Spring 2019

Investigation into the flow physics of large experimental offshore wind farms in a turbulent boundary layer wind tunnel

John James Turner
University of New Hampshire, Durham

INVESTIGATION INTO THE FLOW PHYSICS OF LARGE MODEL OFFSHORE WIND FARMS IN A TURBULENT BOUNDARY LAYER WIND TUNNEL

BY

JOHN J. TURNER V

B.S., Engineering Physics: Mechanical Engineering, University of Connecticut, 2012

DISSERTATION

Submitted to the University of New Hampshire
in Partial Fulfillment of
the Requirements for the Degree of

Doctor of Philosophy

in

Mechanical Engineering

May 2019

This dissertation has been examined and approved in partial fulfillment of the requirements for the degree of Doctor of Philosophy in Mechanical Engineering by:

Dissertation Director, Martin Wosnik,
Associate Professor of Mechanical Engineering
and Marine Sciences

Chris White,
Associate Professor of Mechanical Engineering

Thomas C. Lippmann,
Associate Professor of Earth Sciences

Ivaylo Nedyalkov,
Lecturer in Mechanical Engineering

Lakshmana Doddipatla,
Lead Research Scientist,
FM Global Research

on March 25th, 2019.

Original approval signatures are on file with the University of New Hampshire Graduate School.

This work is dedicated to my mother, ***Joannie Turner****, with wisdoms:*

- *Don't overload the washing machine.*
- *Polite. Polite. Polite.*
- *Never call someone an ass, unless of course, they are.*

Thanks Mom.

ACKNOWLEDGMENTS

This work would not have been possible without my committee members, who put in the extra effort to see this dissertation to completion. Thank you to my adviser, Martin Wosnik, for fostering a learning environment throughout the process. Thank you to the Department of Mechanical Engineering at UNH, who supported me financially for many semesters of teaching assistantships, and the Graduate School for support with two Summer Teaching Assistant Fellowships.

I am of course in debt to my fellow Ph.D. colleagues and friends at UNH. Drummond, Brandon, Sarah, Mike, Scott, Salme, Alley, Justin. You helped break departmental boundaries and grind through courses and research alike. We certainly have learned a lot from each other. I know all of you will make great scientists, and stay great friends. Special thanks to Emily, who suffered through the complaints along the way, while providing emotional support and some key advice: "Write it!".

While at UNH, I enjoyed opportunities to give back to the community through outreach, sometimes introducing people to the concept of fluid dynamics for the first time. From the hundreds of people I've toured through the Flow Physics Facility, to more concentrated weeks with high schoolers at the UNH Tech Camp, I'm proud to have helped inspire the future generation of engineers. These moments have kept me going throughout this degree.

I'm highly appreciative of those who first introduced me to the subject of Physics in high school, Dr. Walter Sieling and Mrs. Catherine Burns, the best physics teachers you could ask for.

Lastly, and most importantly, thanks to my family. To my brother Paul, who's dedicated to keeping the rest of us on the cutting edge of technology. To my mom, Joannie, who will never stop believing in her two sons, and whose boundless energy gives inspiration to everyone who meets her. And to my dad, John. Although you're no longer with us, the coupling of your mathematic prowess and comedic wit lives on forever in my memories, and in me.

ABSTRACT

Investigation into the Flow Physics of Large Model Offshore Wind Farms in a Turbulent Boundary Layer Wind Tunnel

by

John J. Turner V

University of New Hampshire, May, 2019

Large offshore wind turbine array power plants will soon be appearing along the United States' eastern seaboard. With recent advances in technology, turbines have been growing in diameter and arrays have been growing in scale, but not without technical challenges. There exist knowledge gaps in the fluid dynamics that govern the interaction of the incoming atmospheric boundary layer with the wakes of the turbines and the sequential wake–wake interactions that result in an unavoidable decreased bulk power production compared to predicted capacity from the array.

Wind farm experiments were conducted with scale model wind turbines in a high Reynolds number boundary layer wind tunnel. The studies were conducted in the University of New Hampshire Flow Physics Facility which is the world's largest flow physics quality turbulent boundary layer wind tunnel, with test section dimensions of 6 m wide, 2.7 m tall and 72 m long. The long fetch of the facility offers unique opportunities to study the downstream evolution of the wake of single wind turbines, and the flow through model wind turbine arrays over long distances.

Two different types of model turbines were built for these studies at a 1:500 scale based on the National Renewable Energy Laboratory 5 MW offshore reference turbine. Nine 0.25 meter diameter rotating model turbines, and 95 drag matched porous disks of equal diameter were constructed. The two models were shown to have similar enough wake characteristics that they were then used to build up an experimental array. Several experimental campaigns were carried out and selected results are presented here.

An experimental campaign using an array of porous disks placed in atmospheric boundary layer flow was carried with spacings of 8 diameters in the stream wise direction and 4 diameters in the span wise direction. Far downstream within a wind farm it is proposed that the flow through

the farm reaches a fully developed state where the flow field becomes similar from one row to the next. It is suggested that the wind turbine array acts as a sparse displaced roughness, which creates an internal layer whose origin (in the wall-normal direction) remains fixed in space, while the turbulent boundary layer it was placed in continues to grow. To within experimental uncertainty, a fully developed wind turbine array boundary layer condition is observed in the mean velocity, for defined inlet conditions and spacings, from row 12 on.

A careful consideration of experimental uncertainty is discussed due to the large physical scale of the wind tunnel and open-to-atmosphere nature. An expanded uncertainty analysis using the Taylor series method is executed to predict uncertainty for the system of interest in the mean flow. This expanded uncertainty prediction was confirmed by a Monte Carlo simulation. A workable compromise between data acquisition time and uncertainty was used in the experiments, mitigating changing initial conditions due to exposure to atmospheric conditions and temperature changes. This experimental array is sufficiently large to converge on a statistically stationary state in the mean to within 95% confidence level.

Another campaign was carried out with the combination of porous disks and rotating model turbines to study the phenomenon of wake meandering, a dynamic non-periodic shift in the wake over time caused by the atmospheric wake interaction. High temporal resolution velocity time series were obtained at high enough frequencies to resolve oscillatory trends behind individual and coalescing wakes of turbines in boundary layer flow. For single turbine models, incipient wake meandering frequencies decay with downstream distance, along with peak spectral energies and eventually return to those of the incoming turbulent boundary layer flow. However, the meandering also presents itself in the large experimental array, and far downstream the peak meandering frequency is dominated by the turbine spacing, indicating a type of resonance of the array itself.

Porous disk turbine models are the experimental equivalent of numerical actuator disks, therefore, in addition to insights gained into the flow physics of turbine arrays, the publicly available data set is expected to be useful for numerical model validation.

TABLE OF CONTENTS

NOMENCLATURE

δ	Boundary Layer Height
δ^+	Displacement Thickness
λ	Tip speed ratio
ω	Rotor rotational speed
$\overline{x}$	The mean of variable x
ρ	density of air
Θ	Momentum Thickness
b_r^2	Systematic Uncertainty
C_D	Coefficient of drag
C_L	Coefficient of lift
C_{pr}	Pressure Coefficient
C_p	Coefficient of performance
D	Turbine Diameter
f_s	Frequency of vortex shedding
Gr	Grashof Number
N	Number of Independent Samples
P	Transducer Differential Pressure Reading
P_{atm}	Atmospheric Pressure
r	Rotor radius
$R_g(k)$	Autocorrelation
$S(f)$	Power Spectral Density
s_r^2	Random Uncertainty
$s_{\overline{x}}$	Standard Deviation of the mean

St	Strouhal Number
T	Temperature
$t_{\%}$	Student's t Distribution Value
T_w	Hotwire Temperature
U	Wind velocity
$U_{\%}$	Bounds containing the true value of the measurement
u_c	Uncertainty of a variable c
u_{*hi}	Friction Velocity above Turbine Canopy
U_∞	Velocity at Free stream
U_{cl}	Velocity at turbine centerline
U_{hub}	Wind velocity at hub height
x/D	Streamwise location w.r.t. Diameter
y/D	Wall normal location w.r.t. Diameter
z_g	Gradient Height
ABL	Atmospheric boundary layer
ASCE	American Society of Civil Engineers
ASL	Atmospheric Sublayer
BEM	Blade element momentum
CFD	Computational Fluid Dynamics
CTA	Constant Temperature Anemometry
DAQ	Data Acquisition System
DOE	Department of Energy
DoF	Degrees of Freedom
DOI	Direct object identifier
Eq	Equilibrium Region
FFT	fast Fourier Transform
FPF	Flow Physics Facility

H_{hub}	Hub Height of the Turbine
HAWT	Horizontal axis wind turbine
LES	Large Eddy Simulation
MCM	Monte Carlo Method
NACA	National Advisory Committee for Aeronautics
NREL	National Renewable Energy Laboratory
OAPEC	Organization of Arab Petroleum Exporting Countries
PIV	Particle Image Velocimetry
POD	Proper Orthogonal Decomposition
R^2	Coefficient of Determination
SDR	Sparse Displaced Roughness
TSM	Taylor Series Method
UNH	University of New Hampshire
WTABL	Wind Turbine Array Boundary Layer
ZPG	Zero Pressure Gradient

LIST OF TABLES

Table **Page**

LIST OF FIGURES

Figure **Page**

CHAPTER 1

INTRODUCTION

Energy is one of the foremost grand challenges facing our society today. It is inherent to human nature to control our environment to harness and utilize the energy sources provided by the earth and sun. In the early days of humans, biomass was prevalent in the creation of heat and light, and earth harvested energies such as the flowing of a river was used for travel and to transport goods. As population slowly expanded, the control of increased energy density fuels became more commonplace, and the fossil fuel economy was born in the mid 17^{th} century [118]. One hundred years later, with the invention of the steam engine, the industrial revolution required energy needs surpassing biomass and coal production alone [21] and caused a sharp increase in population [118]. In the 1900's the explosion of the usage of the combustion engine and commercial electricity created an exponential demand for energy that was met by petroleum based fuels and the refining of crude oil.

Then, with the west increasingly dependent on imported oil in an increasingly globalized world, political dissent involving the Yom Kippur War created an energy crisis. In 1973 the Organization of Arab Petroleum Exporting Countries (OAPEC) placed an embargo on oil which harshly impacted the certainty of global energy security. Deemed the 1973 global oil crisis, the price of oil per barrel in the United States increased by 300% in only six months [69]. The price of electricity skyrocketed and electricity and gasoline rationing was implemented across the nation. Extreme examples include reduced lighting on the highways, the entire state of Oregon banned Christmas lights for one year [51] and driving was forbidden in Germany on Sundays. The crisis led to a need for a diversified energy budget with interest in alternative energy sources and a commitment to renewable energy. Thus, the modern wind energy movement was born. Wind energy for electricity production has largely been driven by shifts like these in the global oil market.

1.1 Wind Energy History

Utilizing wind to human advantage has been around since man could sail. Farm wind pumps and drainage wind mills have existed for at least 1000 years as evidence by the iconic Zaanse Schans windmills still dotting North Holland of the Netherlands today seen in Figure 1.1 [99]. Some windmill ancients are forever preserved in the classic 15^{th} century Don Quixote, whom, with the help of Sancho, tilted at windmills with arms 'well nigh two leagues in length' [102]. Even the first electrically generating wind turbine was built back in the late 1800's. However, the scale of the electricity demand in the 1970's and 80's called for innovation. In the U.S., the

Figure 1.1: Dutch Zaanse Schans Windmills. Constructed circa 17th century [99]

aerospace industry attempted to tackle this problem with informed knowledge of rotary blades from helicopter design, but none proved to produce a reasonable cost of energy. The utility scale turbines of the U.S., majorly pioneered by NASA, were never put into mass production, partly due to the dropping of oil prices into the early 90's [113]. In Denmark, a decentralized electric system had been forming since the turn of the 20^{th} century, which included development of smaller $\approx$10 kW scale multi-bladed wind turbine models. These demonstration attempts grew in diameter with increasing practical knowledge to fit demand, and Denmark Technical University eventually produced calculations for the blades of the first installed multi-megawatt turbine in the late 70's.

These developments culminated at the three bladed, tubular tower, pitch controlled concept of turbines we see in the plains and on the oceans today [113].

Figure 1.2: Photograph of the Siemens 3.6 MW turbines that make up the London Array off the eastern coast of the UK [86]

At the turn of the 21^{st} century, political instabilities in oil producing nations such as Iraq and tensions in the Gaza Strip brought concerns over energy security once more. Additionally, concerns of climate change and eventual depletion of our non-renewable (for human timescales) fossil fuels were growing. The increases in energy prices in the new millennia again reminded the U.S. about interest in commercial wind energy [21]. Technological advancement also played a part in growing the industry with new material development for blade and tower construction, increased power generation efficiency, and a better understanding of siting conditions, fluid dynamic interactions, and plant scale efficiencies aided by computer engineering. Wind turbines have become the largest rotating machines on earth, with multi-megawatt turbines as a normal, while plans for fu-

ture turbines show even larger diameters (certainly longer blades than ‘two leagues’). The turbines themselves are growing, and so is the vision of arrays dominating large swaths of lands, creating power plants of impressive scale.

1.2 Current state of wind energy plant installations

Wind power plants of 1 GW installed capacity and 100 km^2 have already been realized [113]. One of the worlds largest offshore wind farms located off the south eastern coast of the United Kingdom, the London Array, can be seen in Figure 1.2. The London array boasts 175 operational 120 m diameter Siemens 3.6 MW turbines. The turbines are placed between 650 m and 1200 m apart, or 5.4 – 10 turbine diameter spacing and the array covers a total area of 100 km^2 [86]. From the

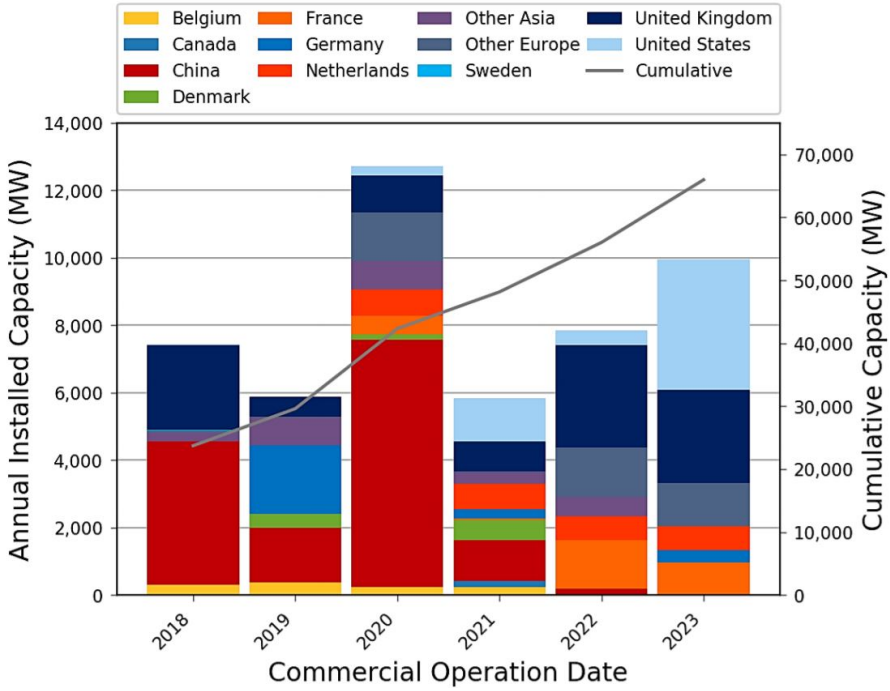

Figure 1.3: Global offshore wind project pipeline through 2023, by country [96]

United States Department of Energy (DOE) 2017 Wind Technology Market Report, wind power represents the third largest source of electrical generating capacity additions in 2017, behind solar and natural gas [40]. The United states currently employs over 105,000 full time workers in the wind energy sector, which is expected to grow at least for the next few years. By the end of 2017,

cumulative wind power capacity in the United States was 88.9 GW with turbine design changes driving capacity factors higher over time and increased height increasing production. It is forecasted that wind additions in the near term in the U.S. will reach roughly 10–13 GW in 2020 [40]. The world's offshore wind energy potential is sufficiently large to power our present energy needs many times over. Offshore wind farms active installments and new proposals are at an all time high as seen in the global offshore project pipeline (Figure 1.3) from the 2017 offshore wind technologies market report update from the national renewable energies laboratory (NREL) [96]. While the U.K. and Germany are the current leaders in offshore wind installed capacity [58], the United States alone has 4.9 GW of offshore wind currently in advanced development stages slated for installation [59]. Cumulative global offshore wind installed capacity was 19 GW at the end of 2017 [58] and has the potential to reach 47 GW by 2020 [59]. Concurrently, offshore wind farms are growing in terms of capacity and number of installed turbines per wind farm.

Our knowledge of wind turbines has grown over time, but there are still significant research challenges ahead. Our energy future's current projections vary highly with uncertainty in petroleum imports and production. What is certain is the increasing likeliness that non-carbon energy resources, especially wind energy, will help fill in the energy budget and aid the United States' energy sustainability and security goals.

CHAPTER 2

BACKGROUND AND MOTIVATION

This chapter is an overview of the basic science background of wind energy and motivation for the following work.

2.1 Principles of the Horizontal Axis Wind Turbine

Horizontal axis wind turbines (HAWT) operate as a spinning lift driven devices connected to electrical generators. A turbine is a very common device for converting mechanical energy from air or water flows into shaft work and thusly electrical energy. The HAWT is an axial flow machine with propellers that rotate in a plane perpendicular to the incoming fluid flow, or, with an axis of rotation aligned with the flow direction. The generator is suspended at the top of the tower in a housing known as the nacelle, and sometimes include gearboxes. The blades are connected to the generator through the nose of the nacelle known as the rotor. While most HAWTs use a tubular tower design, some especially tall turbines use a lattice tower. Wind turbine designs are no longer changing in concept as much as other forms of renewable technology, as the industry has matured into the converged 3-bladed, upwind rotor with yaw and pitch control. The manufacturing of an additional blade does not create enough additional efficiency to be justified from a cost perspective. Additionally, three bladed rotors are thought to appear more fluid to the public when rotating and more neat when stationary than 2 bladed designs [55]. Figure 2.1 is an image of Danish offshore wind farm Middelgrunden, representing what most wind turbines look like today [95].

2.1.1 Aerodynamics of the HAWT

A classical wind turbine analysis was performed by Betz in the 1930's. The momentum analysis involves a stream tube analysis with an actuator disk or momentum sink concept ide-

Figure 2.1: 2 MW Bonus Turbines in the Middelgrunden wind farm in Denmark [95]

alized in place of complex rotating elements. The result of the mathematics dictates the theoretical maximum that any lift driven device in a flow can achieve. The so called Betz limit is $C_{p,max} = 16/27 \approx 0.593$. For brevity, the derivation is skipped here. The momentum analysis can then be extended to include forces on blades divided into blade elements, called blade element momentum (BEM) theory, to calculate the theoretical performance by summing sections of the whole rotor [88].

Wind turbines are lift driven devices. The blades of turbines are comprised of airfoils with various cross sections, twist angles and cambers. These blades then can be rotated to the specific oncoming flow relative to the chord line, ie. angle of attack. For more on the design of turbine blades see Chapter 6 of Manwell [88]. The core principle is positioning the plane of rotation with the blade normal to the wind direction so that the redirection of the air over the blade creates a resultant force which puts torque on the gearbox [103]. As aerodynamic lift is responsible for the operation of the blade and resultant power generation, is necessary to maximize the lift, but also consider drag. The drag is a force that opposes the motion of the blade. The lift must be greater than the drag for operation (consider the flight of an airplane using wings comprised of airfoils) which is why the lift to drag ratio is considered. The lift to drag ratio, simply the coefficient of lift over the coefficient of drag (*Lift to Drag Ratio*$= C_L/C_D$), needs to be high, and is typically over

30 [87]. Coefficients of lift and drag are tested experimentally on airfoil shapes in relation to angle of attack and are compiled in databases such as the National Advisory Committee for Aeronautics (NACA), the precursor to NASA [88].

Another aerodynamic quantity of interest is the tip speed ratio. As it is not possible to match the kinematic, dynamic, and geometric similarities all at once for a model turbine due to the smaller scale, compromises must me made. It is very challenging to match the blade chord Reynolds number of the turbine, but in an attempt to come closer to the desired Reynolds number the blades end up being wider than what the the geometric scales would suggest. Equation 2.1 is the tip speed ratio defined as the relationship between blade velocity ω at the tip with radius r and the relative incoming wind velocity U. is the tip speed ratio

$$\lambda = \frac{\omega r}{U} \tag{2.1}$$

Efficiency of a turbine can be increased with higher tip speed ratios, but not without trade-off. At very high tip speed ratio (eg., over ten) may be desired to match a given generator's rotation rate, but considerations of centrifugal stress, aerodynamic stress, and noise have consequences associated with preventing blade failure. High tip speed ratio blades have more critical aerodynamics than low tip speed ratio designs and must have high cut in speeds or can have trouble self starting owing to low torque at low speeds. However, efficiency decreases significantly below a tip speed ratio of five due to the rotational wake created by the high torque. Additionally, the lower the rotational speed, the less solidity area exists which will increase the number of blades needed. Lower tip speed ratios are commonplace for older uses such as water pumps or mills. The standard 3-bladed design wind turbine for electrical generation thusly has a tip speed ratio in the 6-9 range [103].

2.1.2 Fluid Dynamics of the flow field

Thus far the aerodynamic discussion of wind turbines has only touched on the turbine itself, however, a large topic covering the fluid dynamics should also be discussed, ie. the surrounding

flow field. Wind turbines operate in the bottom layer of the atmosphere, where the wind is affected by the ground and becomes slower near the surface of the earth and faster farther away from this boundary, the atmospheric boundary layer (ABL). Turbines are generally built tall enough (total height 400 – 600 ft ≈120 – 180 m) and with large diameters to reach up into the atmosphere and capture some of the faster wind speeds to generate the most electricity possible. Each wind turbine generates its own wake, which affects downstream turbines as seen by the visualization in Figure 2.2. This photo was taken of the Horns Rev II wind farm off the coast of Denmark [5, 64]. The Horns Rev wind farms have produced iconic examples of how upstream wakes affects downstream turbines. The coupling of the wakes and atmospheric dynamics forms the wind turbine array boundary layer to be explained in Section 2.2.5.

Figure 2.2: A naturally occuring visualization of the wake at the Horns Rev II wind farm off the West coast of Denmark [64, 63]

2.1.2.1 Wakes

The wake is the region of flow directly behind an object. The turbulent wake is a free shear flow that develops without the presence of a boundary. Turbulent wakes have momentum deficits

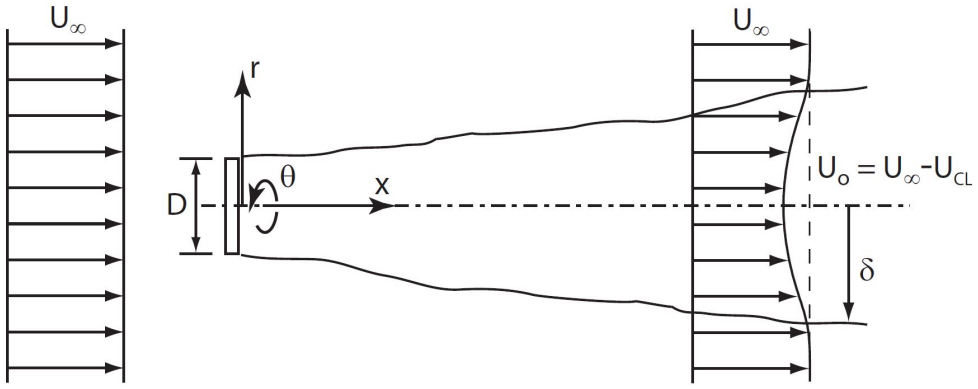

Figure 2.3: Diagram of the axisymmetric wake. U_∞ is the free stream velocity. U_{cl} is the wake centerline velocity. U_o is the centerline wake deficit. δ is the wake width. x; r; and θ represent the streamwise, radial, and azimuthal coordinates of the wake with the origin at the center of the rotor [75, 109]

in comparison to the incoming flow when the object is held stationary, or when the object is towed through a quiescent flow. The momentum deficit is caused by boundary layer separation at the edges and the low pressure zone downstream of the object. In the wake of a turbine, an axisymmetric object, the flow is turbulent and there exists an additional momentum deficit caused by the extraction of energy by the turbine. A diagram of the axisymmetric wake in a uniform incoming flow U_∞, as created by a turbine, is shown in Figure 2.3 [75, 109]. The wake grows downstream of the object, noted by δ. The centerline wake deficit is shown as U_o.

The impact of the wake of an upstream turbine on a downstream turbine has implications ranging from decreased power production to fluctuating loads on the rotor which lead to cycle fatigue. The consideration of downstream flow is important, as turbines for power plant generation scales are built in arrays. The velocity profile impinging downstream turbines can shift in the in rotor plane direction due to skewness of upstream wakes leaving the downstream turbine with an incoming shear flow, stressing the blades in an unequal manner and complicating prediction of power production.

The wakes of turbines are generally broken up into two main categories, the near wake and the far wake. The difference is determined by the intensity and spatial distribution of turbulence between the two regions [88]. The near wake (less than 3 diameters downstream) is fraught with

vortex sheets, trailing edge and hub vortices, and mean rotation. Turbulence and vorticity generated in the near wake are diffused in the far wake by the velocity gradients of the deficit itself and become evenly distributed downstream [84]. The pressure field close to the upstream turbine is important for development of the wake deficit further downstream. In this study, the concern is mainly that of the far wake, where the near wake rotational component and shedding of vortices from the blade tip coalesce into a mean deficit. The mean velocity deficit is what impacts downstream turbines and causes bulk power production losses in comparison to predicted capacity in arrays.

It should be noted that the mean velocity deficit of a turbine in the freestream has been shown to collapse with the scaling $U_o \approx (U_\infty - U_{cl}) \approx x^{-2/3}$ where U_{cl} is the velocity at the centerline [41]. The wake is shown to grow as $\delta^* \approx x^{1/3}$ where δ^* is the wake displacement thickness [109]. Additionally, $W \propto U_o^{3/2}$, i.e. the mean rotation of an axisymmetric wake with swirl decays faster than the mean deficit. When subjected to shear, as in a turbulent boundary layer, the rotation is expected to decay even faster [109]. However, to date, a similarity analysis has not been found for an axisymmetric wake with mean shear, as in the case for a turbine in a boundary layer.

2.1.2.2 Atmospheric Boundary Layer

Consider a flow along a surface caused by a pressure gradient along the flow direction. The flow along a no slip wall, that is effected by the sustained rejection of momentum to this wall is known as a boundary layer. We will consider the flow to have a high enough Reynolds number to be turbulent, and that this momentum rejection is caused by the mechanical shear force. The boundary layer creates the somewhat parabolically shaped velocity profile seen in Figure 2.4 [79]. The boundary layer can be broken up roughly into an inner region and outer region of the flow. The inner layer has complicated physics regarding the structure of the turbulence and the internal transitions between inner subregions. These topics are not explored here as wind turbine rotors exist mostly within the outer region of the flow. The discussion of the inner regions of boundary layers are best saved for pure boundary layer scientists, where (from their perspective) our large

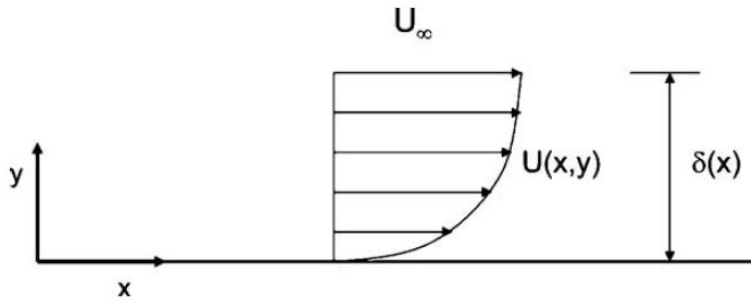

Figure 2.4: Velocity profile diagram of a turbulent boundary layer [79]

obstacles (wind turbines) significantly modify the delicate fundamental physics of flow over a flat plate. The largest turbulent structures exist in the outer region of the turbulent boundary layer, and more detail will be found in the discussion of the modeling of the atmospheric boundary layer in the facility used for these experiments.

Class	Exposure[a]	Terrain Description	z_o^b (m)	n^c	$1/\alpha^d$	l_u^e (%)	${}^xL_u^f$ (m)	z_g^g (m)
1	D	Open sea, fetch at least 3 mi (5 km)	≈0.0002	0.1	0.09	9.2	190	213
2	-	Mud flats, snow; no vegetation, no obstacles	0.005	0.13	-	13.2	140	-
3	C	Open flat terrain; grass, few isolated obstacles	0.03	0.14	0.11	17.2	110	274
4	-	Low crops; occasional large obstacles $x'/h > 20$	0.1	0.18	-	21.7	84	-
5	B	High crops; scattered obstacles, $15 < x'/h > 20$	0.25	0.22	0.14	27.1	64	366
6	-	Parkland, bushes; numerous obstacles, $x'/h \approx 10$	0.5	0.29	-	33.4	55	-
7	A	Regular large-obstacle coverage (suburb, forest)	1.0–2.0	0.33	0.20	43.4	45	457
8	-	City center with high and low rise buildings	>2	0.40–0.67	-	-	-	-

Table 2.1: Neutral Boundary Layer Parameters recreated from ASCE 49-12 [9].
Note: x' is typical spacing between obstancles; h is the height of a typical structure or obstacle.
[a] Exposure categories from ASCE 7
[b] Regional roughness lengths
[c] Mean velocity power-law exponents
[d] 3-s gust power law exponents
[e] Turbulence intensities for FUR terrain ($z = 10$ m) with the same local roughness length
[f] Integral lengths of turbulence for $U_{10} = 20$ m/s, $z = 10$ m, and $f_c = 1 \times 10^{-4}$ rad/s
[g] Gradient heights

The incoming approach flow that impinges upon an array of wind turbines in open terrain is the atmospheric boundary layer (ABL). The ABL can be on order 1 km in height and can be defined by different categorized assessments of obstacles over the development fetch. The American Society of Civil Engineers has defined categories for the ABL so that correct physics can be applied when using a wind tunnel to study scale structures or dwellings, or for locating correct wind load standards for construction purposes. Calling on ASCE Standard 49-12 Table C2-1 (recreated here as Table 2.1) [9], which comes from ASCE 7-16 [10], the ABL has four main categories that are based on the change in power law fit and wall roughness. Category A exposure is the urban, city center type category. Category B exposure is defined as "Urban and suburban areas, wooded areas or other terrain with numerous closely spaced obstructions having the size of single-family dwellings or larger". Category C exposure is defined as "Open flat terrain; grass, few isolated obstacles". And finally category D exposure is defined as "Flat, unobstructed areas and water surfaces outside hurricane-prone regions including smooth mud flats, salt flats, and unbroken ice" [10]. For wind turbine arrays, categories C and D are the most appropriate. Wind farms are located in areas with large flat development fetches sometimes spanning for miles. Especially in the case of an offshore wind farm, the roughness height of the ocean in comparison to the height of a wind turbine is almost negligible, and therefore would be considered a category D atmospheric boundary layer. This incoming boundary layer couples with the wakes of the turbines to produce complex interactions that are the focus of this work.

2.2 State of the Art

While small wind farms are generally favorably aligned with the prevailing wind direction, in large wind farms there is no a priori arrangement and tuning of turbines for a given prevailing wind direction that maximizes power production. In large offshore wind farms with regularly spaced turbine (gridded) alignments, wake effects can cause an average bulk power production decrease of up to 20% [15]. A knowledge gap exists on how to best space or operate these large wind farm arrays. In these large wind farms, turbines many rows downstream of the wind facing row can

have greatly decreased power output. It is important to accurately model wind turbine arrays and

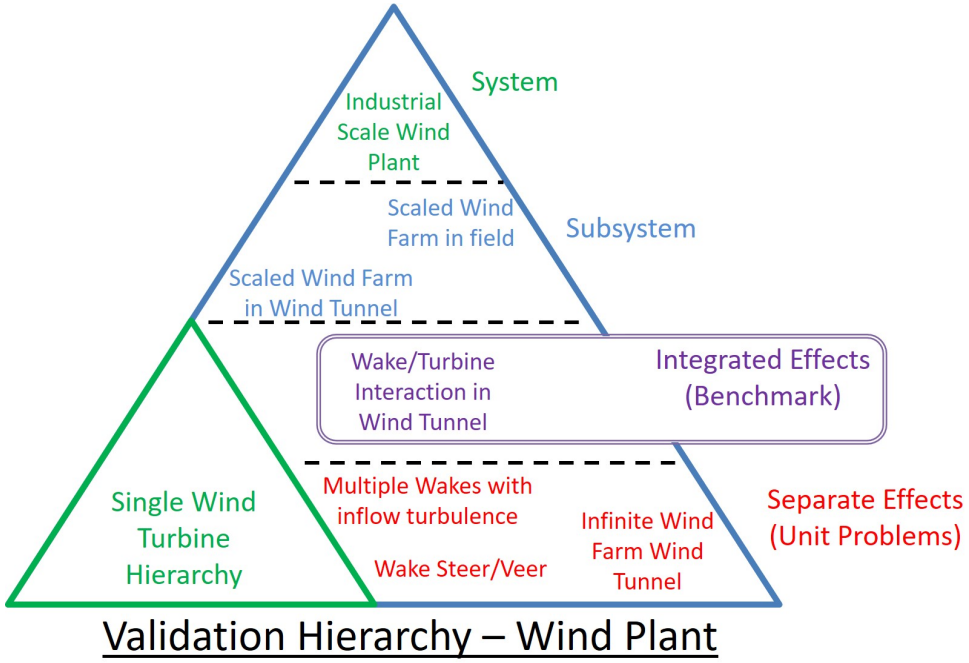

Figure 2.5: Validation Hierarchy adapted from Jonathon Naughton [92]

to be able to select a turbine layout and spacing that maximizes wind farm bulk power production. This requires a detailed understanding of wind turbine array fluid dynamics. Even though much progress has been made in recent years, predictions of in situ wind farm airflow are difficult due the complex physics of the interaction of the atmospheric turbulent boundary layer with the turbine wakes, and wake-wake interaction [113]. A validation hierarchy is shown in Figure 2.5, adapted from Jonathan Naughton [92]. With the goal of understanding the physics of the industrial scale wind plant, categories of scale are narrowed down to base physics. This study presents data for a model wind farm in a large turbulent boundary layer wind tunnel. The appropriate scale for this study is the integrated effects of turbine wake and boundary layer interaction in a wind tunnel, a benchmark study.

2.2.1 Uncertainty

The quantification of uncertainty in velocity measurements is critical in experimental fluid mechanics, especially when dealing with a complex flow such as the wind turbine array boundary layer. In physical experiments the nonspatial independent variables such as flow rates, fan speeds, control pressures etc. can never be held perfectly constant [49]. Even the probing of the physical system by the measurement probe can introduce error [106]. However, obtaining data from a physical set of conditions provides the closest understanding of the physics governing that system. The goal, then, is to yield the lowest result uncertainty while balancing program constraints on data collection requirements. There is a need to improve mathematical models of even well understood flows with well detailed experiments and these should be executed with complete candor about the strengths and weaknesses when comparing model and experimental results [97]. In these types of experiments, the computational analyst is the target audience, who may use the data for verification and validation.

The need to reconcile how good the models function is known as Verification; the question of whether the model computes the equations correctly. Here, we aim to assist in the process of Validation; the process of determining how accurately these models represent the real world. Validation experiments aim to be more complete than novel scientific studies, including boundary conditions and consideration of experimental variability [83]. Recall the validation hierarchy triangle pictured in Figure 2.5. An expanded uncertainty analysis was performed in this thesis and can be found in Chapter 4.

2.2.2 Miniature Wind Farms

Miniature wind farms have previously been investigated using various turbine scales, numbers of turbines, and arrangements. Studies of the velocity field were performed with model wind farms of up to 14 rows and with 2 or 3 columns of turbines by a number of research groups. Table 2.2 contains a list of scaled wind turbine array experiments in wind tunnels. They are listed in order of publication date. From left to right, this table includes; an assigned study number and

citation (Study), number of turbines (No.), turbine diameter in meters (D), type of turbine in the array (Type), stream wise spacing in diameters (S_x), span wise spacing in diameters (S_z), free stream velocity in meters per second (U_∞), coefficient of thrust (C_T), top tip height of the turbine normalized by boundary layer height (H_{TT}/δ), type of boundary layer in the wind tunnel (BL type: either naturally grown, or thickened with help by an active or passive grid), tunnel name where the experiments were performed (Tunnel), tunnel cross section (XS) in height $\times$ width in meters. A dash indicates the information is not provided.

Many studies look to understand the physics of the wind farm in the limit of infinite rows or "infinite" wind farm or "fully developed" condition. In current day large wind farms (See Chapter 1), turbines are arranged in grids that always have wake effects on downstream turbines, no matter the prevailing wind direction. However, these wake effects do not completely halt the downstream turbines' energy capture. It is believed that some of the energy that sustains an array may come from above the array. The fluid dynamics of continued power production far downstream in arrays are of interest to maximize this power production and some model wind farms work were constructed to better understand this energy transport.

Study	No.	D (m)	Type	S_x	S_z	U_∞	C_T	H_{TT}/δ	BL type	Tunnel	XS
1 Corten [37]	28	0.25	bladed	5,4	3	5.0	0.89	-	Natural	TNO	2×3
2 Cal [25]	9	0.12	bladed	7	3	9.4	0.32	0.64	Strakes, actv grd	Corrsin	0.9×1.2
3 Chamorro [31]	30	0.13	bladed	5,7	4	3.0	0.42	0.43	Natural	Saint Anthony Falls	1.7×1.7
4 Hamilton [60]	9	0.12	bladed	7	3	9.4	0.32	0.64	Strakes, actv grid	Corrsin	0.9×1.2
5 Newman [94]	15	0.12	bladed	5	3	8.0	0.46	-	Strakes, chains	Corrsin	0.9×1.2
6 Theunissen [110]	80	0.025	disks	7	7	9.0	0.82	-	None	Bristol	2.1×1.5
7 Hancock [61]	12	0.416	bladed	6	2.4	1.5	0.48	0.48	Spires	Enflo Meteorological	1.5×3
8 Bossuyt [22]	100	0.03	disks	7	5	-	0.75	0.25	Active, pssv grd	Corrsin	0.9×1.2
9 Camp [28]	12	0.12	both	6	3	9.0	0.64	0.60	Strakes	Portland State	0.8×1.2
10 Coudou [38]	9	0.15	bladed	5	3	8.3	-	-	Natural	VKI L-1B	2×3
11 Turner [111]	95	0.25	both	8	4	6.7	0.92	0.43	Spires, natural	FPF	2.7×6

Table 2.2: List of experimental turbine array studies conducted in wind tunnels arranged by publication year. A dash mark means the information was not reported.
Study: Assigned study number and citation
No.: Number of turbines
D: turbine diameter in meters
Type: Type of turbine in array
S_x: Stream wise spacing measured in diameters
S_z: Span wise spacing measured in diameters
U_∞: Free stream velocity in meters per second
C_T: Coefficient of thrust
H_{TT}/δ: Top tip height of the turbine normalized by boundary layer height
BL type: Type of boundary layer in the wind tunnel (either naturally grown, or thickened with help by an active or passive grid)
Tunnel: Tunnel name where the experiments were performed
XS: Tunnel cross section (height $\times$ width) in meters

Corten et. al. aimed to get a basic understanding of the power production stabilization of wind farms with an 8 row and 3 column array of two bladed turbines. They also drew attention to the overestimate in efficiency of classical wind farm models that optimistically assumed a steady state too early in the farm [37]. Cal et al. examined the horizontally averaged structure of the flow and measured the Reynolds turbulent shear stresses to be of the same order as the power extracted by the wind turbines [25]. This leads us to the conclusion that the vertical kinetic energy is the driver of the power production stabilization in infinite wind farms. Chamorro and Porté-Agel took hotwire measurements in a miniature aligned wind farm and characterized the regions within and above the farm noting that large wind farms could be treated as a special case of surface roughness. They noted a strong enhancement of turbulence levels around top tip height and the growth of an internal wind turbine array boundary layer [31]. Chamorro and Sotiropoulos studied a staggered wind farm and showed that the momentum transfer is improved with larger spacings, however, a large distance is required for the adjustment of flow statistics above the farm [32]. Hamilton et al. performed a statistical study of the sweeps and ejections that contribute to the vertical kinetic energy flux from the flow above and argued that sweeping motions dominate the net entrainment of kinetic energy that can ultimately be used at the wind turbine location [60]. The last study listed in Table 2.2 (Study 11) is the current study [111]. The present work can be considered an extension of these studies. A photograph of one setup of the wind turbine array discussed in this thesis using a combination of 0.25 m diameter porous disks and model turbines can be found in Figure 2.6. This photograph is used here for a scale reference for this and future sections. This array is positioned to examine the worst case flow direction where the turbines are arranged in aligned rows and columns with a uniform incoming wind direction.

While studies with rotating miniature turbines have yielded important insight into the energy transport phenomena in arrays of turbines, they are generally more challenging to use for model validation due to the small model scale of the turbines, and low-Reynolds number effects of the flow over the rotor blades and in the near-wake. One potential solution to the experimental challenges are analytically modeled farms that work towards solving the coupled wake boundary layer

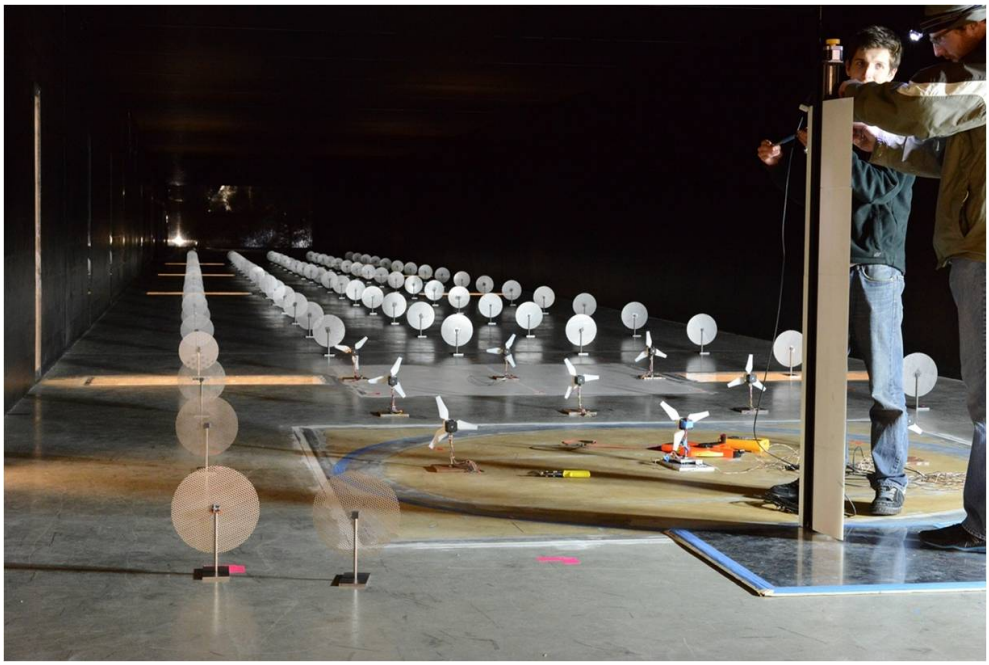

Figure 2.6: Photograph of the combined porous disk and rotating model wind turbine array in the Flow Physics Facility. Photo is taken from the end of the test section looking upstream into the wind tunnel.

problem and optimal power extraction scehemes [50, 100, 108]. However, purely mathematical models, although easy to implement, do not provide the velocity distributions of the full domain and tend to underpredict power losses due to wake effects [16].

2.2.3 Computer simulated modeled wind farms

Prediction models of total wind farm power production and velocity distributions have attempted to be utilized since the 1980's. First, linear mathematical models were applied to the growth of wakes and considered their deficits additive. The Jensen model provides an equation for the wake deficit, the wind speed deficit in the wake of a turbine, using momentum theory. The model assumes an axisymmetric expansion of the wake where the velocity just behind the rotor is $1/3^{rd}$ the inlet hub height velocity and that the wind velocity is constant within the wake. The model allows the momentum deficit to spread linearly with downstream distance [73]. Although linear combinations of turbine wakes are possible with this model, the wakes are modeled as a top hat distribution as compared to the more realistic Gaussian velocity profile and does not take

into account momentum entrainment that sustains power production far downstream. The model was not extended at the time, as stated in the 1987 publication by Jensen "...since so many aspects concerning wakes need to be clarified..." [74]. Ainslie implemented another early model for the purpose of wind turbine farm site planning. In this mathematical model, a derivation takes place mostly from the governing equations, with a near field empirical filter function. The pressure terms were disregarded from the Navier-Stokes equations when outside the near wake region and gradients of mean quantities are much larger in the radial direction than in the downstream direction which implies the ability to use the thin shear layer approach [3]. The wake decay corresponds relatively well to full scale field measurements with given thrust coefficient values, but the model is still essentially a two dimensional model and cannot account for the wake growth and addition as in the case of a farm of turbines. In two dimensions the model is not able to include vertical profiles of velocity and turbulence which is necessary to capture the influence of the true incoming boundary layer flow and the asymmetry of the wake in the wall normal direction due to the influence of the wall.

Linear models certainly have their benefits in terms of computational efficiency and easy of understanding, but to truly capture all the physics necessary, higher fidelity computations are needed. Mainly, the ability of the models to consider more than simple linear wake additions that then impinges a downstream turbine is lacking. When turbines are aligned in the prevailing wind direction, they behave relatively well, but in the modern day case of hundreds of turbines in a single farm, even the dominant wind direction quickly involves coupling of wake wake behavior within the first few row the farm.

Analytical models paved the way to increasingly complex computer simulations with more than exponentially increasing computational requirements [8]. To help gain velocity distributions and power extraction from the full extent of the domain, modelers turn to computational fluid dynamics (CFD). Initial CFD models used an eddy viscosity to account for the closure problem of the Reynolds-averaged Navier-Stokes equations, but this approach did not allow for the consideration of the wind turbines' effect on the atmospheric boundary layer flow and underpredicted wake

losses [8]. Corrections have been made in applications such as the Deep-Array Wake Model, but the major improvement to the field of prediction came with the usage of Large Eddy Simulation (LES). LES enables modelers to obtain high spatial and temporal resolutions of the full flow field. An image from Goit and Meyers [56] of the velocity field of a simulated wind farm can be found in 2.7.

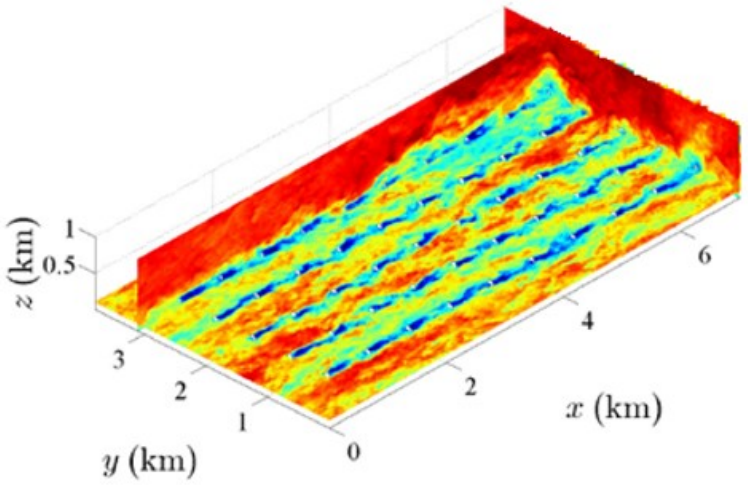

Figure 2.7: An LES simulation of a velocity field in a wind farm from Goit and Meyers [56]

A common technique in LES for wind turbine array studies is to use the actuator disk method, in which the wind turbine is modeled as a momentum sink. These infinitely thin, numerically generated, circular momentum sink models, take the place of fully resolved rotating wind turbines by simulating the momentum extraction, ie. thrust, of turbines. The actuator disk model is useful for wind farm simulations, since it yields significant computational savings compared to blade resolving models [104]. Using the actuator disk model, large wind farms can then be embedded in simulations of wind turbine arrays using LES. Calaf et al. (2010) investigated the flow field surrounding and within a fully developed wind turbine array boundary layer showing that the vertical fluxes of kinetic energy are of the same order of magnitude as the the power extracted by the forces modeling the wind turbines [26]. Calaf et al. (2011) investigated scalar transport in a wind farm which highlighted the influence of a wind farm on local meteorology [27]. Other

researchers were able to apply optimal control algorithms to study the maximization of wind farm energy extraction [56, 57].

2.2.4 Porous Disks vs. Rotating model wind turbines

Experimental studies have shown that the wakes of porous disks or circular meshes are similar to the wakes of wind turbines. Aubrun et al. showed that the wake of a porous disk (segmented, higher porosity at hub) and a model wind turbine achieve similar characteristics with regards to velocity profile and turbulence intensity as close as 3 diameters downstream of the rotor plane [11]. Lignarolo et al. showed that the wake expansion and mean flow kinetic energy entrainment in the near wake was similar between a porous disk and a two-bladed model wind turbine at 2.2 diameters downstream of the rotor [85]. Camp and Cal utilized a circumferentially symmetric porous disk with porosity that varies radially to compare energy terms to a farm built with rotating turbines. Their results suggest that wind farms with array spacings larger than 4 diameters would be adequately represented using stationary disks in lieu of rotating turbines if turbine inflow was the primary concern [28]. In a prior study in the University of New Hampshire (UNH) Flow Physics Facility (FPF) it was shown that the wake velocity profiles of the 0.25 m diameter porous disk models used here were similar to those of three-bladed turbines at 6 diameters downstream in a high Reynolds number boundary layer flow [34]. These results justify the use of physical porous disks instead of rotating turbines in wind tunnel studies of wind turbine arrays. Porous disks are the experimental equivalent of the numerical actuator disk model, and data obtained in wind turbine arrays made of porous disks can readily be compared to actuator disk model simulations.

2.2.5 Fully Developed Wind Turbine Array Boundary Layer Condition

Wind turbines far downstream in arrays continue to produce power, even though upstream turbines greedily extract energy from the incoming flow, reducing the momentum that downstream turbines see. The wind power available to these downstream turbines comes from kinetic energy entrainment from the atmospheric boundary layer above the wind farm [26]. Large arrays eventually approach a statistically stationary state known as the “fully developed wind farm” [50, 30].

The fully developed wind farm condition exists when the mean velocity and turbulence intensity within and above the array and performance of the turbines a number of rows downstream remains consistent from one row to the next [31].

To achieve "fully developed" wind farm conditions, a common practice in CFD is to define a spatial domain with some rows of numerically generated turbines and then apply periodic boundary conditions. The domain outflow gets recycled into the inflow, and the flows passes through the domain many times, and eventually a (sufficiently) statistically stationary state is achieved [7]. It is quite computationally expensive to simulate the entire farm, and only rarely has this been done in recent LES simulations [35]. Experimentally this condition can be achieved only with a very long development fetch and many rows of turbines. The UNH FPF uniquely enables this due to its long fetch, and the question is asked, "When does a particular configuration of wind turbines reach a fully developed state?", one of the goals of this thesis.

2.2.6 Wake Meandering

When investigating wind flow, patterns are observed after a perturbation that produces gusts and vortices. For a wind farm, understanding these coherent structures' generations and lifetimes has huge importance for wind conditions within a wind farm. It is proposed that large scale atmospheric eddies push the wake of single turbines around [22, 38]. This idea can be seen via a diagram in Figure 2.8. The red dot represents the dead center of the turbine hub height and therefore the time averaged center of the deficit. The black $\times$ represents the true center of the instantaneous wake. The instantaneous center of the wake is not aligned with the time-averaged center. This atmospheric wake interaction, a dynamic shift in the wake over time, is a phenomenon known as wake meandering. Intermittency and randomness of the incoming wind resource to downstream turbines affects the reliability and stability of the power supply. The wake impact on downstream turbines causes a decrease in array power production as well as increased rotor fatigue and failure, and wake meandering introduces significant uncertainty in predicting this.

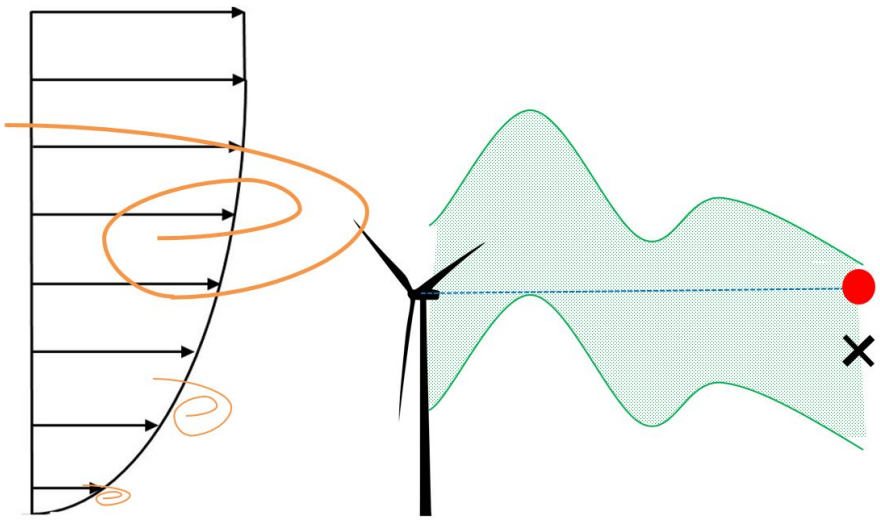

Figure 2.8: Diagram of large scale eddies in the the atmospheric boundary layer pushing the wake of a turbine around causing wake meandering

The meandering phenomenon is not yet well characterized, but the physics can be described by two main possibilities. One, that intrinsic instabilities characterized by vortex shedding, as observed for a bluff body, are produced by the turbine hub, and two, large scale turbulent eddies contained in the atmospheric boundary layer only create meandering when the length scales are larger than the rotor diameter [44]. The shedding of the wake behind a bluff body is usually dominated by boundary layer separation off the sides of the object creating a shear layer and changing the wake size. For bluff bodies the shedding has defined Strouhal numbers ($St = \frac{f_s D}{U}$) and the wake oscillation is sinusoidal [117]. In this case the vortex shedding characteristic length scale is D, the diameter of the turbine. The shedding frequency is f_s and the characteristic velocity is U. However, the meandering phenomenon for a turbine is not characterized by a well-pronounced peak in the frequency domain, but rather by a bumb spread over a larger low-frequencies range, especially at tip height [12]. The incoming atmospheric structures are thought to be the largest contributors to wake meandering.

The detection of large scale coherent motion in boundary layers and other canonical flows has been prevalent in the last half century. Coherency within boundary layer flow was understood via spacetime autocorrelation and crosscorrelation maps obtained by use of streamwise spaced

hotwires by Favre [48]. Later, both streamwise and wall normal components were used to discover the large lasting features of a turbulent flow in an experiment by Kovasznay et al. [81]. These coherent meandering structures can be quite long. Streamwise correlations in the streamwise-wall-normal plane can amount to 7-8 boundary layer thicknesses existing in the log region of turbulent boundary layer flow [112]. More recently, very long streaky structures have been identified in the log region of turbulent boundary layers amounting to up to 20 boundary layer thicknesses [68]. The strongest correlations in the streamwise direction are found within the inertial sublayer of the turbulent boundary layer, however, ramp shaped hairpin packets are found beyond the log layer and cover the entire flow domain up to boundary layer height [1]. Large scale structures also exist in the outer region of turbulent boundary layers, and Liu has shown they may become invariant with increasing Reynolds number [66]. These atmospheric scale structures are part of the inlet atmospheric boundary layer flow to a wind farm and will affect how the internal farm's flow structures behave.

To elucidate some of the very large scale structures that influence the production of turbulent energy inside a wind farm, the technique of proper orthogonal decomposition (POD) has been employed experimentally and through simulation. Either LES or particle image velocimetry (PIV) in a wind tunnel experiment will provide an instantaneous snapshot of the full spatially resolved field necessary to execute POD. Newman et al. performed a POD analysis on the $U\overline{u'v'}$ transport term and found that 75% of the energy in the farm comes from large scale entrainment with wavelengths greater than the diameter of the turbines [94]. Compared to a boundary layer without turbines, the influence of turbines causes energy in low modes (high energy) to decrease, meaning energy not extracted by turbines goes to turbulence production, distributing the flow energy over a wider range of scales. Larger coherent structures are initially destroyed by the turbines presence [94]. However, in a strain gauge instrumented study of micro turbines, the aligned crosscorrelation is strongest in the array, confirming a strong correlation with presence of upstream turbines [22]. Far downstream, structure size and energy grow while the coherency of structures increases [6].

Single model turbines and miniature wind farms have been experimented with in various scales and arrangements, placed in artificially thickened boundary layers. Chamorro & Porté-Agel have shown that upstream turbines impart a signature of shed tip vortices in the velocity spectra of the wakes of downstream turbines [32]. Wind tunnel experiments from Bossuyt show that there are important temporal correlations in turbine power output from the influence of other turbines in the array [22]. This unsteadiness and variability of the flow can affect wind farm power optimization. Iungo found from wake measurements of a 3 bladed model turbine that the hub vortex oscillates sinusoidally only in the near wake [72] in agreement with others [89, 120]. Howard et. al. performed a PIV experiment with two turbines and found that near wake meandering is governed by interaction between bluff body hub vortex shedding and higher momentum fluid entrained along the tip vortex shear layer [67]. For a porous disk without a hub, España found that no defined periodic alternations takes place in a flow with high turbulence (12% turbulence intensity) in a simulated atmospheric boundary layer. The higher turbulence forces a weaker spectral energy peak. Contiguous vortices can be shed at different circumferential locations on a disk, and this non-deterministic feature can be affected by upstream turbulence intensity and velocity gradients [45]. This would imply that wake meandering exists, but with no defined periodicity. Medici found that for lower λ (tip speed ratios) the Strouhal number is large and the effective diameter of the turbine becomes smaller when the rotational speed is decreased [89]. In a 3x3 experimental wind farm array set up by Coudou, the Strouhal number was found to be $St = \frac{f_s D}{U_{hub}} \approx 0.20 - 0.22$ [38]. Similar peaks in Strouhal number were found by Heisel et. al. [65].

The unsteady properties of the wind turbine wake have been studied by Muller et. al. with a hotwire rake and two porous disks who looked at the ability of the wake to follow the large turbulent eddies contained in the approach flow [91]. Similarly, 2D LiDAR measurements were made in the wake of operational turbines at Denmark's Risø campus to verify this basic conjecture in their home grown Dynamic Wake Meandering (DWM) model. These measurements support that wake deficit is advected passively by the larger than rotor size eddies in the inflow [19, 20]. Many researchers have had difficulty quantifying the separate effects of large scale turbulence of incoming flow

and the local hub vortex on amplitude and intensity of wake meandering, especially in relevant turbine configurations such as the fully developed wind power plant [67]. It is known that upstream turbines confine the wake of downstream turbines which further increases the velocity deficit. This confinement also sometimes produces acceleration between the turbines due to the blockage effect, known as jetting. Higher performance was sometimes seen from turbines that end up in these non-aligned cases due to jetting in an LES torque controlled actuator disc simulation of the special case of Lillgrund offshore windfarm [39]. More often however, the turbines far into the array experience increased turbulence, unpredictable inflows, and a further power reduction.

It is expected that identification of large coherent structures in the prevailing wind of a site and within the array can inform the passive optimization of a wind farm via placement and spacing of wind turbines. Some researchers are working to integrate meandering knowledge into control systems in order to improve the wind farm monitoring and control and ultimately farm scale power production [119]. With further understanding of how the incoming flow and turbine wakes interact, increased array efficiency can be achieved by improving the turbulent mixing that enables wake recovery behind a turbine or series of turbines. Active optimizations are also possible with knowledge of how energetic structures are distributed and behave with the influence of a wind farm.

Through the high number of modes needed to capture half of the energy content of the flow in a POD analysis, Andersen recognized the structure of the wake is constantly morphing between highly complex shapes and is not merely a collective deficit translated by the incoming atmospheric flow [5]. Many high-fidelity flow simulation outputs show persistent meandering deep in the wind farms, where relatively smaller scale structures are present. Large scale motions are an integrated and inseparable part of the entire wake dynamics. It is likely that the downstream continuation of the meandering is provided via the intrinsic wind-turbine behavior [12]. It will be proven here that this meandering presents itself far downstream in large experimental arrays.

2.3 Goals and Outline

The purpose of this thesis is to address two main goals

1. **In a large regularly spaced wind farm, for a given configuration of turbines, at what point does the array reach a fully developed condition?**

2. **Does wake meandering still exist in a fully developed wind farm, and how does it present itself?**

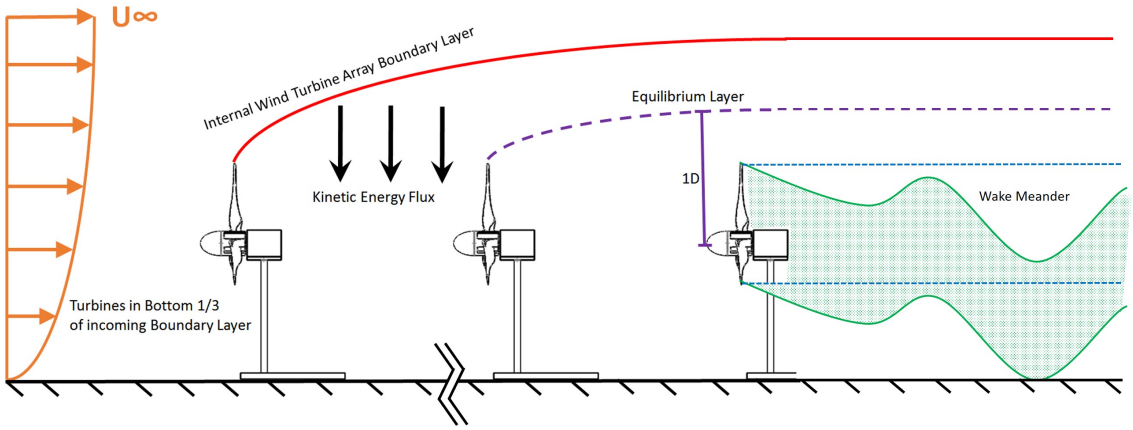

Figure 2.9: Diagram of wind turbine array boundary layer physics discussed in this thesis

The diagram in Figure 2.9 represents the topics covered in this thesis. The line drawn turbines are setup in a boundary layer flow. The turbines produce their own internal wind turbine array boundary layer. Far downstream, represented by the break in the floor, the equilibrium layer is carefully probed to reveal the fully developed wind turbine array boundary layer condition. Within the fully developed condition, and downstream of individual model turbines in boundary layer flow, wake meandering is characterized.

This thesis is arranged by first discussing experimental setups in Chapter 3. Next, an expanded experimental uncertainty is provided in Chapter 4. In Chapter 5, the fully developed wind turbine array boundary layer condition is investigated via mean velocity measurements. In Chapter 6,

wake meandering is investigated downstream of a single model turbine and within a wind farm array. The thesis concludes with a summary and future work recommendations in Chapter 7.

CHAPTER 3

METHODS

This chapter describes the test facilities, turbine models, data acquisition instruments, and experimental setups used in this thesis. Setup information is presented here for three experimental campaigns discussed in this thesis. Data sets discussed here include a pitot tube measurement campaign that is the focus of Chapter 5, a single wire hot wire study in the wake of a single model turbine in a boundary layer wind tunnel and a single wire hot wire study within the flow of a wind turbine array in a boundary layer wind tunnel, the latter two being the focus of Chapter 6.

3.1 Facilities

Most of the work in this thesis was performed in the University of New Hampshire Flow Physics Facility. The Blue Wind Tunnel was used for drag testing on model turbine rotors.

3.1.1 Flow Physics Facility

The single model turbine wake studies and turbine array studies were conducted in the University of New Hampshire (UNH) Flow Physics Facility (FPF). The UNH FPF is a large turbulent boundary layer wind tunnel, with sufficient flow quality to enable study of high Reynolds number boundary layer flow. The view from outside the facility looking at the inlet can be found in Figure 3.1. The test section measures 6.0 m (W) x 2.7 m (H) x 72 m (L). In its present state (Phase 1, open return), test section velocities of up to 14 m/s can be achieved with free stream turbulence intensities less than 0.5$\%$ at all downstream locations. The tunnel is powered by two 400 horse power fans capable of moving 250,000 cubic feet per minute each. Naturally grown turbulent boundary layers on the order of 1 meter thick with the correct range of scales, and Reynolds numbers based on boundary layer scale ratios, $\delta^+ \equiv u_\tau \delta/\nu \approx$ 20,000 with $\eta = \nu/u_\tau \approx 35 - 40$ μm (corresponds

Figure 3.1: External view of the Flow Physics Facility looking at the test section inlet

to $\delta = 0.7 - 0.8$ m) can be achieved towards the downstream end of the test section. Spanwise variation in friction velocity measured with a Preston tube is less than +/- 0.5% when outside of the side wall boundary layers. The boundary layer is tripped with 1/4"-20 threaded rods on the floor and two side walls. The ceiling of the test section slopes slightly upward to compensate for the growth of boundary layers on the floor, two side walls and ceiling, and establish a zero pressure gradient for operation with an empty test section (i.e., turbulent boundary layer experiments). Details of the FPF and qualifying wind tunnel boundary layer measurements are reported in Vincenti et al. [114]. The FPF is situated outdoors and is a single pass open to atmosphere facility. Changes in weather conditions over the course of a data set such as inlet temperature, barometric pressure and humidity all affect the flow. This provides unique challenges discussed in Chapter 4.

3.1.2 Blue Wind Tunnel: ELD Model 404c

Drag measurements for the porous disk were conducted in the Model 404c Eiffel-type Blue Wind Tunnel from Engineering Laboratory Design (ELD) [43]. Figure 3.2 shows the UNH Blue Wind Tunnel diagram. This is a in-draft type tunnel with internal test sections dimensions of 18" x 18" x 36" and flow speeds ranging from 0 – 40 m/s. The test section of the Blue Wind Tunnel

Figure 3.2: Photograph of UNH Blue Wind Tunnel. Flow is from left to right. Photo is taken from the fan end of the tunnel.

is fitted with 3/4" thickness, clear, GM grade, acrylic plexiglass to allow for a safe viewing area Air is drawn by a axial fan powered by a 40 HP cariable speed, DC Reliance motor and controller into the settling chamber through a flared inlet and passed through a combination honeycomb and screen flow conditioner before being accelerated through the contraction section into a Plexiglas test section. The bottom of the test section is removable for placement of instruments and the top of the test section has an input for a pitot tube to measure free stream velocity. The flow then passes through the diffuser section into the fan and is discharged through the silencer and into the room. The tunnel is located in Kingsbury Hall at the University of New Hampshire and is exposed to the conditions of the climate control in the room where it is located. The tunnel is painted blue and will be referenced as the Blue Wind Tunnel.

3.2 Model Turbines

The experiments conducted for this thesis utilized 0.25 m diameter (D) scaled model wind turbines and porous disks. The turbines were chosen to be quarter meter in diameter due to the scale of the boundary layer in the FPF. A typical inflow condition for a real wind farm is that the atmospheric surface layer thickness is greater than three times the wind turbine hub height ($\delta/H_{hub} > 3$), which is replicated in the model array in the FPF. The porous disks were drag (thrust) matched to blade element momentum theory designed 1:500 scaled model turbines of 5 MW offshore wind turbines created for a previous study [34].

3.2.1 Rotating Bladed Turbine Design

The 0.25 m diameter model wind turbines used in this study are 1:500 scale models of turbines with a rotor diameter of 125 m, which is approximately equivalent to a 5 MW turbine (e.g., NREL 5 MW offshore reference wind turbine [76]). The airfoil chosen for the blades was a NACA 2412 with the following distribution of twist angle and chord length at various normalized radii seen in Table 3.1. The blades and hub assembly were 3D printed with ABS plastic with a rapid

r/R	Twist Angle (deg)	Chord Length (m)
0.00	40.3	0.0732
0.14	28.8	0.0583
0.25	21.4	0.0475
0.36	16.4	0.0396
0.46	12.8	0.0338
0.57	10.2	0.0295
0.68	8.1	0.0260
0.79	6.5	0.0233
0.89	5.2	0.0211
1.00	4.1	0.0193

Table 3.1: Blade design characteristics

protyping tolerance of 0.002 inches. For the turbine array studies, the turbines were mounted with hub height at 0.75 times the turbine diameter, or 0.1875 m, which is representative of offshore

wind turbine installations. Since it is not possible to simultaneously achieve geometric, kinematic and dynamic similarity at this scale, the turbines were designed with the goal to approximate the non-dimensional performance parameters of full scale turbines, i.e., power coefficient C_P, tip speed ratio λ and drag (thrust) coefficient C_T. The turbine rotor/blades were designed using blade element momentum (BEM) theory [88].

In previous studies, the performance of the turbine was characterized, in a free stream and inside the boundary layer in the FPF. Both the thrust coefficient and power coefficient were quantified. In these past experiments, the rotational speed of the turbine was controlled using a variable resistor and the power was measured using a multimeter. Rotational speed was computed using the voltage constant of the motor and a tachometer for redundancy. The thrust was measured using a custom built force balance equipped with an OMEGA LCEB-5 load cell connected to a DATAFORTH Corporation DSCA38-02 signal conditioning module. The model wind turbine was able to achieve a thrust coefficient of $C_T \approx 0.73$ and a coefficient of performance of $C_P \approx 0.33$ measured in the free stream at a tip speed ratio of 3.5. Details of the turbine design and results from various performance tests are given in [17, 33].

3.2.2 Porous Disk

The porous disks were drag (thrust) matched to the spinning model turbines and their wakes were compared for the purpose of building up an array of porous disks and spinning model turbines. The porous disks have 0.1875" (4.76 mm) diameter holes with a 0.25" (6.35 mm) center to center spacing, with a 60 degree staggered center hole arrangement, resulting in an open area of 51%. They are made of Type 304 stainless steel, with a thickness of 0.0480" (1.22 mm) (McNichols Perforated Metal). The porous disk hub height is also located at $0.75D$ from the floor. The porous disk does not spin. The two objects are compared near the end of the test section of the FPF in Figure 3.3.

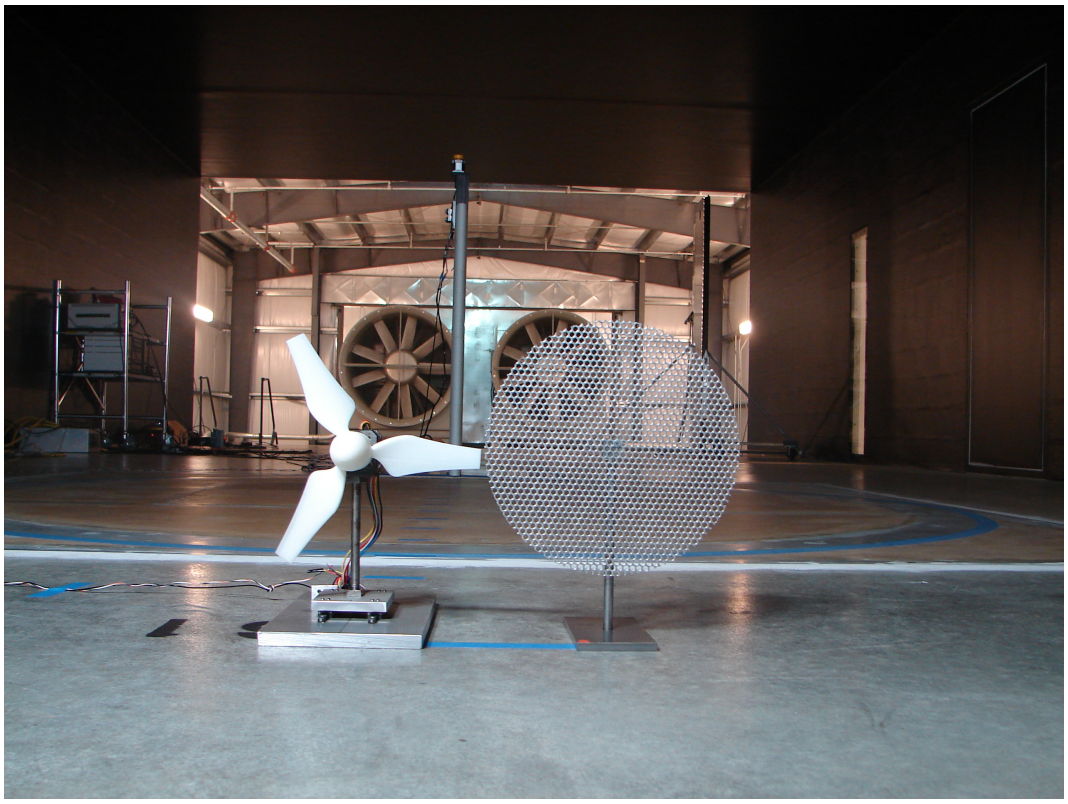

Figure 3.3: Side by side view of the porous disk and the rotating model turbine pictured in the rear of the FPF test section (61 m downstream of the inlet) looking downstream. Both models have diameter $D = 0.25$ m and hub height of 0.75 times D.

3.2.2.1 Disk Drag Measurements

The drag (thrust) coefficient of the porous disk used was measured as $C_T = 0.92$ in a uniform inflow in the Blue Wind Tunnel, at Reynolds numbers comparable to what the porous disk model would encounter at hub height at the first row of the array. This value is consistent with recent measurements and predictions from Hultmark and Steiros [107].

The thrust was measured using the built in linear force balance attached to the Blue Wind Tunnel equipped with an OMEGA LCEB-5 load cell connected to a DATAFORTH Corporation DSCA38-02 signal conditioning module. Drag was calculated by first obtaining voltage versus force calibration measurements of the force meter by hanging masses of known weights off a calibration rig that allowed force only in the stream wise direction. The calibration was then

applied to varying velocity measurements of only the stand in the test section. The stand is a 3/8" 1566 steel rod used for mounting the disks. A graph of force versus speed of the stand is used to remove the effect of the stand and isolate the drag of the disks. Figure 3.4 shows the coefficient of drag versus Reynolds number for the stand. At a Reynolds number independent regime of ≈10,000 the coefficient of drag for the stand is 1.39.

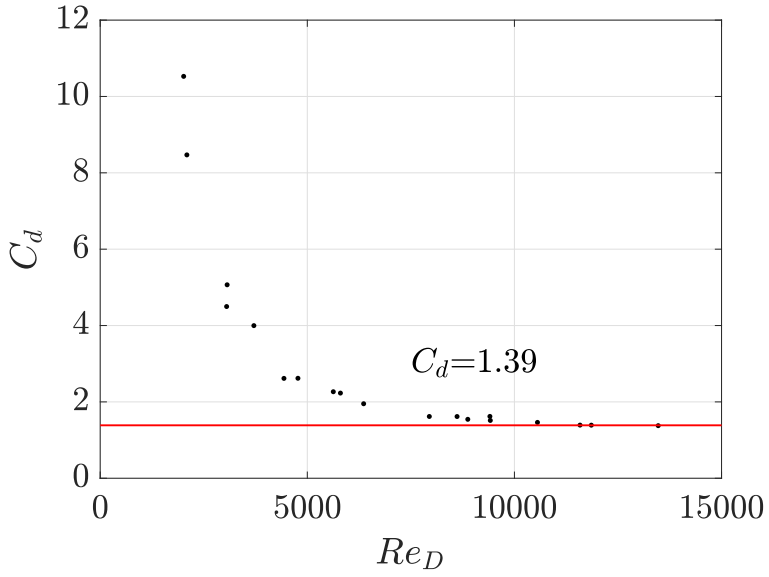

Figure 3.4: Coefficient of Drag versus Reynolds number with respect to cylinder diameter for the stand in a uniform flow

For drag testing in the Blue Wind Tunnel, disks of 3" and 5" were cut from the same porous plate stock used for the 0.25 m diameter disks. The 5" and 3" diameter disks were mounted on the stand and force measurements were obtained at various wind tunnel speeds. A plot of the force on the two diameters of porous disks can be found in Figure 3.5. A trend line was calculated based on the velocity measurements of the stand. The corresponding force as a function of velocity from the stand were subtracted to obtain coefficients of drag on the disks. The Reynolds number based on diameter was calculated and plotted versus the coefficient of drag and the average of the last 5 points of each disk size was averaged to obtain C_D. For the disks, coefficient of drag versus Reynolds number based on diameter is shown in Figure 3.6. The data is presented for 3" and a 5" diameter porous disk. The lower Reynolds number flow has a larger coefficient of drag and

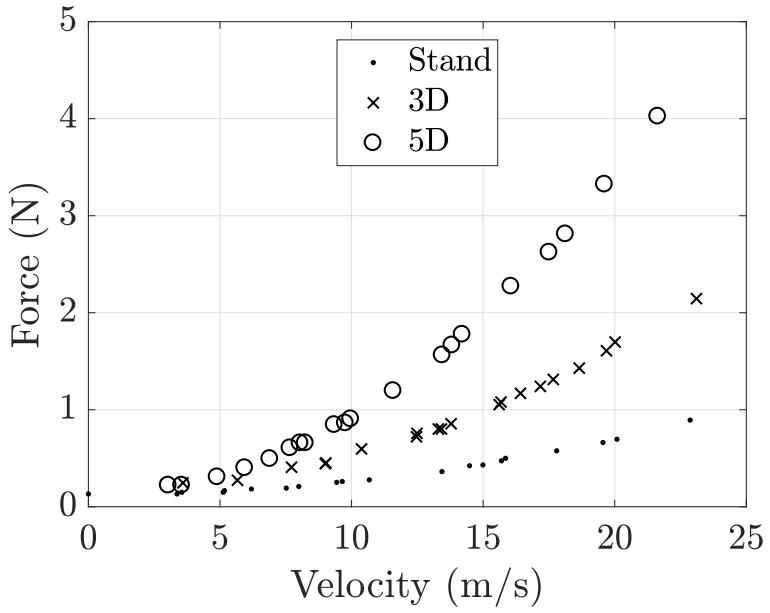

Figure 3.5: Force in Newtons versus Velocity for a 3" diamater (here 3D) and 5" diameter (here 5D) porous disk and the holding stand in a uniform flow.

with increasing speed, the coefficient of drag levels off to a near constant value of $C_D = 0.92$. An aim of these drag measurements was to capture the Reynolds number comparable to what the 0.25 m diameter porous disk model would encounter at hub height at the first row of the array in boundary layer flow in the FPF. This value is approximately $Re_D = \frac{UD}{\nu} = 75,000$ using a hub height velocity of 4.5 m/s. As can be seen in the figure, the range around 75,000 is captured, but the coefficient of drag may not yet be leveled off.

3.3 Experimental Setups

This section will discuss three experiments. Data sets discussed here include a pitot tube measurement campaign that is the focus of Chapter 5, a single wire hot wire study in the wake of a single object in a boundary layer wind tunnel and a single wire hot wire study within the flow of a wind turbine array in a boundary layer wind tunnel, the latter two being the focus of Chapter 6.

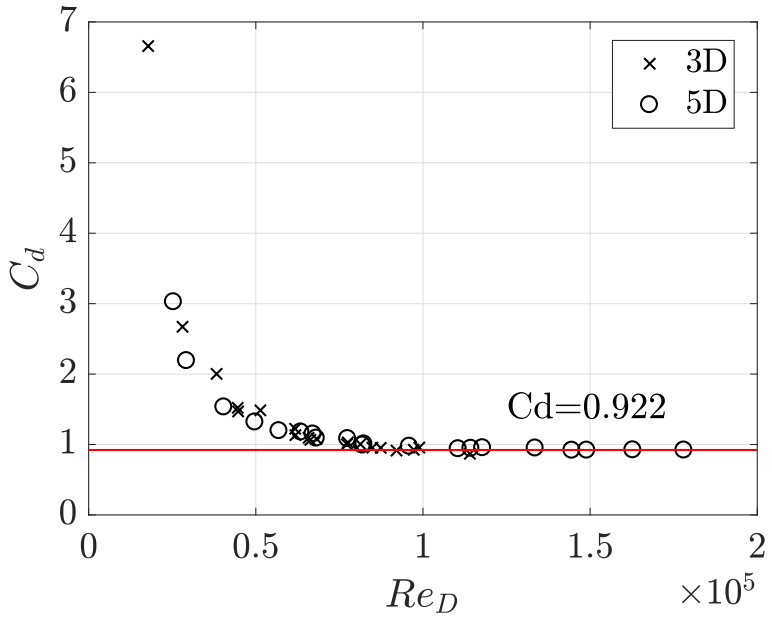

Figure 3.6: Coefficient of Drag versus Reynolds number with respect to diameter for a 3" and 5" diameter porous disk in a uniform flow. 3" diameter disks are indicated with an "$\times$" and 5" disks are indicated with a "$\circ$".

In this thesis, many of the measurements and locations are discussed in reference to the turbine diameter D. As an example, an x/D location would imply downstream distance with respect to Diameter, so $x/D = 8$, would be 2 m in SI units.

3.3.1 Disk Array Setup for Mean Velocity Measurements

An array of 95 porous disks was setup in the FPF to obtain the mean velocity measurements for Chapter 5. The model turbine array consisted of 19 aligned rows in the stream wise direction and 5 columns in the span wise direction. The disks are aligned facing the mean wind direction with a spacing of $8D$ in the stream wise and $4D$ in the span wise directions, respectively. This stream wise and span wise spacing of turbines in the array is typical of arrangements in real arrays and is typical of the turbine spacing used by modelers. The incoming boundary layer flow was artificially thickened using a set of 11, one meter tall Irwin spires, which were positioned at 5 m downstream of the wind tunnel turbulent management section [70]. The first row of the model turbine array entrance is positioned 28 m downstream of the spires (33 m from test section entrance) which

allows for additional boundary layer growth. The boundary layer profile at the model array inflow (2 turbine diameters upstream of the first turbine row) satisfies the criteria for an atmospheric boundary layer (mean velocity, turbulence, energy spectrum) according to ASCE Standard 49-12, as discussed in 5. A typical inflow condition for a real wind farm is that the atmospheric surface layer thickness is greater than three times the wind turbine hub height ($\delta/H_{hub} > 3$), which is replicated in the model array in the FPF.

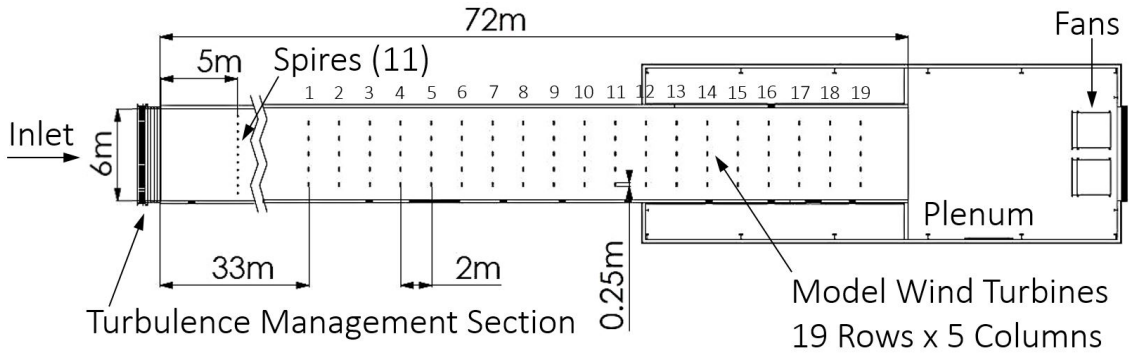

Figure 3.7: Top down cutaway view of UNH FPF with 19 x 5 array of model turbines. Spires are installed 5 m downstream of the turbulence management section. Flow is from left to right.

Figure 3.7 shows a top down schematic of the FPF with the model turbine array layout and relevant dimensions. The flow is from left to right, from the turbulence management section at the inlet to a low pressure plenum section with two fans at the end. Note that for figure legibility, approximately 26 m of the test section length were cut away (from $\approx 6 - 31$ m in the stream wise direction). An image of the porous disk array setup inside the FPF is found in Figure 3.8.

Velocity measurements were performed in the center row of the model array. Vertical profiles were measured at $6D$ downstream of each turbine model for the first 17 rows in the 19×5 array. This stream wise measurement location puts the vertical profiles at $2D$ upstream of the next turbine row. A diagram of data point locations in reference to an example disk is shown in Figure 3.9. The vertical spacing of the points in the figure are to scale, but they are placed closer downstream to the disk than in the physical experiment. Table 3.2 lists the number of points and spacing distributions, as well as starting and ending location in reference to the vertical distance from the floor. Recall

Figure 3.8: Photograph of the porous disk wind turbine array setup in the FPF. Looking downstream towards the low pressure plenum. Photo taken by Jeremy Gasowski

the turbine hub height is 0.1875 m (0.75 D) from the floor. For the experiments reported here, the FPF fans were operated at 600 RPM, corresponding to a nominal free stream velocity of 6.7 m/s. Attention is given to the equilibrium region located just above top tip height, spanning measurement region II which has finer spacing (0.10 D) [31]. The initial spatial conditions of the array and spires were kept constant throughout the experiment. The full array was setup throughout testing.

Region	Spacing	Number of Points	Starting Location (m)	Ending Location (m)
I	0.25D	4	0.125	0.3125
II	0.10D	5	0.3125	0.4375
III	0.25D	10	0.4375	1.0625
IV	0.50D	5	1.0625	1.6875

Table 3.2: Point spacings of vertical profiles. Starting and ending locations are referenced from the floor.

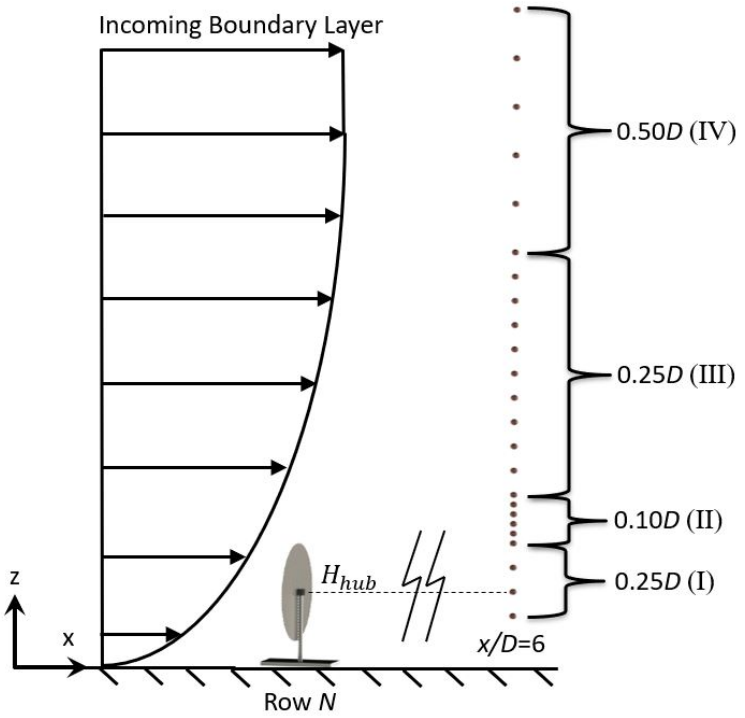

Figure 3.9: Velocity measurement locations, with spacing in turbine diameters D. Second point above the wall is at turbine hub height.

3.3.1.1 Pitot Tube

A Pitot static tube was used as the primary instrument to measure velocity profiles in the FPF presented in Chapter 5; the reasoning for this is further discussed in the chapter on measurement uncertainty (4). Pressure measurements were made with a MKS Baratron 698A Differential Pressure Transducer. A 16-bit Data Translation 9836 DAQ sampled at 100 Hz for 6 minutes per point, 24 points per profile. The pressure transducer data was corrected in post-processing for temperature at each point, barometric pressure per profile and humidity per profile [23]. These corrections are required due to the open return configuration of the FPF.

The Pitot static tube was attached to a sting, positioning it 0.5 m upstream of a 2.4 m tall vertical traversing system produced by Hambleton Instruments. The stepper motor which controls the vertical linear rail system is controlled by a Phidget motion controller. To move to new streamwise measurement locations, the entire traversing system was moved in the streamwise direction in the center of the tunnel, while the model turbine array remained in the same position. The local

free-stream velocity was measured at a height of 1.7 m from the floor (about 60% of wind tunnel height) with a second Pitot-static tube. Temperature was measured with a k-type thermocouple at the same height as the traversing Pitot tube. A detailed calculation using Bernoulli's equation to find velocity using a pressure transducer can be found in Chapter 4.

To measure the inlet of the array for comparison with a standard incoming atmospheric boundary layer, a single wire hotwire was used. A single wire hotwire, 5 μm Tungsten with a 1 mm active length, and an AN-1003 AA Labs constant temperature anemometry (CTA) system were used to measure a velocity profile at the inlet of the wind turbine array at $x/D = 2$ upstream of the first turbine row. The hotwire sampled at 1 kHz for 6 minutes per point.

3.3.2 Single Model Wind Turbine Wake

Wake comparison experiments between the spinning model turbine and the porous disk were conducted in the UNH FPF. Measurements were performed with the turbine or disk in the turbulent boundary layer towards the end of the test section at various downstream locations. The boundary layer is allowed to develop 62 meters before interacting with either a rotating model turbine or porous disk. The boundary layer height at this location is approximately 0.8 m which fully immerses the object in a shear flow and puts the hub height of the object in the bottom 1/3rd of the boundary layer. Again for this study, the variable frequency drives for the fans in the FPF were set to 600 RPM which equated to a free stream velocity of approximately 6.7 m/s. Vertical profiles of 67 points at were obtained with a custom built vertical traversing system at span wise center line of the object. The first 60 points (region A) were linearly spaced between 1 cm from the floor and 0.6 m at a spacing of 1 cm. The final 7 points (region B) were spaced at 5 cm and ended at a vertical height of 0.95 m. This information can be seen in Table 3.3. The profiles were taken at 8 different locations downstream of the disk and turbine spaced by diameter as follows: $x/D = 1$, 2, 4, 6, 8, 10, 14, and 20.

Region	Spacing	Number of Points	Starting Location (m)	Ending Location (m)
A	0.04D	60	0.01	0.60
B	0.20D	7	0.60	0.95

Table 3.3: Point spacings of vertical profiles for the profiles of wakes of single model turbines or porous disks. Starting and ending locations are referenced from the floor.

3.3.2.1 Single Wire Hotwire Anemometry

Velocity measurements were performed with an in house constructed single wire tungsten constant temperature hot-wire anemometer probe measuring 5 μm in diameter with an exposed active length of 1 mm. The hot-wire was attached to a sting, positioning it 0.5 m upstream of a vertical traversing system, and connected to an AN-1003 AA Labs anemometry system. Each point was sampled for 60 seconds at high enough temporal resolution (10 kHz) to capture the spectral density of the velocity time series. The hot wire was calibrated in the free stream against a pitot-static tube before and after each profile. Temperature was acquired during each calibration and throughout each profile. The hot wire was calibrated by a linear interpolation corresponding to the change in temperature from the before and after calibration. If the temperature varied more than 2°C between the before and after calibration, the profile was rejected and repeated. The traverse was streamlined using 3-D printed ABS plastic airfoils. The vertical traverse was controlled using a stepper motor and a NI MID-7604 controller. An image of a single porous disk in the boundary layer flow can be seen in Figure 3.10. An incoming boundary layer profile before interaction with one of the single objects obtained at 62 m downstream of the inlet is shown in Figure 3.11. The incoming profile is spaced vertically in the same manner as the wake data obtained downstream of the single objects.

It was determined that the wake of the spinning model turbine and the porous disk in a boundary layer flow becomes sufficiently similar after $6D$ downstream and therefore can be used to build up a large array containing both objects and was published in [34].

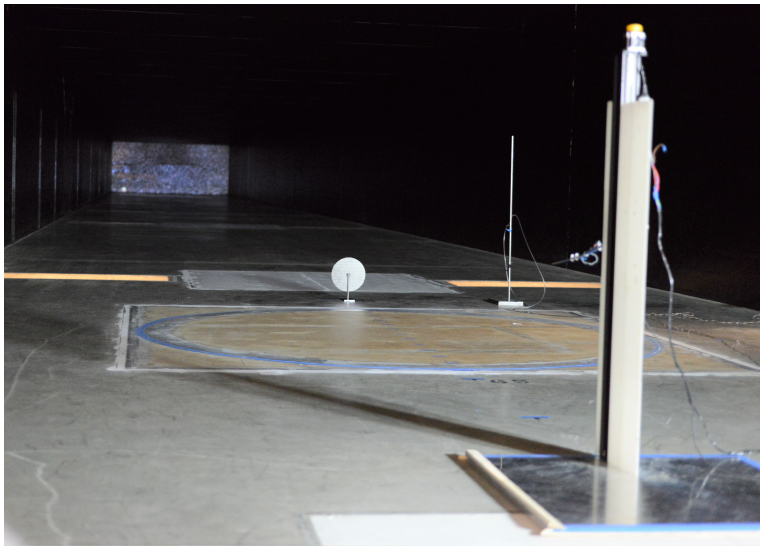

Figure 3.10: Photograph of the porous disk in a boundary layer flow with traversing system in foreground of photo with sting holding a single wire hot wire for wake measurements. Photo is taken looking upstream with the test section inlet in view. Disk is positioned near the end of the test section.

3.3.3 Disk and Turbine Array

To study wake meandering in the wind turbine array boundary layer, hot wire measurements were performed in an array of the model wind turbines and porous disks. A total of 9 model turbines and 86 porous disks were used for this study. The disks and turbines were set up in large arrays in the UNH FPF of 5 columns and 19 rows. The large test section of the FPF allowed for variable stream wise spacing and array size. The turbines and disks where aligned to within ± 1 mm which corresponds to ± 0.5 m full scale. More on the placement of the turbines can be found in Section 3.3.4. Measurements were taken within the array using the same hot wire and traversing system as for the single wake comparisons.

The model turbines were arranged in a 3×3 array within the array of porous disks. All velocity profiles were measured downstream of the last (third) row of turbines at span wise center line. This 3×3 array reintroduces the rotating wake components of the flow and helps correct for any turbulence differences in the porous disk and the turbine wake. A schematic of this setup is shown in Figure 3.12. The schematic is a rendering of the FPF that includes the drag balance plates

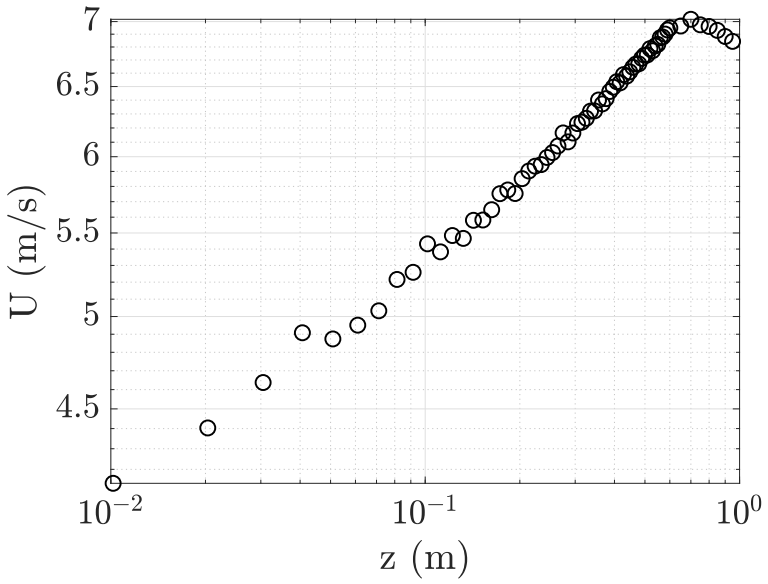

Figure 3.11: Incoming boundary layer velocity profile

in the floor indicated by the ≈2 m × 2 m rectangular white tiles and the turntable indicated by the wooden ≈3 m × 3 m rectangular plate in the floor. Note that two dummy rows of turbines (porous disks) were placed downstream of the measurement region to establish the proper flow resistance and prevent the flow from prematurely expanding and decelerating in the measurement region. A spanwise spacing of 4 diameters ($S_y = 4D$) was used for all array studies. This span wise spacing allowed for the maximum amount of span wise tunnel space to be used without major influence from tunnel wall effects. Two stream wise spacings were investigated, 8 and 10 diameters ($S_x = 8D, 10D$). Four different array sizes were used: 19×5, 14×5, 9×5, and 5×5, with velocity profile measured at center line downstream of the 17^{th}, 12^{th}, 7^{th} and 3^{rd} rows, respectively. The vertical point spacings can be seen in Table 3.4. Region 1 is comprised of 21 points of $0.04D$ spacing that notably begins at model turbine hub height. Region 2 is comprised of 53 equally spaced points of $0.08D$. Note that the intention of this study is to mainly to capture the flow physics and wind turbine array boundary layer dynamics at the top tip of the turbines and above the array and therefore the near wall points are not included. The array is built up by placing 5 rows of turbines at a time in front of the rotating array that is left in place. In this way, we simulate

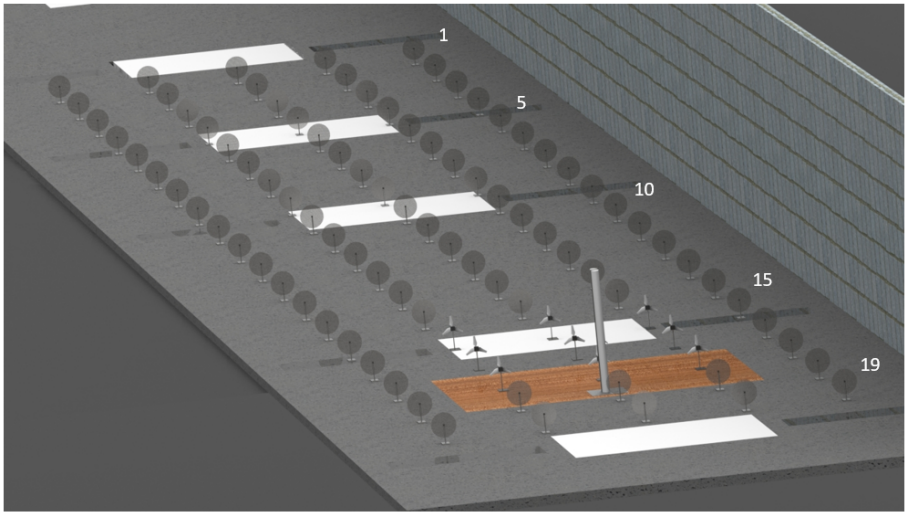

Figure 3.12: Rendering of the 19×5 array setup in the UNH FPF. Rows labeled at right. Flow is from upper left to lower right. 3×3 array of spinning scaled turbines can be seen next to tall white traversing system.

traversing downstream through the array while maintaining a single downstream position in the wind tunnel.

Region	Spacing	Number of Points	Starting Location (m)	Ending Location (m)
1	$0.04D$	21	0.1875	0.3875
2	$0.08D$	53	0.3875	1.4475

Table 3.4: Point spacings of vertical profiles for the profiles of the combined turbine and porous disk array. Starting and ending locations are referenced from the floor.

3.3.4 Turbine Placement

For the placement of the model turbines and disks in an array setup, a grid was drawn on the floor of the FPF in one meter spacing throughout the entirety of the test section. The grid was painted with small crosses at every meter both span wise and stream wise, where the inside bottom left corner of the cross indicates the dead center location for that point as seen in Figure 3.13. The paint used was an oil based model paint with an estimated thickness once dried of $1/10^{th}$ mm. This thin oil paint was chosen to make the smallest impact on the flow physics of the smoothness of the

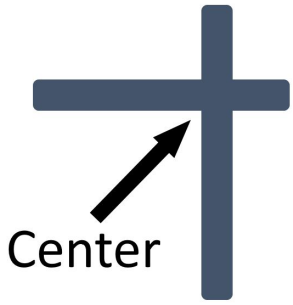

Figure 3.13: Example of grid marks painted on the floor of the FPF with the centerline indicated. Not to scale.

concrete floor, but still be robust enough to adhere to very smooth concrete and stand up to harsh temperature and humidity variations the tunnel undergoes.

First, a centerline had to be established in the tunnel. Although the architectural drawings have the FPF floor as 6 m wide, the as-built varies slightly ($\pm$ 5 cm) as measured with a steel tape, and a center line had to be redefined to ensure alignment. The center of the inlet and the end of the test section was determined and a fiberglass open reel tape measure was laid down the center of the test section and taped down including 3 inch hexbar weights (cut up into 4 inch pieces) every 20 meters. Next, one meter spacing were determined with a steel tape and steel meter stick outwards from the centerline to establish five total markings in the steamwise direction. Braided nylon mason line was then stretched down the test section at these four additional locations and anchored by wrapping it around a 1 m long 3 inch hexbar weighing $\approx$ 50 lbs each. The mason line was then checked at various locations down the tunnel test section in relation to the established centerline with the steel tape and steel meter stick. It was then anchored every 20 meters with smaller sections of the hexbar. To ensure minimal spanwise variability, a laser line was used in conjunction with a T ruler and square. Each spanwise laser line was squared and used for five markings across the six meter wide test section. The steel tape was also used to check the diagonals of the intersection of the laser line and mason line.

A jig was machined out of $1/8^{th}$ inch steel with a 2 inch by 1 inch cross milled out of the center and cross hair etching. See Figure 3.14 for a photo of the physical jig. The etching on the

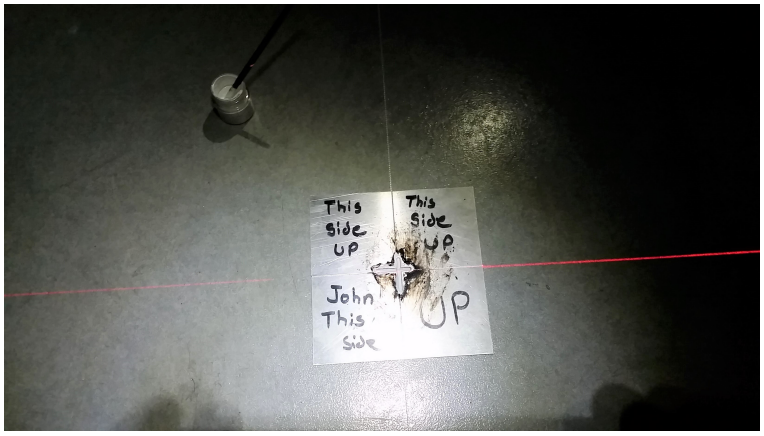

Figure 3.14: Photograph of jig in use for painting crosses to grid the FPF. Mason line and laser visibly intersecting.

jig was able to hold the mason line, which was tight enough to spring back into place if moved unintentionally, and the laser line fell onto the perpendicular cross hair. With the jig in place, the milled cross was filled in with a minuscule amount of the oil paint, and the mason string or anchored measuring tape were immediately removed to allow the paint to dry. As stated, the edge of the bottom right corner of the cross is the location of dead center for the intended point. This process was repeated 350 times to grid the test section, which did not include the initial boundary layer trip or the last set of five crosses at the end of the test section at 72 meters. An image of this process is shown in Figure 3.15.

Another jig was created for the placement of the turbines. The jig had the same size and shape for the crosses painted on the FPF floor and could be laid directly over the painted markings. The jig was the same size as the base of the turbines and the initial crosses are long enough that alignment with this jig is simple. Once the turbine placement jig was down, a thin edge line in the corner of the jig could be drawn on the FPF floor, and this marking is where the turbines would be aligned when placed in the array seen in Figure 3.16.

After the entirety of the tunnel was gridded, no variation was found using the steel measuring tape on perpendiculars or diagonals of greater than 1 mm or $\Delta x/D = \pm 0.4\%$. See Figure 3.8 for a qualitative visual of turbine placement in the aligned array.

Figure 3.15: Example of laying the grid used for turbine placement

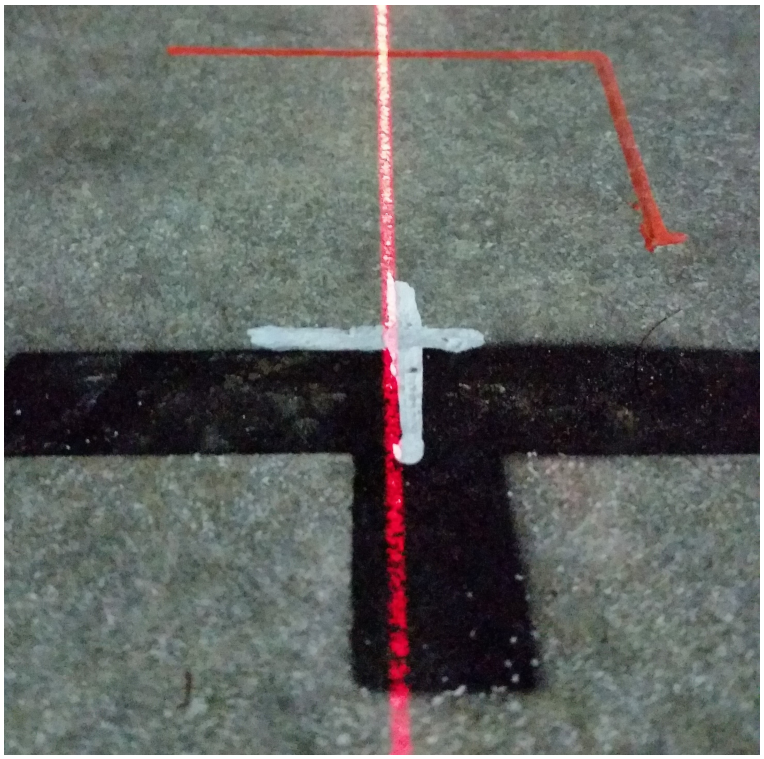

Figure 3.16: Grid floor cross marking with turbine edge drawn

CHAPTER 4

UNCERTAINTY

The quantification of uncertainty in velocity measurements is critical in experimental fluid mechanics, especially when dealing with a complex flow such as the wind turbine array boundary layer. The presence of the turbine array creates complex wake and incoming boundary layer interactions and the shear off the top tip of the turbines contributes to the creation and growth of an internal wind turbine array boundary layer. Due to the complex nature of the continually developing outer region of boundary layer flow, even a slight change in initial or boundary conditions can have large consequences on the region of interest. Studies in turbulent flows almost always require quantities to be represented as ensemble averages because representing instantaneous turbulent processes create confusion [53]. Appropriate bounds must be placed on data accuracy. A careful consideration of uncertainty is especially warranted here due to the open to atmosphere nature of the experimental facility and the duration of the experiments. Each velocity profile took about three hours to complete, including data collection and traversing time, during which significant variations in ambient temperature could occur. Additionally, the experiments were conducted over the course of several weeks.

Uncertainty estimates from the experimental investigation discussed in Chapter 3 of a scale model wind turbine array, conducted with (on the order of) 100 0.25 m diameter model wind turbines in a high Reynolds number turbulent boundary layer facility, are reported. An expanded uncertainty analysis using the Taylor series method is executed to predict uncertainty for the system of interest in the mean flow. This expanded uncertainty prediction was confirmed by a Monte Carlo simulation. A workable comprise has been found between data acquisition time and uncertainty, mitigating changing initial conditions due to exposure to atmospheric conditions and temperature drift. Flow measurement techniques pitot tube and hot wire anemometry were compared showing

increased uncertainty with increased complexity of instrumentation. The goal of this chapter is to accurately determine the uncertainty associated with open to atmosphere wind tunnel data for use in validation of numerical models and show that this experimental array is sufficiently large to converge on a statistically stationary state in the mean to within our confidence level.

4.1 Experimental Variability

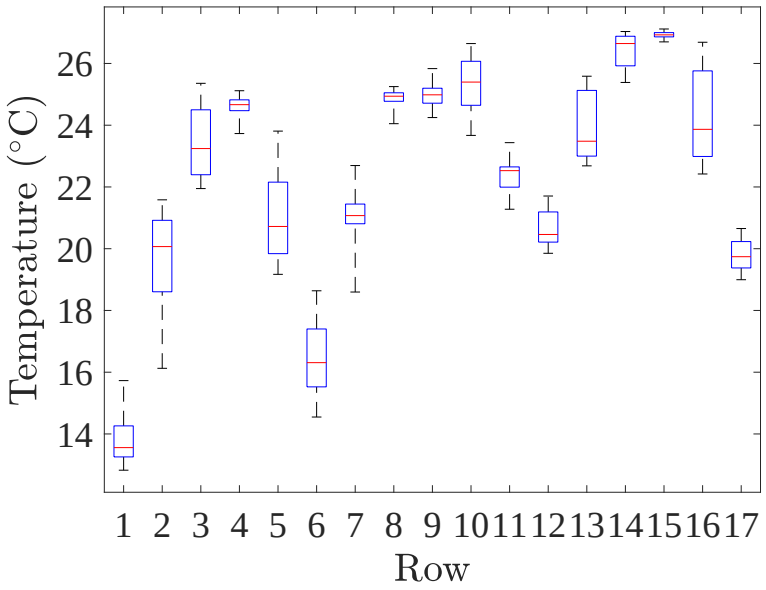

Figure 4.1: Temperature average, and extreme values over every point per profile, indicated by turbine row number

Figure 4.1 shows temperature data for the experiments, obtained with a k-type thermocouple. This data set helps visualize of the need for an uncertainty analysis. This temperature data is obtained simultaneously with pitot tube measurements in the porous disk array. The thermocouple is located on the sting that positions the pitot tube, essentially at the pitot tube measurement location. Figure 4.1 shows a set of box and whisker plots of each of 24 six minute per point mean temperature over a profile at a designated row number. The temperature median over the entire profile is represented by the red center line in the box plot. The edges of the box are the 25^{th} and 75^{th} percentiles and the whiskers extend out to the most extreme 6 minute mean data point for a given profile. While temperature remained relatively constant during a few velocity profiles,

there is significant temperature variation during most profiles, and significant day-to-day variation. Visually, the scatter of temperature is evident within a single profile. A profile spans about 3 hours of combined data collection and traversing time, and there is time between profiles which can be taken on different days with different weather conditions. Figure 4.1 clearly shows that the variable inlet conditions of an open-return facility must be reconciled, and is a good visual representation of the need for an uncertainty analysis.

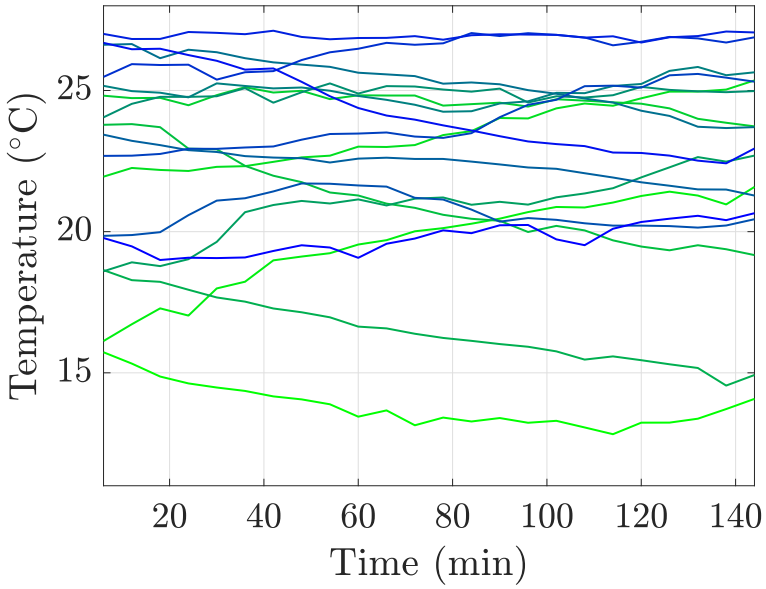

Figure 4.2: Temperature versus time over the course of every profile, with temperature averages. The profiles go from $x/D = 6$ downstream of row 1 being the most green to $x/D = 6$ downstream of row 17 being the most blue.

Figure 4.2 shows the temperature over the time span of each profile. It is captured here that temperature does not always vary linearly, or even monotonically, with time. A few representative examples extracted from that figure can be found in Figure 4.3 where the profiles are labeled by row number. It can be seen for example, that the temperature over time of the data obtained at Row 1 decreases and then increases so a linearly interpolated calibration at two end points would not capture correctly the variation. Additionally in the data set of row 12 the temperature varies non monotonically. The data sets of row 2 is a monotonic increase, and the data set of row 16 is a monotonic decrease over the time span of the profile. With this temperature variation, using ther-

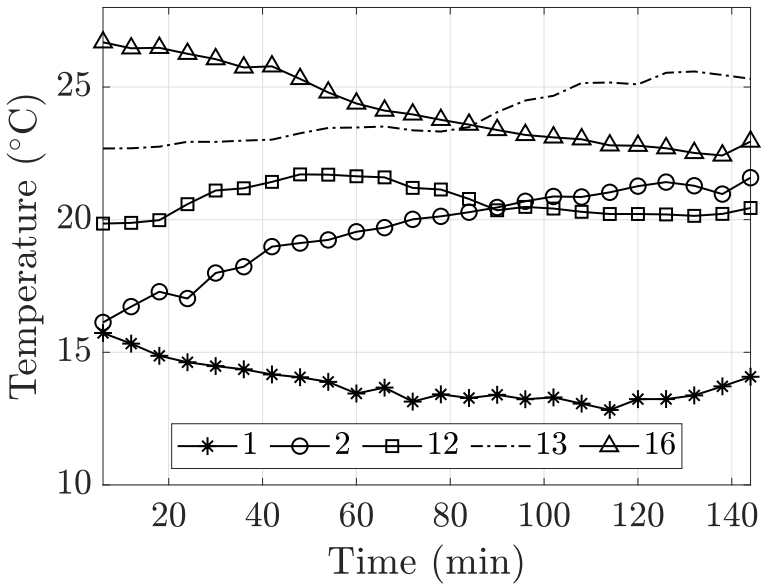

Figure 4.3: Temperature versus time over the course of representative profiles, with temperature averages.

mal velocity measurement techniques such as constant-temperature (hot wire) anemometry (CTA) becomes challenging. A typical hot wire calibration scheme would be to obtain calibration data before and after a velocity profile acquisition, and then linearly interpolate the voltage time series obtained to account for a linear temperature variation, then calculate velocities. In this case, this may result in erroneous interpolation of velocities due to the outdoor ambient temperature variation over a three hour window. Other schemes could be applied to calibrate hot wires, however the nonlinearity of this thermal technique with respect to ambient temperature variation provides challenges. One could suggest to reduce the data acquisition time to reduce the influence of changing weather conditions, but it is well known that shorter data sets decrease the trustworthiness of the mean. Therefore a balance must be found between data acquisition time to center in on the true mean, and drift of the mean itself. For this reason, a reduction in complexity was sought resulting in the decision to use a pitot tube for velocity measurements. The pitot tube velocity measurement depends on barometric pressure and density which are functions of ambient temperature. However, this calculation is affected less by temperature variation than thermal techniques which also rely

on the pitot tube for calibration. Thus, the high temporal resolution of hot wire anemometry was sacrificed for increased certainty of the true mean.

4.1.1 Representative Velocity Profile

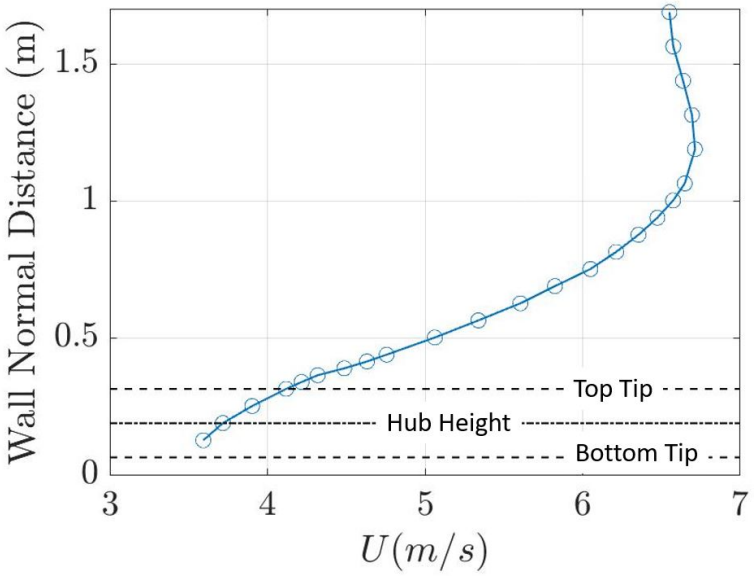

Figure 4.4: A representative velocity profile at $x/D = 6$ downstream of row 11

A representative velocity profile obtained with a pitot tube at a downstream location of $x/D = 6$ downstream of row 11 is shown in Figure 4.4. Horizontal single dashed lines indicate bottom tip height, and top tip height. Hub height is represented by a dot dashed line in between bottom tip and top tip height. The velocity profile shape approximates that of a boundary layer with modified near wall region due to the presence of turbines. Note that the study was not interested in very near wall boundary layer measurements and the first velocity data points is located at $\approx 0.16\delta$, where δ is the boundary layer height calculated by the vertical location at which 99% of the maximum velocity is achieved. The boundary layer height in Figure 4.4 is 1.06 m.

4.1.1.1 Ad hoc data acquisition length study

A study was performed at a single point in the representative velocity profile to determine an appropriate length of data acquisition. A time series totaling 20 minutes was obtained at 100 Hz at

a downstream location of $x/D = 6$ downstream of row 11 at top tip height. This time series can be seen in Figure 4.5. This long time series is broken up and the means are plotted in Figure 4.6.

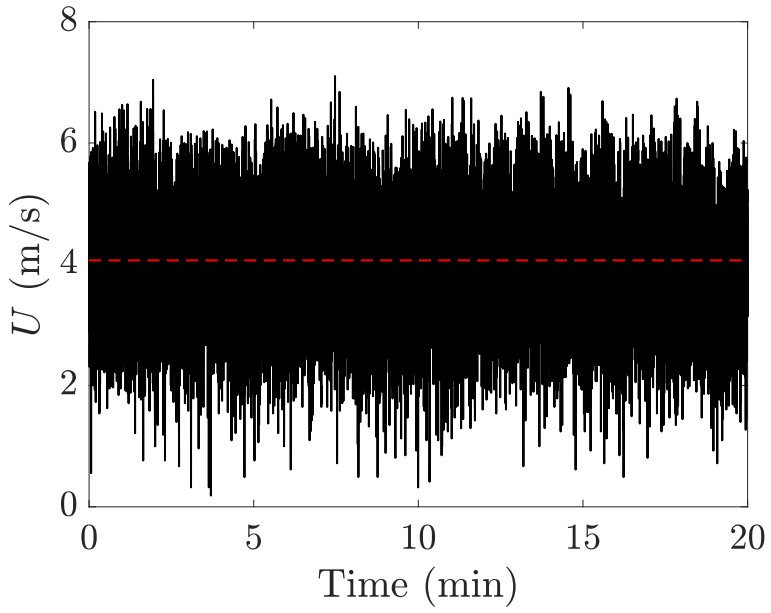

Figure 4.5: Long time series obtained at a downstream location of $x/D = 6$ downstream of row 11 at top tip height at a frequency of 100 Hz

The mean of the 20 minute sample of the velocity time series is the center red dashed line. Blue dot dashed lines indicate $\pm 1\%$ and $\pm 2\%$ deviation from the 20 minute sample of mean velocity. The 20 minutes time series was broken up into smaller data subsets by time, and the subsets' mean velocities are displayed in this figure respective of their new time series length by the symbol "○". Considering this representative example, the long 20 minute time series contains the value closest to the true mean. At a sample length of 5 minutes, the mean velocity spans $\pm 1.6\%$ of that long mean. As an example of an individual segmented one minute sample from the long time series, Figure 4.7, plots the velocity time series from minute 8 to 9. The mean of the long time series in Figure 4.5 is 4.064 m/s and the mean for the short time series in Figure 4.7 is 3.897 m/s. This is a deviation from the long mean of $\approx 4\%$. As the sampling time is artificially decreased and the long time series is broken up into smaller data sets, the variance from this true mean increases as expected. This variation from the mean of the long time series shows that an expanded uncertainty

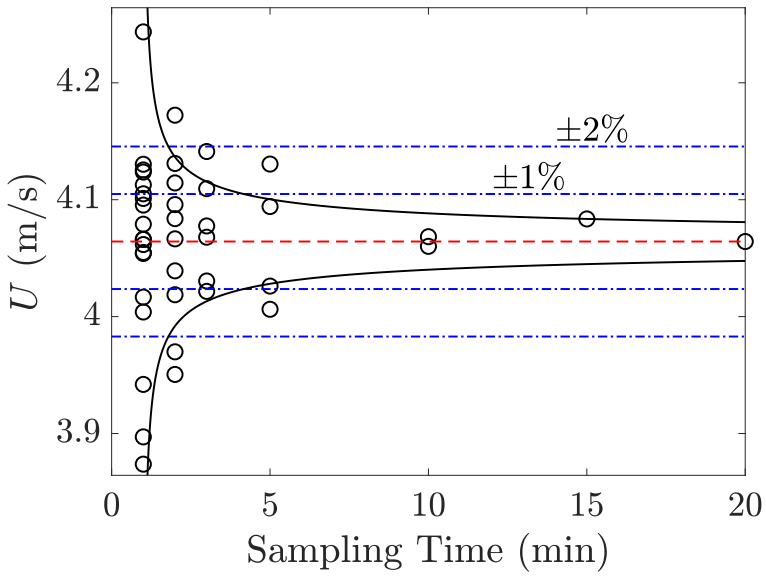

Figure 4.6: Ad hoc length of time series sampling study done at x/D =6 behind row 11 top tip height. Solid lines indicate the standard uncertainty for the mean calculated by Equation 4.3

analysis makes reasonable sense for this case.

Understanding the in situ uncertainty will help minimize data collection time, which includes traversing time, over a single profile, which due to the open to atmosphere configuration of the tunnel, is needed to mitigate potential weather influences in the inlet flow (eg. a passing cloud that changes inlet temperature). In general however, the random uncertainty will change based on the flow case and number of independent samples.

4.2 Standard Uncertainty

The next calculations follows Coleman and Steele (2009) [36]. A similar methodology can be found in the Assessment of Experimental Uncertainty with Application to Wind Tunnel Testing from the American Institute of Aeronautics and Astronautics (1999) [2]. We define the first moment of a random variable x as the mean of that variable.

$$X = \overline{x} \equiv \lim_{N \to \infty} \frac{1}{N} \sum_{i=1}^{N} x_i \tag{4.1}$$

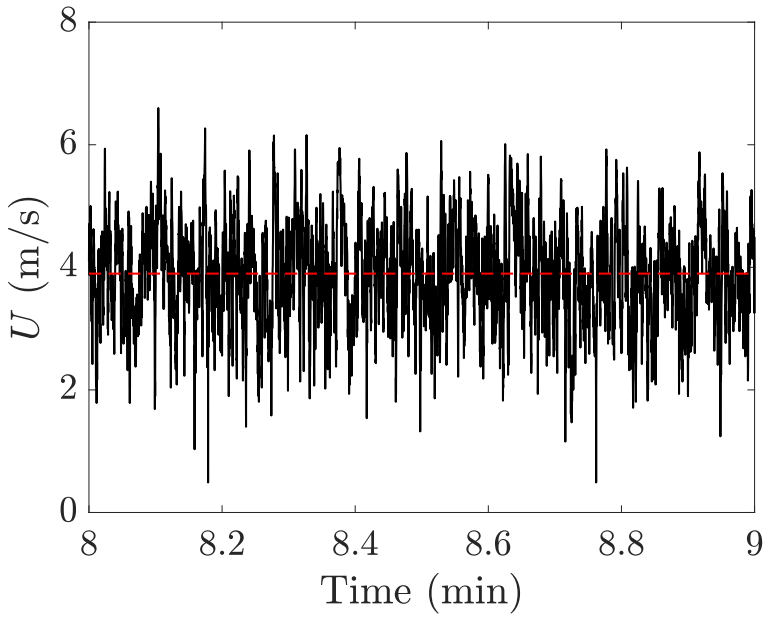

Figure 4.7: One minute segment of the long time series obtained at a downstream location of $x/D = 6$ downstream of row 11 at top tip height at a frequency of 100 Hz

The standard deviation of a single sample, s_x, is also called the root mean square (rms) of the random variable x and is sometimes denoted as the symbol σ_x when the random variable is known to have a Gaussian distribution with number of independent samples N. The standard deviation of a single sample can be assumed to vary by the turbulence in the flow being measured and is represented by

$$s_x = \lim_{N\to\infty} \left[\frac{1}{N-1} \sum_{i=1}^{N} (x_i - \overline{x})^2 \right]^{1/2} \tag{4.2}$$

In the case of measurements performed in turbulent flows, the flow velocity is the random variable x which contains mean and fluctuating components per notation $v = V + v'$, where v' is the fluctuating component of the flow (with mean about zero) and V is the mean component of the flow. The rms is related to the variance of the random variable through $\sigma_x^2 = var(x)$. The variance can be thought of as the second moment of the random variable minus the square of the first moment, meaning, $var(x) = \overline{x^2} - X^2$. Having removed the mean, the variance is the second central moment of the random variable x and describes the extent of difference from the mean in a

single variable. $s_{\overline{x}}$ is the standard deviation of the mean, where the first moment, $\overline{x}$, in a turbulent flow is the mean velocity V.

One can seemingly easily determine the expected error for the first moment assuming a Gaussian distribution of a random variable, by

$$s_{\overline{x}} = \frac{s_x}{\sqrt{N}} \tag{4.3}$$

where N is the number of independent samples. Samples must be statistically independent from one another to fully capture the factors that influence the random behavior of the variable. We will call Equation 4.3 the standard uncertainty calculation. The equation can be rearranged to find a necessary number of independent samples for a predetermined percent error on the mean, $N = (\frac{s_x}{s_{\overline{x}}})^2$. For the purpose of this uncertainty analysis, turbulent flows are often assumed to be Gaussian, which means that the standard deviation for a velocity measurement becomes the turbulence intensity. If, for example, the local turbulence is $s_x = u'/U = 25\%$ (where U is mean velocity and u' is turbulent fluctuations), 625 independent samples would be required to achieve a desired uncertainty on the mean velocity of $s_{\overline{x}} = 1\%$, see Equation 4.3. The variability of the mean quantity varies as the inverse square root of the number of independent realizations, but linearly on the fluctuations of the random variable.

To determine how long one should sample, one must find N, but also ensure that these N samples are independent. Typically, the integral of the one sided autocorrelation of a time series represents the integral time scale. This is a eddy size at which the highest energy contributions to the flow are found. The integral time scale represents a time lag where the flow is decorrelated with itself. Conservatively, the time separations of the first zero crossing of the autocorrelation is used here, the point at which the time series has "forgotten" any past influences on the flow. Anything before this crossing will have some nonzero correlation value implying flow memory. Increasing temporal resolution to sample faster than the time to achieve independent, or uncorrelated, samples does not improve the accuracy of the mean of measurements. Furthermore, using the independent sampling time method to calculate the standard uncertainty will not necessarily

achieve the required certainty for the measurement as will be discussed in section 4.3. Combining the integral time scale with the number of samples required, N, will dictate a total sampling time per measurement point. Figure 4.8 shows the autocorrelation, $R_g(k)$, of the time series taken at

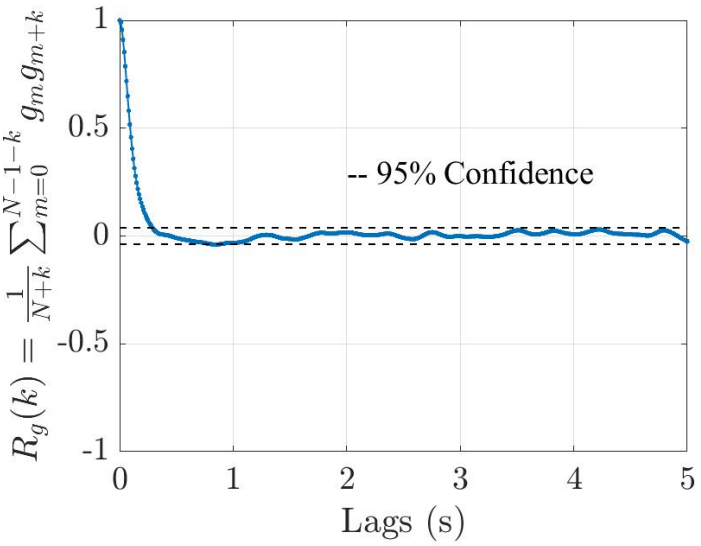

Figure 4.8: Autocorrelation of pitot tube data at top tip height at $x/D = 6$ downstream of Row 11

x/D = 6 downstream of row 11 at turbine top tip height. The integral time scale, or independent sample time, is approximately $T_{independent} = 0.5$ s. For an uncertainty of $s_{\overline{x}}$ =1%, or $N = 625$ independent samples, a sampling time of 312.5 s, or 5 minutes and 12.5 seconds, would be needed. However, this standard uncertainty calculation neglects the effects of temperature variation and the coupling of the systematic uncertainties of each instrument used, and will thus lead to an underestimate of actual uncertainty discussed in Section 4.3.

4.2.1 Representative Baseline Calculations

For the purpose of baseline calculations, we will assume we are taking measurements in a region of the flow with relatively high turbulence (assumed to be 25%) with an average flow speed at turbine top tip height of 4.75 m/s. For ease of calculation this velocity corresponds to a differential pressure readout of 0.1 Torr calculated via Bernoulli's equation using a pitot tube. This calculation is performed at 20°C and 101 kPa barometric pressure. These approximations establish a baseline

and are representative of the established experimental setup. For instance, these values for velocity and turbulence can be nominally located just above top tip height in the representative profile, Fig 4.4.

In these baseline calculations, it is still chosen that less than 1% uncertainty is desired and a sample time must be determined that allows this. Based on the first zero crossing of the autocorrelation $R_g(k)$ of the time series taken at $x/D = 6$ at row 11 top tip height seen in Figure 4.8, independent sample time would be $\tau_{independent} \approx 0.5$ s. Using equation 4.3, each time series is calculated to contain $N = 625$ independent samples. Since a 1% uncertainty on the mean seemed like a reasonable goal, the required sampling time calculated from the standard uncertainty was rounded up to 6 minutes sampling time per point, or 720 independent samples. This translates to about three hours per profile, including traversing time, which allows the experiments to avoid large diurnal temperature variations, but still incur significant temperature variations, see Figure 4.1. 720 independent samples using the standard uncertainty calculation is 0.93% uncertainty on the mean velocity.

4.3 Expanded Uncertainty

Required sampling time per point was initially determined based on the standard uncertainty analysis, and an expanded uncertainty analysis was then performed on the actual experimental data. The following equation contains the true value of a variable within some level of confidence

$$U_{\%} = t_{\%} u_c \tag{4.4}$$

where u_c is the uncertainty of a variable and $U_{\%}$ is the total combined uncertainty [71]. The student t distribution value $t_{\%}$ depends on the number of degrees of freedom (DoF) associated with systematic uncertainty b_k. $t\%$ defines a confidence interval that contains the true value of the variable mean with the chosen percent level of confidence. Here, 95% confidence is chosen, which is to include all values within two standard deviations from the mean. This definition implies that the lower and upper tails of the probability function contain 2.5% of the error distribution each.

We must first calculate the DoF value to determine what student t value to use to find the total uncertainty. The calculation for number of DoF is

$$v_{bk} = \frac{1}{2}\left(\frac{\Delta b_k}{b_k}\right)^{-2} \tag{4.5}$$

where $\frac{\Delta b_k}{b_k}$ is the relative uncertainty, usually given in a percentage of the measured value, and typically found on an instrument specification sheet as a factory guideline. As the certainty of a measurement increases (and thusly the *un*certainty decreases), DoF increases. Using equation 4.5, any relative uncertainty value smaller than $\frac{\Delta b_k}{b_k} \approx \pm 6.45\%$ results in greater than 120 DoF. On most student t charts, it is acceptable to use $\geq$120 DoF$= \infty$ DoF and find the student t value in accordance. As $\pm 6.45\%$ is greater than the requirement of $s_{\overline{x}} < 1\%$ error, the constant value from a student chart of $t_{\%} = 1.96$ is used for 95% confidence [18]. This method assumes a Gaussian distribution of the independent samples that make up the mean velocity as confirmed by measurement in situ at top tip height at a streamwise location of $x/D = 6$ downstream of row 11 in Figure 4.9. In the figure, p_y is the binned distribution and the red overlaid line is the Gaussian. The exists a slight amount of negative skewness in the tail, but the overall shape represents a Gaussian distribution.

4.3.1 Taylor Series Method

Velocity is calculated from the readout of a pressure transducer connected to a pitot tube via Bernoulli's equation

$$V = \sqrt{\frac{2P}{\rho}} \tag{4.6}$$

Where P is the differential pressure from the transducer and ρ is air density, which can be found through the ideal gas law, $\rho = P_{atm}/RT$. R is the specific ideal gas constant for air ($R = 0.2871$ kJ/kgK), thermocouple temperature is T and atmospheric pressure is P_{atm}. Combining the ideal gas law with Bernoulli's equation we have

$$V = \sqrt{\frac{2PRT}{P_{atm}}} = \sqrt{2R}P^{1/2}T^{1/2}P_{atm}^{-1/2} \tag{4.7}$$

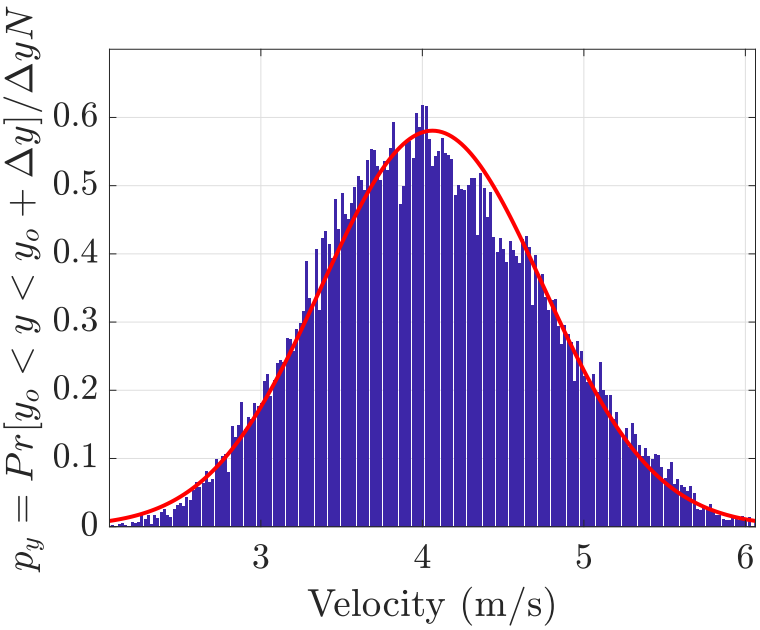

Figure 4.9: Velocity histogram at $x/D = 6$ behind turbine row 11 top tip height. The data is binned in 0.02 m/s bin sizes with 2 m/s range about mean

For each variable in Equation 4.7 the systematic uncertainty and random uncertainty are used to obtain the combined standard uncertainty of each mean result. This equation to calculate the quantity of interest, velocity, will be the base equation input into the Taylor Series.

$$\frac{\partial V}{\partial P} = \sqrt{2R}\frac{1}{2}P^{-1/2}T^{1/2}P_{atm}^{-1/2} = \frac{1}{2}P^{-1/2}\sqrt{\frac{2RT}{P_{atm}}} \tag{4.8}$$

Keeping only the first terms in a Taylor series expansion, the combined standard uncertainty for the Taylor series method (TSM) for an arbitrary variable r is given by

$$u_r^2 = \underbrace{\Sigma_{i=1}^{J}(\frac{\partial r}{\partial X_i})^2 b_{X_i}^2}_{b_r^2} + \underbrace{\Sigma_{i=1}^{J}(\frac{\partial r}{\partial X_i})^2 s_{X_i}^2}_{s_r^2} + b_{correlated}^2 \tag{4.9}$$

where b_r^2 is the systematic uncertainty, s_r^2 is the random uncertainty, both broken up into J number of additive sources. The systematic error correlation effects are known as $b_{correlated}$ [13]. The systematic uncertainty can arise from an inherent inaccuracy with an instrument in the data acquisition

suite, while the random uncertainty is inherent to the measurement itself. The random uncertainty is best calculated in situ as in equation 4.3. The systematic error correlation effects term presumes the instantaneous quantities are correlated by identical calibrations, system biases, and algorithm processing, sometimes out of the control of the operator [116].

Using the general uncertainty analysis expression in equation 4.9, and considering only the measured quantities, the uncertainty is determined by

$$U_V^2 = (\frac{\partial V}{\partial P})^2 U_P^2 + (\frac{\partial V}{\partial T})^2 U_T^2 + (\frac{\partial V}{\partial P_{atm}})^2 U_{P_{atm}}^2 \tag{4.10}$$

Taking derivatives of velocity with respect to the variables for differential pressure, temperature, and atmospheric pressure, we have

$$U_V^2 = (\frac{1}{2}P^{-1/2}\sqrt{\frac{2RT}{P_{atm}}})^2 U_P^2 + (\frac{1}{2}T^{-1/2}\sqrt{\frac{2RP}{P_{atm}}})^2 U_T^2 + (-\frac{1}{2}P_{atm}^{-3/2}\sqrt{2RPT})^2 U_{P_{atm}}^2 \tag{4.11}$$

Dividing by V^2 the combined standard uncertainty for velocity is

$$(\frac{U_V}{V})^2 = (\frac{1}{2})^2(\frac{U_P}{P})^2 + (\frac{1}{2})^2(\frac{U_T}{T})^2 + (\frac{1}{2})^2(\frac{U_{P_{atm}}}{P_{atm}})^2 + \Sigma b_{correlated}^2 \tag{4.12}$$

The systematic and random uncertainty for each variable is now calculated.

4.3.1.1 Pitot Tube Pressure

The MKS Baratron 698A Pressure Transducer specification sheet lists a systematic uncertainty $\pm 0.15\%$ of the readout, $b_{transducer} = 0.00015 \times P_{measured}$ Torr. The random uncertainty will change based on the flow case and quantity of independent samples. The random uncertainty for the pressure transducer calculated in situ for this example is $s_{transducer} = 0.00094$ Torr. We recall the equation for total uncertainty and apply it to the transducer.

$$u_P^2 = s_{transducer}^2 + b_{transducer}^2 \tag{4.13}$$

4.3.1.2 Temperature

As amply discussed, there is a need to reconcile the variable ambient inlet conditions that an open to atmosphere facility may encounter. The temperature measurement is obtained by a k type thermocouple amplified by an AD595C thermocouple amplifier. The amplifier has a stability uncertainty of $\pm 0.025^oC/^oC$ deviation away from 25 ^oC, $b_{stability} = 0.025$ and a gain error of $\pm 0.75\%$, $b_{gain} = 0.0075 \times T_{measured}$ K. Random uncertainty for the thermocouple is obtained by calculating the standard deviation of a 360 s time series and recalling the independent sample at $T_{independent} = 0.5$ s, $s_{thermocouple} = 0.024$ K. The stability of the device is a linear degree per degree, so the units can be either Celsius or Kelvin. However, the gain error is a percent of the output, so this must be measured in Kelvin, as absolute units are used in the ideal gas law to calculate density and thusly velocity. Now the general uncertainty Equation 4.9 applied to the thermocouple is

$$u_T^2 = s_{thermocouple}^2 + b_{gain}^2 + b_{stability}^2 \tag{4.14}$$

If the FPF was able to be temperature controlled to what a standard indoor facility might experience, say 0.1°C for instance, a decrease in uncertainty could be expected. Note that this decrease would have to come from the ability to obtain longer data sets per collection scheme. Without atmospheric changes affecting the inlet conditions, a longer quasistatic environment would allow for longer time series.

4.3.1.3 Atmospheric Pressure

Atmospheric pressure is not measured at every 6 minute average, but rather obtained from a local weather tower that broadcasts results hourly. An uncertainty arrives from the fact that the barometric pressure could change over the course of the measurement. Over a six hour window, as in an afternoon of data taking, the atmospheric pressure may shift by 1.0 kPa (10 mbar), where the approximate average is 101 kPa ($s_{atmosphere} = 0.5$ kPa). Systematic uncertainty is not considered for the atmospheric pressure measurement as data acquisition information is not known about the

weather tower system. A larger barometric shift in this time frame would indicate a storm or other event where the FPF would not be operating due to the open to atmosphere nature.

$$u^2_{P_{atm}} = s^2_{atmosphere} \tag{4.15}$$

4.3.1.4 Systematic and Random Uncertainty Summary

Instrument	b_k	s_k	U	$U_{\%}$
Pitot Tube Pressure	0.15%	0.94 mTorr	1.9 mTorr	1.87%
Thermocouple	0.025°C/°C and 0.75%	0.024 K	4.3 K	1.47%
Atmospheric Pressure	-	0.5 kPa	101 kPa	0.98%

Table 4.1: Expanded uncertainties for instruments at 95% confidence using expected values

Using the expected values of $P = 0.1$ Torr, $T = 25\ ^oC$ (298.15 K) and $P_{atm} = 101$ kPa with a 95% level of confidence and infinite degrees of freedom for the student t distribution, expanded uncertainties are obtained and presented in Table 4.1. The values of b_k are from specification sheets, and the values s_k are measured and calculated in situ. The confidence level $U_{\%}$ is indicative of how much this particular quantity influences the final expanded uncertainty of the velocity. In Table 4.1, it can be seen that the pressure transducer and the thermocouple measurements have a much larger influence on the mean velocity uncertainty than the atmospheric pressure variation.

4.3.2 Systematic error correlation effects

Included here are systematic error correlation effects, $b_{correlated}$, which arise from sources of uncertainty not included in the calculation of our desired quantity. The independent variables of the fan control drive and digitization of analogue data are not included in the calculation of the velocity, but they have an obvious effect on the outcome of the experiment.

4.3.2.1 Digitization

The spec sheet of the 16-bit DT9836 DAQ lists a system accuracy of full scale as 0.015%, $b_{DAQ} = 0.0015$, where full scale of the DAQ is 10 Volts. With the confidence interval included,

$U_{DAQ} = 0.0029$. Both the pressure transducer and the thermocouple analog signals have to be read in and digitized. The pressure transducer, assuming a nominal $P_{readout} = 0.1$ Torr and the middle range option on the signal conditioner selected (Volts = 0.1X Torr), would correspond to $DC_{transducer} = 1$ Volt. The thermocouple temperature is calculated as follows

$$T = (DC_{TC} - DC_{offset}) \times 100 \ [C] \tag{4.16}$$

where DC_{TC} is the voltage output by the thermocouple amplifier and DC_{offset} is the calibration of the thermocouple. This would mean a temperature of 20^oC using the offset value of $DC_{offset} = -0.06$ corresponds to a voltage of $DC_{TC} = 0.14$ Volts.

4.3.2.2 FPF Variable Frequency Drive

The fans in the FPF are two 2.6 m diameter vane-axial fans, powered by two 300 kW AC motors. They are controlled by variable frequency drives and operated in a coupled leader-follower configuration controlled by PID that is accurate to ± 0.5 RPM $b_{rpm} = 0.5$ and the fans will operate at 600 RPM.

4.3.2.3 Error Correlation Effects Summary

Instrument	$b_{correlated}$	U	$U_{\%}$
Pressure Digitization	0.0015 V	0.0029 V	0.29%
TC Digitization	0.0015 V	0.0029 V	2.10%
FPF VFD	0.5 RPM	0.98 RPM	0.16%

Table 4.2: Systematic uncertainties at 95% confidence using expected values

A list of the expanded uncertainties, including systematic error correlation, is shown in Table 4.2. It can be noted that by percentage, the digitization of the thermocouple is the largest contributor to uncertainty. Thermocouples function on the dissimilarity between two metals that form an electrical junction dependent on temperature. This junction phenomenon is known as the thermoelectric effect and the flow of electrons that produces a readable voltage is very small and needs

to be amplified. Amplifying any analog signal can be problematic, especially when trying to decipher signal from noise. After this small signal is amplified, it must be digitized, but is still a small fraction of the full scale DAQ input, and therefore ends with increased uncertainty.

4.3.3 Final Combined Uncertainty

Revisiting the combined standard uncertainty, equation 4.12, and using the above expected values, to within 95% confidence a final nominal combined uncertainty of the velocity is

$$\frac{U_V}{V} = 2.5\% \tag{4.17}$$

The final uncertainty found in Equation 4.17 is the total expanded uncertainty including systematic, random and correlated uncertainties from instruments and devices for a sampling length of 6 minutes. This can be contrasted with the standard uncertainty from Equation 4.3, which for 720 independent samples is 0.93%. Even for significantly longer sampling times, i.e., on the order of an hour per point, the total combined uncertainty will remain higher than this value predicted from the standard uncertainty. The largest contribution to uncertainty in the mean velocity comes from the thermocouple digitization. The driving factor of this correlated uncertainty is that the voltage output of the thermocouple amplifier is small, even though the DAQ is highly accurate. The pressure transducer readout is also one of the larger contributors to the overall uncertainty.

4.4 Monte Carlo Simulation

A Monte Carlo simulation was performed to capture the uncertainty of the measurement of mean velocity and compare with the TSM. The Monte Carlo Method (MCM) is a stochastic simulation procedure that imitates sampling the quantity of interest directly, including all sources of systematic, random and correlated uncertainties [36]. Assuming that the variable uncertainty involved in the calculation of the measurement are normally distributed and additive, the MCM may be considered a form of experimental statistics, a brute force trial calculation [47]. It has been shown that the TSM is unable to account for skewness of the systematic uncertainty if a variable is does

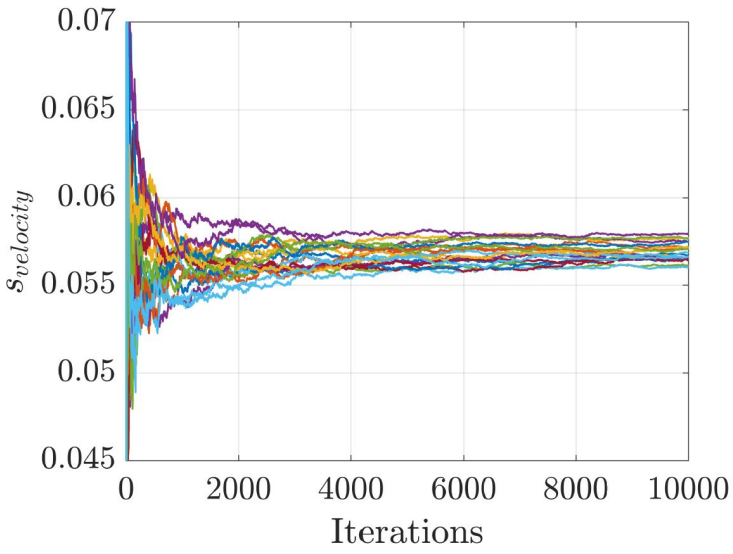

Figure 4.10: 10,000 Monte Carlo iterations for 20 trials of the standard deviation of the mean velocity using representative true values

not have a symmetric distribution [116]. However, only normal distributions of uncertainty are accounted for here, and the slight negative skewness of Figure 4.9 is ignored. It is shown here that the MCM and TSM calculate very similar combined uncertainties.

To calculate each MCM iteration, true representative values were obtained from Section 4.2.1 and fluctuation values were obtained from a Gaussian random number generator with prescribed standard deviations from Table 4.1. Including in situ instrument variations forces the Monte Carlo to reproduce reliable estimates on calculated outcomes. The MCM included systematic and random uncertainties, both with defined Gaussian statistics. The error correlation effects were also included in the standard deviation of each variable via percentage normalization of the effected terms in the velocity calculation eg. $b_{correlated} = T \times U_{Digitization}$. The convergence of the standard deviation of the mean velocity, $s_{velocity}$, is shown for twenty Monte Carlo simulations for 10,000 iterations in each simulation in Figure 4.10. The standard deviation of each simulation was taken at the 10,000th iteration and averaged over the twenty simulations to produce the total uncertainty on the mean velocity at 95% confidence of $U_{VMC} = 2.4\%$. This MCM uncertainty confirms the validity of the TSM mean velocity uncertainty calculation.

4.5 Comparison of instruments

The original goal of this experimental setup was to elucidate what energy transport mechanisms dominate the continued energy production of wind turbines very far downstream in a wind turbine array boundary layer. In large farms a state is reached where the forcing of the atmospheric boundary layer balances the turbines' momentum extraction. At this stage, called the fully developed wind turbine array boundary layer, the mean velocity and turbulence quantities remain statistically similar in a tightly defined region from one row to the next. The tightly defined, so called equilibrium region, is defined as turbine top tip height to one turbine radius above top tip height. If the turbulent quantities in this region converge, the array is certainly fully developed. To investigate if the equilibrium region converges with turbulent statistics in addition to the mean, multiple components of velocity and a high temporal resolution are required to resolve the turbulent fluctuations. A two component x-wire hot wire anemometer was chosen for this task. This section will describe the shortcomings of the multi-component hot wire and why data of this nature is not present in this thesis.

4.5.1 Hotwire uncertainties

For the wind turbine array experimentalist, one term of particular interest is the statistical convergence of the Reynolds shear stress $\overline{u'v'}$, where the prime ($'$) indicates only the fluctuating component of the velocity. This term is responsible for the transport of momentum through the shear layer above the turbines down into the array itself. It is assumed that in the equilibrium region, these sweeps eventually reach a steady state when the array is fully developed. In this experiment, a two component x-wire hotwire was used to capture streamwise (typically denoted as u) and wall normal (typically denoted as v) velocities. The wires are oriented at 90° from each other with each wire also being 45° from the streamwise flow direction to capture both directions of flow. The wires are separated by 1 mm, and oriented with the sting pointing into the flow. Calibration of an x-wire requires a dedicated calibration jet unit which is connected to a pressure

transducer. Therefore this flow measurement technique includes the uncertainty of the previous pitot tube velocity calculation, plus additional error sources.

Hotwire anemometers are chosen to be used in experiments for their high spatial and temporal resolutions. In constant temperature anemometry (CTA), a very thin wire is heated via voltage input to above ambient flow temperature with circuitry involving a Wheatstone bridge. A defined overheat ratio a is applied to the wire involving the wire material's (in this case, tungsten) temperature coefficient of resistance α, the wire temperature T_w and a reference temperature T_o.

$$a = \alpha(T_w - T_o) \tag{4.18}$$

The convective cooling of the flow over the probe reduces the temperature of the wire. To maintain the specified overheat ratio a voltage input is required, which is then correlated to flow velocity. Because the wires are hotter than the environment, there is the possibility of a natural convection effect from the hotwires. A characteristic convection velocity may be determined by equating the Reynolds number ($R \equiv U_c d/\nu$) and square root of the Grashof number ($Gr \equiv g\beta d^3 \Delta t/\nu^3$). This velocity is generally very small, in particular owing to the minuscule diameter of the hotwire. A nominal convection velocity of $U_{con} = 0.005\ m/s$ was found in [80] which would be 0.1 % of the mean velocity using the representative values in Section 4.2.1. Even so, due to the additional complexities of the hardware involved, necessarily the hotwire will have a greater uncertainty than a pitot tube or other, more simple, measurement devices.

Additional error sources relating to the calibration procedure and the electronics of the instrumentation are listed in Table 4.3. Values calculated in Table 4.3 use the expected value of -4 V analogue out of the anemometer. This is the signal that will be input into the DAQ. The other values are found in instrument manuals and specification sheets when available. Calibration directionality comes from a description of the in house calibration device used. The streamwise flow is estimated to be directionally accurate to within 1%, while the vertical velocity component is less trustworthy at 6% uncertainty [42, 52]. Additionally, the probe itself can only be directionally accurate to within 1% in either the streamwise or vertical flow measurement positioning. More de-

Source	$b_{correlated}$ (mV)
Signal conditioner	1.42
Power supply	0.10
Gain error	20.00
Probe noise	0.14
Drift	7.20
Calibration lookup table	4.00
Calibration directionality	40.00

Table 4.3: Additional uncertainties for a hotwire anemometer. Hotwire expected value of -4 Volts into the DAQ

tails about the 2D calibration jet can be found in [42]. Including the random uncertainties, $s_{hotwire}$, measured in situ for a 10 minute sampling time, the mean velocity measurement from the x-wire for a confidence of 95% is almost $U_{HW\%} = 4\%$. It can be noted that decreasing the confidence interval (eg. 90% or 75%) would modify the uncertainty band.

The Reynolds stress will now be addressed, which we recall contains fluctuating components of velocity. If it is assumed that the error is unbiased and normally distributed, one can deduce that the percent errors in the velocity rms values are nominally the same as for the mean values. In a boundary layer study with a multi-wire hotwire it was shown that the Reynolds stress converged at least as fast as either of the velocity quantities measured to compute it [80]. The uncertainty in the Reynolds shear stress, $s_{\overline{uv}}$, is estimated by adding the component fluctuating velocity uncertainties of u' and v' in quadrature. The uncertainty calculated here with a 10 minute sampling time using the representative values above is $s_{\overline{uv}} = \sqrt{u'^2 + v'^2} = 12.8\%$ at a 95% confidence interval. This uncertainty is significantly greater than that of the mean velocity. It should be noted that some researchers believe the statistical convergence of the turbulence quantities is also necessary to validate the fully developed wind turbine array boundary layer condition [31]. The challenge for the overall study lies in trying to prove an asymptotically converging condition in which the uncertainty is greater than the differences between the downstream measurement locations.

As discussed in Section 4.2 using Equation 4.3, increasing the length of a time series will decrease the standard deviation of the mean by $\sqrt{N}$. A plot of uncertainty of an x-wire hotwire

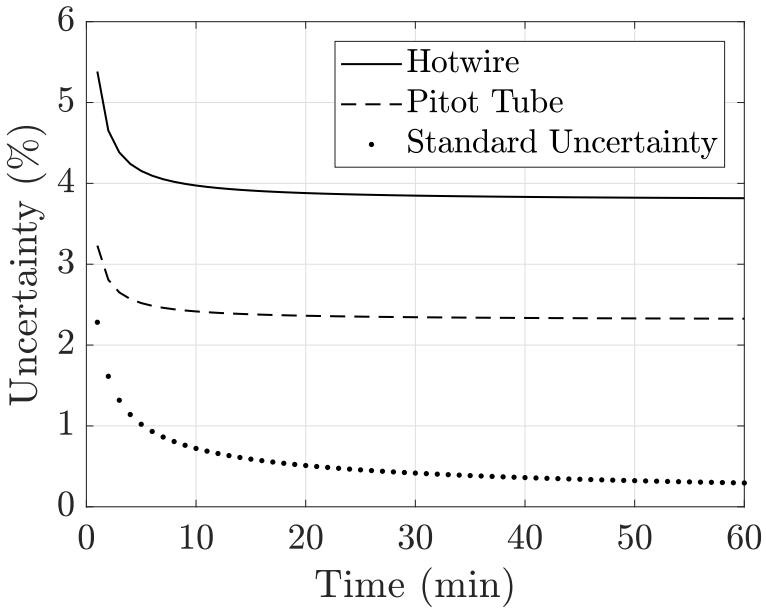

Figure 4.11: Representative uncertainty versus length of sample time for the mean velocity of an x-wire and pitot tube using the TSM at top tip height, row 11, $x/D = 6$. Compared with the standard uncertainty calculation from Equation 4.3.

mean velocity versus time is displayed in Figure 4.11. Uncertainty decreases very rapidly initially and seems to reach a steady state after the 10 or 20 minute mark. It is obvious that even with incredibly long sampling times, reaching the goal of the predicted standard uncertainty found in Equation 4.3 with the instruments available is unrealistic. Recall that each time series produces only one mean velocity value in a campaign of data acquisition and the length of the overall data set must be considered, as well as the uncertainty the value contains. At a certain single time series length, we are precluded from accomplishing an entire data set due to changes in atmospheric conditions.

4.5.2 Hot Wire versus Pitot Tube

X-wire hotwire timeseries was acquired for 10 minutes per point in the equilibrium region at a select number of rows at a downstream position of $x/D = 6$ per row. Time series at the exact same location within the experimental setup in a different measurement campaign was also acquired with the pitot tube as discussed previously. In Figure 4.12 time series is acquired at the center

column turbine at a position of $x/D = 6$ downstream of rows 13-16 from a vertical position of top tip height, to 1D above hub height, where hub height is defined as $z/D = 0$. Pitot tube velocity data points were averaged over 6 minutes time series while x-wire time series were averaged over 10 minutes. It is shown empirically in Figure 4.12, the hotwire data has more uncertainty than the pitot tube data. This region, as confirmed for the mean in Chapter 5, is within the fully developed

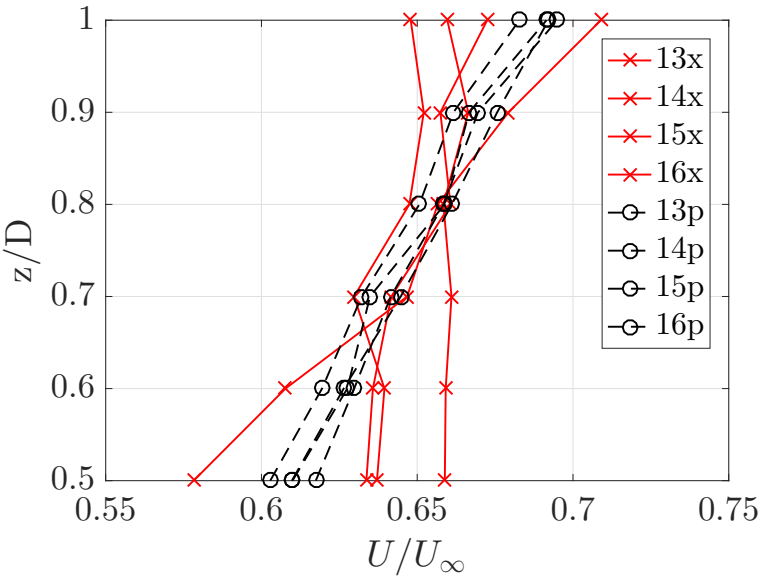

Figure 4.12: Equilibrium region data from rows 13-16 taken with both an x-wire hotwire for 10 minutes per point (x) and a pitot tube for 6 minutes per point (o).

region of the wind turbine array boundary layer. That is to say, the profiles from the pitot tube data here converge to similarity within the experimental uncertainty. Additional scatter is evident from the hotwire measurements compared with the pitot tube data. To investigate the asymptotic convergence of higher order turbulence terms in this experimental setup, a higher accuracy method is required.

4.6 Summary

The typical standard uncertainty analysis for the first order moment of a turbulent flow, velocity, only considers the local turbulence and number of independent samples. An expanded uncertainty analysis has been performed, accounting for the bias of each instrument in the measurement suite

to calculate mean velocity. Efforts were focused on the balance of data accuracy with reasonable total measurement time, considering the open to atmosphere nature of the facility. The temperature acquisition and digitization is the main driver of the uncertainty. The primary mitigating factor keeping uncertainty low is increased data acquisition time. Point wise data collection time had to be balanced with the unpredictability of inlet weather conditions to determine an appropriate overall profile time length. Uncertainty of the specific measurement device being used must be considered when trying to gain information from a turbulent flow of interest. Instruments with additional complexities sometimes preclude obtaining the most relevant trends about specific experimental flow setups. The final expanded uncertainty for the mean velocity was calculated using representative values as a nominal 2.5% uncertainty at 95% confidence. The results of the Taylor Series Method expanded uncertainty analysis were confirmed by a Monte Carlo simulation.

CHAPTER 5

MEAN VELOCITY

The following section discusses the results from the velocity measurements in the wind turbine array boundary layer. Experimental data are reported for a wind turbine array boundary layer (WTABL) in a model wind farm. An array of 95 model wind turbines consisting of 5 streamwise columns by 19 spanwise rows of 0.25 m diameter models was studied in the University of New Hampshire Flow Physics Facility (FPF). The wind turbine array was constructed of porous disks, which were drag (thrust) matched to offshore wind turbines at typical operating conditions. The turbine spacing was 8 diameters in the streamwise and 4 diameters in the spanwise directions. Spires were used to thicken the boundary layer and achieve a boundary layer thickness on the order of 1 m at the first row of the wind turbine array, which is located 33 m downstream from the test section inlet, thus placing the turbines in the bottom 1/3 of the boundary layer. The inlet profile of the wind turbine array was measured with a single wire hotwire. Velocity profiles at a downstream location of $x/D = 6$ in the center column of the first 17 rows of model turbines were measure with a pitot-static tube, following the point spacing shown in Figure 3.9. To within experimental uncertainty, a fully developed WTABL condition is observed in the mean velocity, for defined inlet conditions and spacings, from row 12 on. The wind turbine array acts as a sparse displaced roughness, which creates an internal layer whose origin (in the wall-normal direction) remains fixed in space, while the turbulent boundary layer it was placed in continues to grow. Porous disk turbine models are the experimental equivalent of numerical actuator disks, therefore this publicly available data set is expected to be useful for numerical model validation.

5.1 Inflow conditions - modeling the atmospheric boundary layer

The wind tunnel was modified to achieve a simulated atmospheric boundary layer of sufficient thickness at the first row of the model wind turbine array.

5.1.1 Boundary Layer Thickening

The boundary layer was thickened with the help of eleven 1 m tall Irwin Spires [70], placed 5 m downstream from the wind tunnel turbulence management section. The spires are photographed in Figure 5.1, which are placed at 62 m downstream of the FPF inlet prior to moving them to their experimental location of 5 m downstream of the turbulence management section. Their construction was out of 3/4" plywood with a 0.5 m long base for stability. The spires are broken up into three sections for ease of transportation into the test section. The spires are triangular, with a

Figure 5.1: Irwin Spires placed at 62 m downstream of the inlet in the test section of the FPF

wide base and thin peak. This shape creates wakes that redistribute the momentum approximately into boundary layer shape. The spire design assumes that there is vigorous mixing downstream of the spires, and that any flow structures imposed by their shape have sufficiently decayed by $6h$ downstream, where h is the spire height. Figure 5.2 shows comparisons of the boundary layer velocity profile at the centerline of the FPF at 66 m downstream of the inlet, 33 m downstream of the inlet with the spires installed and at 6 times the height of the spires downstream of the spires. It's obvious from this plot that the mixing has not fully coalesced into a nicely shaped boundary

layer velocity profile as near to the spires as $6h$. However, at 33 m downstream from the inlet, or 28 meters from the spires (as the spires are 1 m in height this is also $28h$), a boundary layer profile as emerged and a comparison with the boundary layers natural growth at 66 m is shown. The boundary layer profile at 33 m downstream is sufficiently thick, as discussed below, to warrant placing a wind farm in this flow.

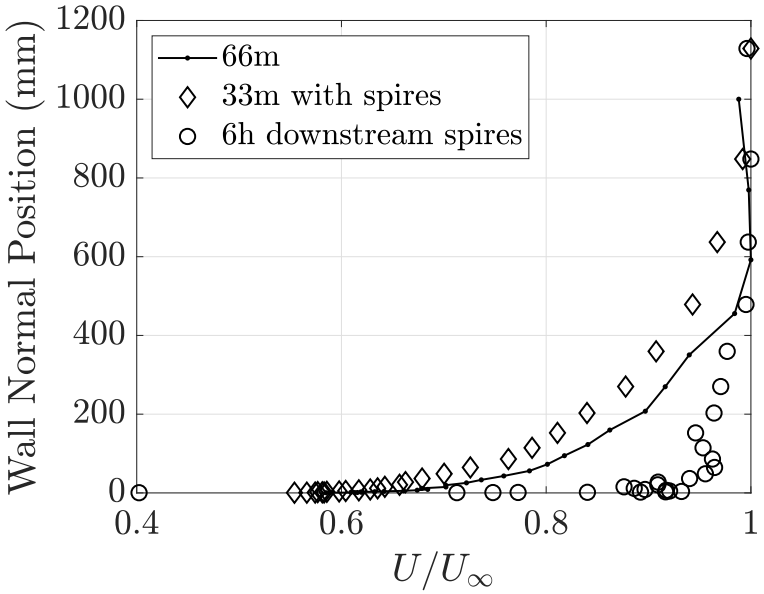

Figure 5.2: Boundary layer velocity profiles at 66 m downstream of the inlet compared with the implementation of the spires at $6h$ and 33 m downstream of the inlet

The technique of placing large roughness and spires to artificially thicken boundary layers to simulate atmospheric boundary layers in wind tunnels is a well known and utilized practice [24, 4, 46, 82]. The boundary layer continues to grow over the development fetch, and the inlet flow of the turbine array is a simulated stable atmospheric boundary layer.

5.1.2 Array Inlet Boundary Layer Comparison with ASCE Standard 49-12

The velocity profile at the wind turbine array inlet is shown in Figure 5.3. The profile was obtained with a single wire hotwire which was traversed vertically at $x = 32.5$ m downstream from the wind tunnel turbulence management section, or $x = 0.5$ m ($x/D = 2$) upstream of the first turbine row. The boundary layer thickness at this location, calculated as $\delta_{99} = y(U = 0.99U_\infty)$

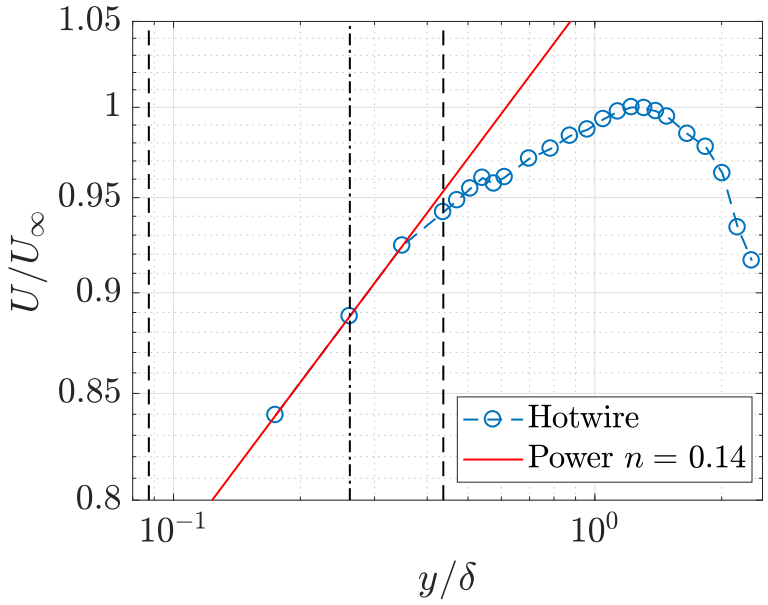

Figure 5.3: Velocity profile two turbine diameters (0.5 m) upstream of the wind turbine array. The vertical dash-dot line is at hub height, dashed lines show extent of turbine rotor.

from the velocity profile, is $\delta = 0.72$ m. An example of the determination of the boundary layer height is plotted in Figure 5.4. The velocity used for U_∞ to calculate δ_{99} is actually U_{max} as seen in the example profile of the velocity downstream of turbine row 5.

To determine how well the atmospheric boundary layer is simulated, we compare the inflow profile to the ASCE Standard 49-12 [9]. For exposure category C, the atmospheric boundary layer "gradient height" is z_g= 274 m full scale [9]. The FPF boundary layer at the inlet of the wind turbine array is 0.72 m high which is $\approx$ 1:380 scale compared to full scale z_g. Recall the turbines that are being using to build this experimental array are 1:500 scale models. The atmospheric sublayer is about 25% of the boundary layer which for a category C boundary layer is 68.5 m full scale. [1] Similarly, for a 1:380 model scale atmospheric boundary layer, the atmospheric sublayer in the FPF would be 0.18 m. That is to say, the turbine hub height (H_{hub}= 0.1875 m) is approximately at 25% of the boundary layer thickness.

[1] Some of the nomenclature and definitions used in the ASCE Standard 49-12 are different from what is commonly used in turbulent boundary layer research.

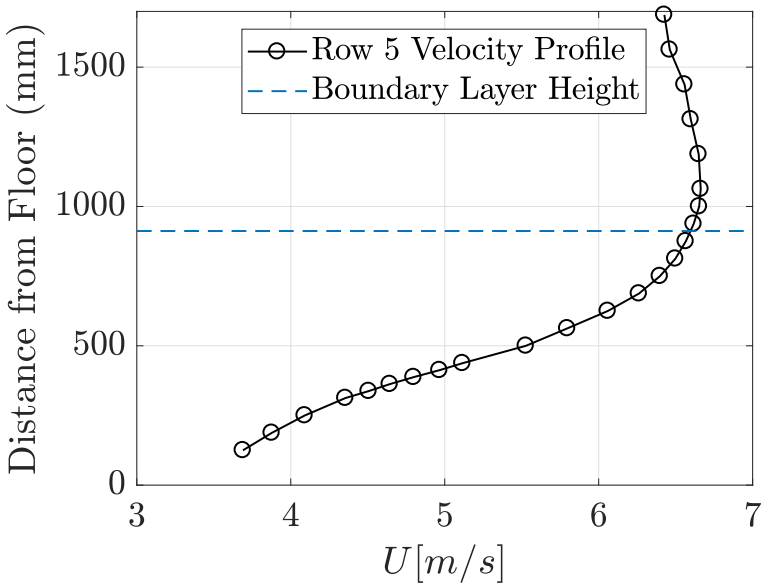

Figure 5.4: Determination of boundary layer height using $U = 0.99U_\infty$ from the velocity profile downstream of turbine row 5.

As the near-wall region was not of interest in this study, a power law was fit to the three points closest to the wall, covering approximately $0.17 \leq y/\delta \leq 0.35$. The power law provides an empirical formulation for the mean velocity profile through the ABL, except for very near the surface. The three points in the fit are all within the extent of the model turbine rotor, and a power law exponent of $n = 0.14$ is obtained. As per ASCE standard 49-12 table C2-1, which comes from ASCE 7-16, this is a category C exposure: "Open flat terrain; grass, few isolated obstacles" [10]. If additional points in the incoming boundary layer are included in the power law fit, it is possible to reduce the power law exponent towards a category D exposure: "Flat, unobstructed areas and water surfaces outside hurricane-prone regions including smooth mud flats, salt flats, and unbroken ice" [10].

The single wire hotwire data was also compared with turbulence profile theories from ASCE in Figure 5.5 where turbulence is defined as the fluctuations over the local velocity u'/U_{local}. It is noted that the turbulence profile at the inlet of the turbine array contains less turbulence overall than ASCE theory, Category C and D exposure. Larger scale motions are needed in the FPF to reach the same turbulence intensity as in the theory.

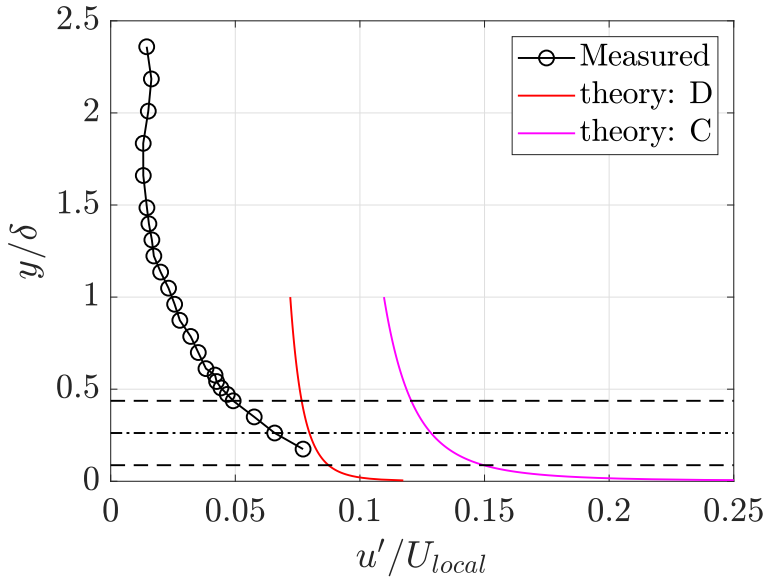

Figure 5.5: Array incoming turbulence profile plotted with the ASCE Categories C and D exposure theory. Horizontal dashed lines indicate bottom tip, hub, and top tip height.

The single wire hotwire data at hub height was used to produce the spectrum in Figure 5.6. The spectrum is plotted with 50 degrees of freedom (DoF) which is defined as the number of independent components that contribute to the estimate. A raw spectral density starts with 2 DoF which increases with increased band width or ensemble averaging. A typical turbulence spectrum is observed. A -5/3 slope is shown for reference, and the spectrum appears reasonably parallel to that over an intermediate frequency (eddy size) range. The theoretical power spectral density derived by von Kármán and used in the ASCE Standard is

$$\frac{fS_u(z,n)}{\sigma_u^2} = \frac{4f^xL_u/U}{[1+70.8(f^xL_u/U)^2)]^{5/6}} \tag{5.1}$$

where $S_u(z,n)$ is the power spectral density of the u velocity component, f is the frequency, and ${}^xL_u$ is the integral scale of the streamwise component of velocity in the streamwise direction [9, 115]. ${}^xL_u$ is the most common measure of the most energetic gust size used in wind engineering practice. Within the atmospheric sublayer (ASL) an estimate of the streamwise integral scale is given by

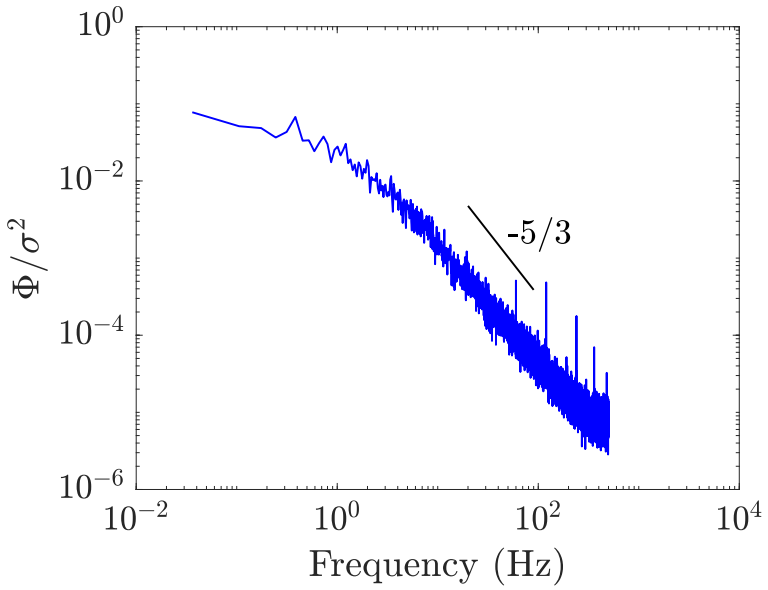

Figure 5.6: Spectra of the inlet of the array at hubheight. 50 DoF

$$^{x}L_u = z/(2\pi f_m) \tag{5.2}$$

where f_m is the reduced frequency at the maximum of $nS_u(n)$. The value used here is $f_m = 0.032$ for an incoming ideal exposure category [9].

A typical power spectrum is usually monotonically decreasing with few frequency peaks. The dominance of the low frequency high energy peaks sometimes obscures less energetic peaks in the mid frequency range. To rectify this, spectra can be pre-multiplied by frequency. The low spectral density, fastest turnover times, are only slightly amplified, due to the low magnitude energy when premultiplied. Weighting the spectra by frequency multiplication helps to identify the most common energy additions to the flow. The theoretical expression for power spectral density in an atmospheric boundary layer, equation 5.1, is compared to the pre-multiplied spectrum measured at hub height in Figure 5.7. The theoretical spectrum represents the measured spectrum, in terms of shape, at the hub height measurement location. The peak of the premultiplied spectrum is slightly lower than that of the model indicating less energy at the larger scales. The decreased variance in this spectrum compared to theory is also why the turbulence is less than predicted as seen in 5.5.

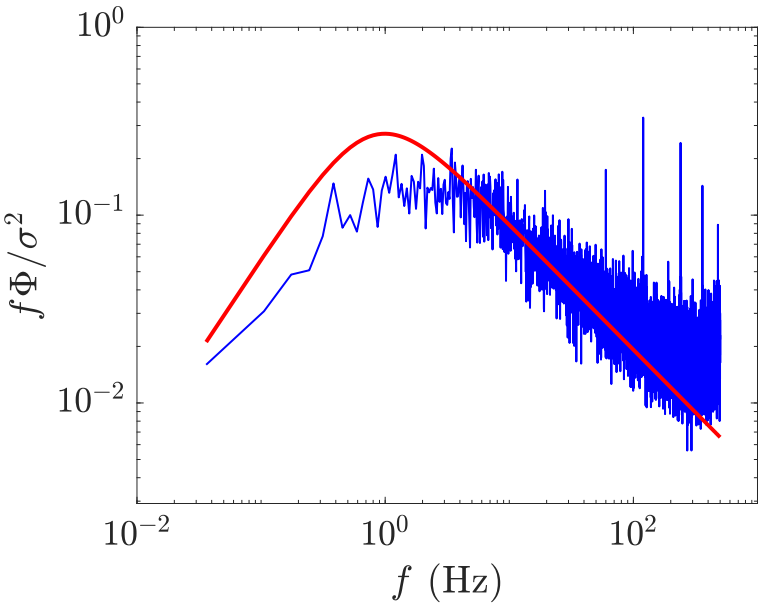

Figure 5.7: Comparison of measured spectrum at turbine hub height with ASCE standard 49-12 category C exposure (von Kármán theoretical spectrum), 50 DoF

The turbulence intensity of the incoming boundary layer over the extent of the model turbine rotor ranges from 5-8%.

It can be concluded that the inflow profile to the model turbine array, created by using spires to thicken the boundary layer and an additional 27 m fetch to develop the flow, provides a reasonable simulation in terms of shape of profile of the atmospheric boundary layer in the region of interest. If the ratio scales of the ABL and the turbines matched more closely, the steeper gradients of flow would be higher on the overall height of the turbine. It can be speculated that this may have caused additional mixing and quicker wake recovery.

5.2 Pressure Gradient

The FPF was designed to develop a zero pressure gradient (ZPG) turbulent boundary layer in an empty test section, with a ceiling that slopes upward to compensate for boundary layer growth (displacement thickness) from all four walls. The addition of objects in the tunnel test section creates additional flow displacement (blockage). The blockage for 5 turbines placed in the cross

section of the tunnel is calculated to be $<2\%$. A weakly favorable pressure gradient thus develops over the extent of the array. The pressure gradient was measured to be at most $\frac{dP}{dx} = -0.002$ over most of the array, or 32 meters of development, excluding the last two rows (18 and 19) where the pressure gradient adjusts as the flow moves first into an empty test section again, and then into the plenum at the end of the test section.

The pressure gradient can also be defined in terms of a pressure coefficient.

$$C_{pr} = 1 - (\frac{U_x}{U_{inlet}})^2 \tag{5.3}$$

Harun [62] conducted a study with favorable and adverse pressure gradient boundary layers to investigate when the turbulent structure is affected by the pressure gradient. The pressure gradient dP/dx was calculated using maximum velocities from the pitot tube placed at a height of 1.7 m from the wall which is also used to measure free stream velocity. The reference location used is the inlet ($x/D = 2$ upstream of the first row) free stream measurement of the array. C_{pr} is calculated for 17 rows of turbines. The pressure gradient boundary layer data of Harun [62] is compared with the array data in Figure 5.8. The maximum pressure coefficient value achieved in the FPF with the turbine array was -0.078, and would be classified as "very weak" with "no substantial difference [in the turbulent structure] from the ZPG case" [62].

5.3 Velocity Profiles

Figure 5.9 shows the velocity profiles at a downstream location of $x/D = 6$ for rows 1-17. The overlaid horizontal dashed lines are top tip height of the turbine, hub height, and bottom tip height, from top to bottom for reference. A 95% confidence band about mean velocity using the calculation from Section 4 are drawn around the velocity profile downstream of row 16. The uncertainty on the mean velocity points ranges from 1.7% to 4.4%. The maximum uncertainty for the dark black dashed line around the row 16 velocity profile is 2.1%. The velocity profiles are obtained with a pitot tube on a traversing system and U_∞ is measured concurrently at 1.2 m from the floor with a separate pitot tube.

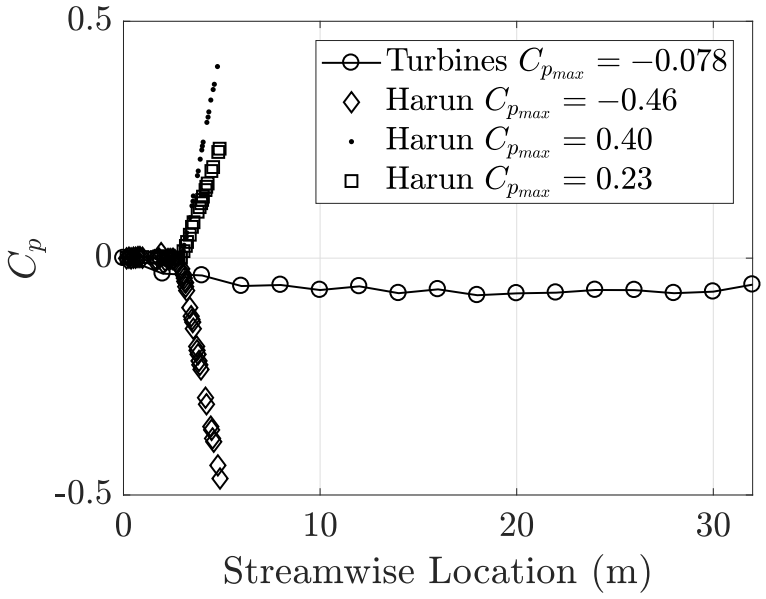

Figure 5.8: Coefficient of pressure from row 1 of the array moving downstream. Comparison to data of [62] starting at the entrance of that tunnel

The velocity profiles are shifting outward from the wall with increasing downstream distance consistent with the growth of an internal wind turbine array boundary layer. At any given height, the velocity decreases with increased distance downstream. Measurement region (II), that exists from from top tip height to $1D$ above hub height, is the so called equilibrium layer defined by Chamorro and Porté-Agel in 2011 [31, 90]. The equilibrium layer is the region where the flow is fully adjusted to the wind farm and can be seen to . Within the internal wind turbine boundary layer, where velocity and turbulent fluxes are highly modified, the knowledge of a consistent region of energy flux can be of great help to atmospheric modelers. In the equilibrium region, boundary layer and wake coupling start to exhibit self similar conditions which is noticeable in Figure 5.9 even without normalization of the data. The equilibrium region is most noticeably offset in the first few rows, as the profiles shift up and left towards a fully developed state. The relative location were the flow reaches a fully developed state is important. Large scale atmospheric models would treat the wind farm as an added roughness and this parameter should be obtained under equilibrium conditions where similarity theory can be applied [31].

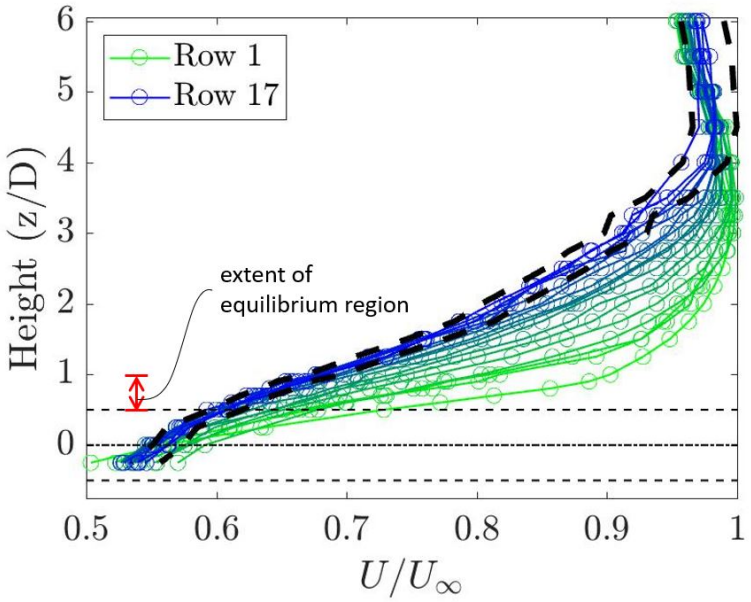

Figure 5.9: Velocity profiles normalized by freestream velocity measured at 1.2 m from the floor and turbine diameter. The black dashed line is the 95% confidence band around row 16. Maximum uncertainty on any mean velocity is 4.4%

A colormap is shown in Figure 5.10. Velocity is normalized by freestream velocity, the short vertical lines indicate the locations of the model turbines and the black dots indicate measurement locations (at $x/D = 6$). The wake after row 1 shows the highest velocity deficit, with some recovery further downstream, consistent with previous findings in array studies [34]. Various layers within the flow can be observed in this color contour plot. The outer boundary layer grows via downstream evolution; this can be seen by following the orange band of the region where $U/U_\infty \approx 0.9$. Additional forcing comes from the added flow displacement created by the turbines. The internal wind turbine array boundary layer continuously grows above the array, and can be observed in the green region where $U/U_\infty \approx 0.8$ magnitude. Within the array, there exists a qualitative consistency of the lower region of the flow, particularly below y/D =1 from approximately Row 11 on, where $U/U_\infty \approx 0.6 \ldots 0.65$.

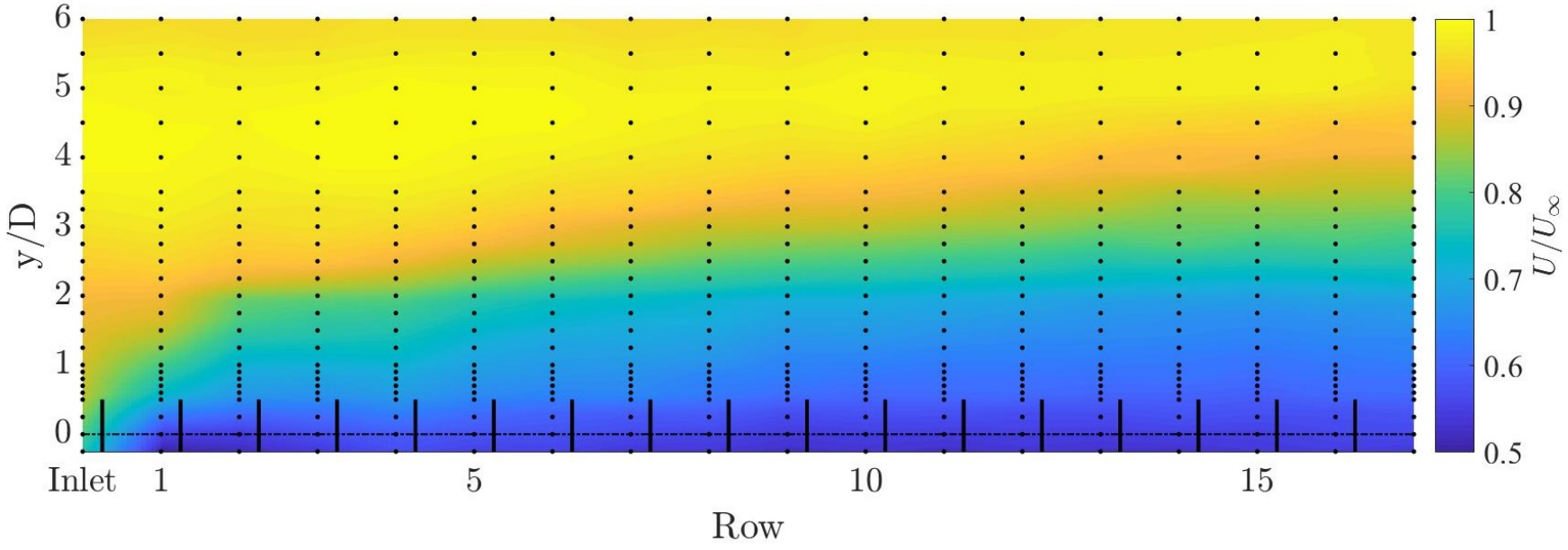

Figure 5.10: Velocity contour plot normalized by freestream velocity and turbine diameter. Measurement locations indicated by •, turbines indicated by thick black lines. Measurements were taken at 6 diameters behind turbine rows.

5.3.1 Outer Normalization

Following George and Castillo 2001 [29], the velocity data are plotted in outer variables, where the velocity deficit is normalized by the maximum velocity and the location is normalized by boundary layer height δ, calculated as the location where the mean velocity reaches 99% of the maximum velocity ($\delta = \delta_{99}$). Figure 5.11 shows the velocity profiles plotted this way, using the same color scheme as Figure 5.9. Figure 5.12 shows boundary layer heights at turbine row location

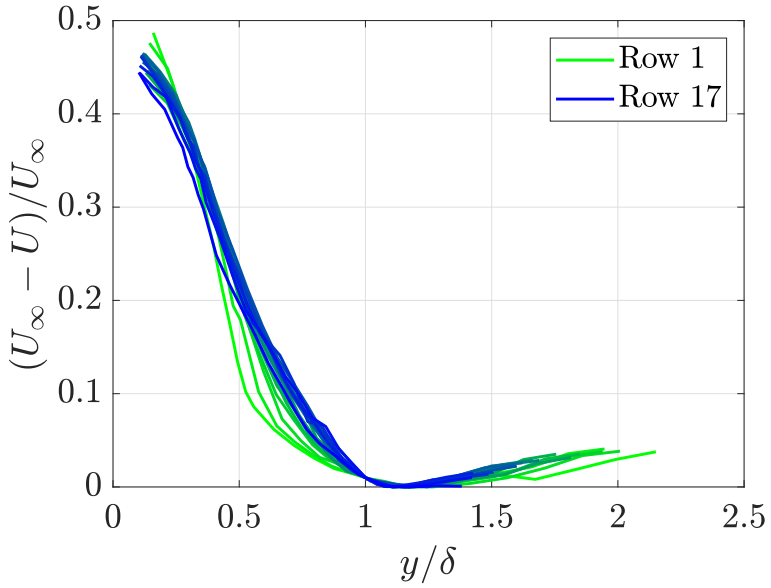

Figure 5.11: Velocity deficit normalized by the maximum velocity and boundary layer height δ_{99}. Same color scheme as Figure 5.9.

and is used when normalizing the velocity profiles by δ. It's obvious that the outer boundary layer height continually increases from Figure 5.12, however, excellent collapse is seen in the normalized variables beyond the initial transition which visually lasts until row 4, in agreement with Chamorro et. al [31]. After row 4 in Figure 5.11, the outer normalized deficit profiles appear to be similar, indicating that a similarity solution for the outer part of the flow exists.

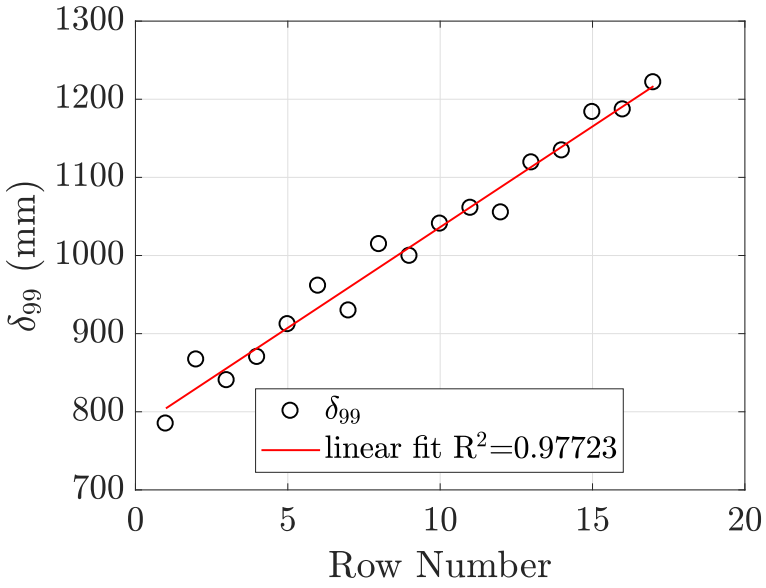

Figure 5.12: Boundary layer height δ_{99}, per vertical velocity profile taken downstream of each turbine row.

5.4 Determination of Fully Developed Condition in WTABL

A criterion is applied to different normalizations and regions of the velocity profiles to determine whether and where, from a mean flow perspective, the WTABL becomes fully developed. In this asymptotic regime, changes in the flow in the streamwise direction can be neglected in comparison to the wall normal direction [26]. Determining at what point the flow can be considered fully developed is nontrivial. This section deals with determining the fully developed condition by applying a coefficient of determination.

5.4.1 Coefficient of Determination

The coefficient of determination, or R^2 value, is one minus the ratio of two least squares regressions [18].

$$R^2 = 1 - \frac{SS_{res}}{SS_{tot}} \tag{5.4}$$

The ratio is formed by the residual sum of squares,

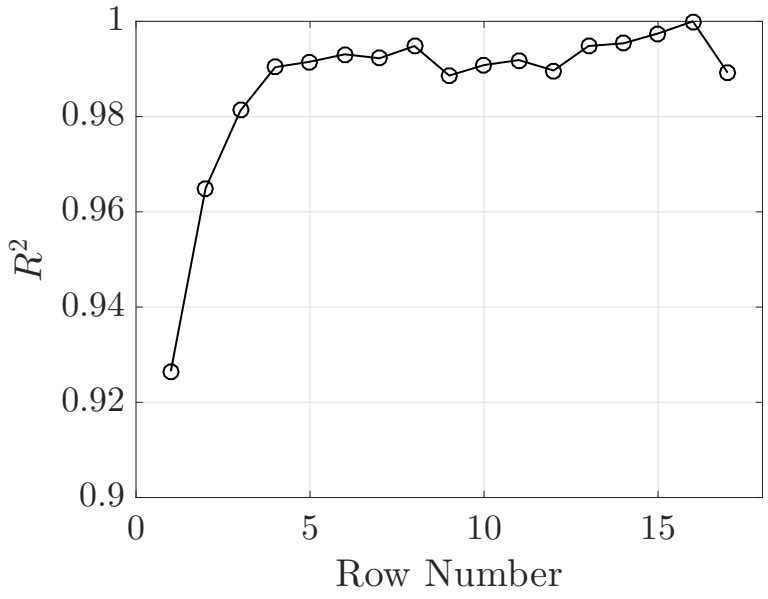

Figure 5.13: Coefficient of determination using velocity data of row 16 as the model f. Velocity profiles normalized by δ.

$$SS_{res} = \sum_i (y_i - f_i)^2 \tag{5.5}$$

where f is the modeled value and y is the observed data set, and the total sum of squares,

$$SS_{tot} = \sum_i (y_i - \overline{y})^2 \tag{5.6}$$

where $\overline{y}$ indicates the mean of the observed data. The coefficient of determination provides a numerical representation of how two or more random variables are interrelated [18].

In this analysis, the velocity data of row 16 are used as the model f to compare to the other velocity profiles. Row 16 is assumed to be in the fully developed region of the WTABL flow. The velocity data of row 17 were not used as the model, as they may already have been affected by the flow deceleration due to reduction in blockage at after the end of the array (row 19), see the discussion of pressure gradient and Figure 5.8. Additionally, the expansion of the tunnel to the plenum near the end of the test section may change the pressure gradient slightly and could effect the velocity. In Figure 5.8 the very last point is slightly higher than the rest amounting to

20% different from the second to last point, whereas none of the previous ten C_{pr} values differ from their neighbors greater than 10%. For these reasons, the velocity profile of row 16 is used as the model for the determination of the fully developed condition. The criterion, applied to the velocity profiles, is plotted in the following normalizations and profile regions, with their symbolic representations in Figure 5.14 noted.

- The full velocity deficit profile, with wall normal height normalized by local boundary layer thickness; "○", y/δ
- The full velocity deficit profile, not normalized with wall height; "∗", y
- The velocity deficit of the equilibrium region only, applied to the six data points above turbine tip height, not normalized with wall height "△", Eq

There are differences between how a "classical" turbulent boundary is generated and evolves downstream versus how the wind turbine array boundary layer is generated. All internal sublayers of a turbulent boundary layer over a flat plate (inner layer, buffer layer, meso-layer, outer layer) move away from the wall as the boundary layer evolves and grows downstream, including the outer layer [54, 78]. Therefore the wall-normal location of where the "outer part" of the TBL begins moves further away from the wall in physical coordinates, and hence outer normalization (as applied in Figure 5.11) is warranted. The wind turbines are the generators of the WTABL, which manifests itself as an internal layer to the larger turbulent boundary layer.

The entire wind turbine rotor is within the "outer part" of the classical turbulent boundary layer (by design, since it is trying to reach higher velocities, i.e., a better wind energy resource $P \propto U^3$), however, the turbines remain at a fixed wall-normal distance throughout the array. The flow through large wind turbine arrays can thus be interpreted as a boundary layer flow with a sparse displaced roughness (SDR), in contrast to classical rough-wall boundary layers, where the roughness is attached to the wall. In a classical rough-wall boundary layer, the inner layer and therefore all other layers, are displaced by the presence of the wall roughness [42]. In the WTABL, an internal layer that remains at a fixed vertical distance from the wall, is generated by the SDR.

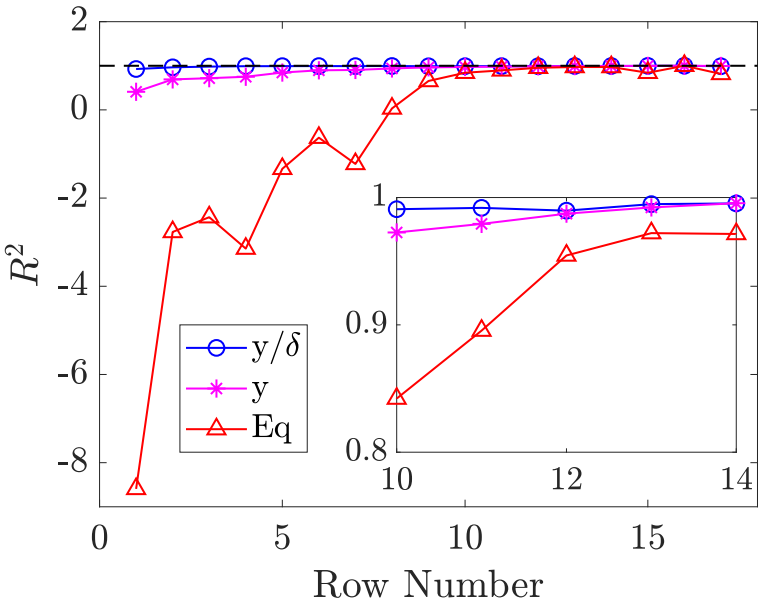

Figure 5.14: Coefficient of determination using velocity data of row 16 as the model f. y/δ: Outer normalized. y: Velocity deficit. Eq: Equilibrium region only.

Therefore it will be useful to apply the coefficient of determination criterion to normalized and non-normalized velocity profiles, for different regions of the flow, and compare the results.

Considering the normalized velocity deficit profiles in Figure 5.11, a coefficient of determination (R^2) is calculated over the entire velocity deficit boundary layer normalized profile, y/δ. In this boundary layer normalized velocity comparison to the row 16 model, after row 4 the R^2 value exceeds 0.99 as seen in Figure 5.13. This is a good indication that our cursory look at the velocity deficit normalized velocity accurately displayed agreement beyond the first 4 rows of transition. This would lead one to believe incorrectly the flow becomes fully developed very quickly, after row 4. However, the velocity profiles were broken up into three normalization categories and will be examined here. A coefficient of determination calculation is done for the velocity deficit of the equilibrium region of the flow, Eq, and compared to the full profile velocity deficit boundary layer normalized values, y/δ, and the full profile velocity deficit non-location-normalized values, y. These values are compared in Figure 5.14. Row 16 is again chosen as the model. Decreased values of R^2 for y compared with y/δ is seen as expected. For Eq, the R^2 values show the pro-

files are very dissimilar from the model in row 1-10. After row 11, the correlation is above an R^2 of 0.9. The interest is placed on examining the region just above turbine tip height, Eq. With a focus on the Eq R^2 values, arguably the most relevant space to give attention, one should draw the conclusion that the flow is fully developed in the mean velocity starting at row 12. Finding a "fully developed" region that does not vary with a cross-stream normalization essentially says that a near-parallel flow regime has been achieved, where the streamwise growth is significantly less than that of the external boundary layer.

Concluding that the WTABL is fully developed at row 12 is a unique result specific to this experiment's exact boundary conditions and array set up and spacing. It is recognized that this determination cannot be easily copied and immediately applied to full scale wind farms due to the changes in turbine spacings, different tuning, wind conditions, etc. The goal of the fully developed determination in this configuration lies in the hopes that full field modelers will have the ability to reduce computation time with some knowledge of a consistent energy extraction from the array at some point downstream. This data set is publicly available (See Appendix A) and will be able to calibrate models using actuator disk methods. Currently, the concept of the infinite wind farm is implicitly assumed in some simulations where the domain is the full atmosphere and wind farms are parameterized by means of an induced surface roughness [101, 77]. In these works, the modeler is investigating the impacts of wind farms on meteorology [14]. Additionally, increased knowledge of the flow field and specifically the array velocity transition to a sustained internal farm velocity is useful to validate other physical data sets and full scale measurements.

5.4.2 Integral Thicknesses

Figures 5.15 and 5.16 show the displacement thickness and the momentum thickness respectively. The Reynolds numbers on the abscissa is defined as $\delta^+ = u_{*hi}\delta/\nu$ with the friction velocity

$$u_{*hi} = \sqrt{\frac{H}{\rho}\frac{dP_\infty}{dx}} \tag{5.7}$$

where H is the height at which the pressure gradient term is measured. In this instance the maximum velocity per profile is used which varies in height. This definition of friction velocity is restated from Frandsen's theory in Meneveau et. al. (2010) and reused in a sequential paper, and is prescribed above the wind turbine canopy[26, 90]. The displacement thickness does not see much change row to row as the majority contribution comes from near wall points, within the turbine canopy. The momentum thickness can be approximated to level off near $\delta^+ \approx 3900$ which corresponds to row 11 or 12.

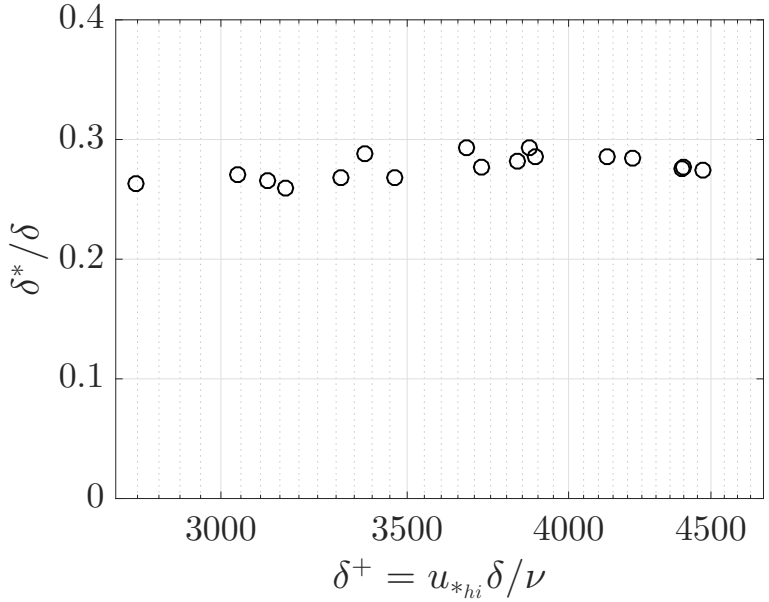

Figure 5.15: Displacement thickness $\delta^* = \int_0^\infty (1 - \frac{U}{U_\infty})dy)$

Figures 5.17 and 5.18 are representations of the displacement thickness δ^* and momentum thickness Θ contributions at 30 equally spaced points from the wall. The velocity profiles obtained in the turbine array did not have data points at locations very near wall and so a point was created at zero distance away from the wall at zero velocity to complete the profile. The displacement and momentum contributions tend towards zero with increased distance from the wall. Once the boundary layer height is reached for that downstream location, the additional equally spaced contribution locations are forced to zero. Vertical locations past the maximum velocity and boundary layer height do not contribute to the integral thicknesses, nor were plotted, and it can be seen that

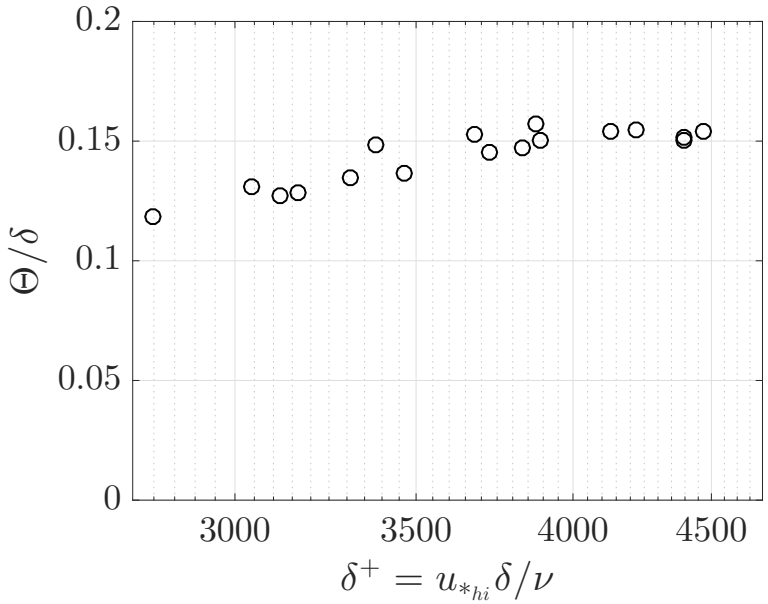

Figure 5.16: Momentum thickness $\Theta = \int_0^\infty \frac{U}{U_\infty}(1 - \frac{U}{U_\infty})dy$

some of the profiles do not have 30 integral contribution points. It is seen that a large portion of the displacement thickness comes from near wall points, while very little of the momentum thickness comes from near wall points. Within the turbine wake and below, the integral thickness contributions are very similar at all downstream rows. Above the turbines, in the outer boundary layer flow, the contributions to the integral thicknesses become more disparate. With further downstream progresses into the array, the contributions become increasingly self similar, which is to be expected considering the ease of collapse of the velocity profiles.

Figures 5.19 and 5.20 show the contribution to the displacement thickness and momentum thickness that comes from the equilibrium region. It is shown here to be leveling off in both δ^+ and Θ around $\delta^+ \approx 4000$, corresponding to 12 rows of turbines downstream. This further pressures the observer to contend that the fully developed nature of this flow exists starting at row 12. At this location in the array, the vertical kinetic energy flux balances the power extraction of the disks and the velocity becomes statistically stationary in rows thereafter, which is how the fully developed condition is defined. Further investigation can be given to the turbulence statistics that within the array which should also asymptotically approach a stationary state.

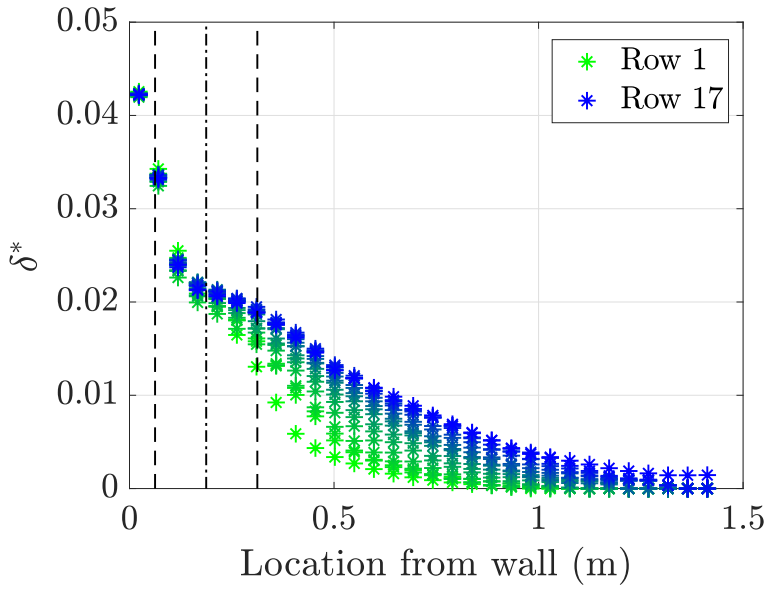

Figure 5.17: Displacement thickness contribution profile from an equally distributed 30 points along the vertical height of the profile

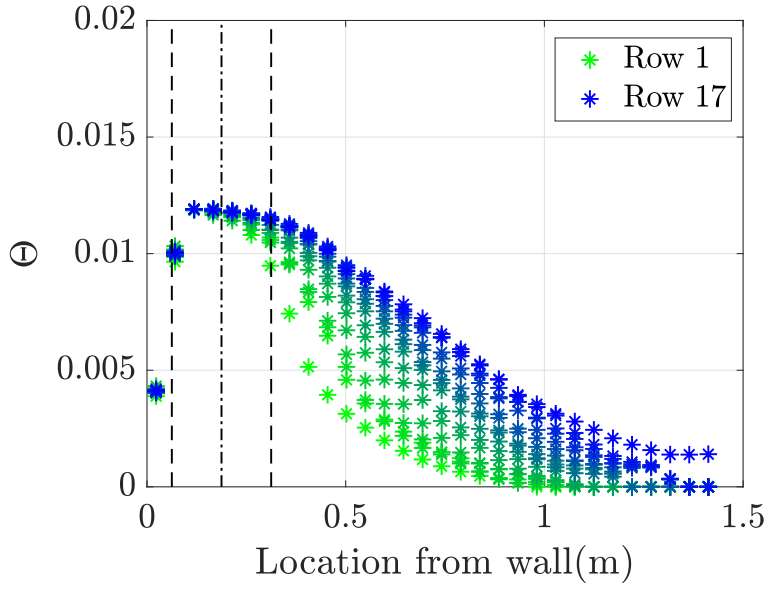

Figure 5.18: Momentum thickness contribution profile from an equally distributed 30 points along the vertical height of the profile

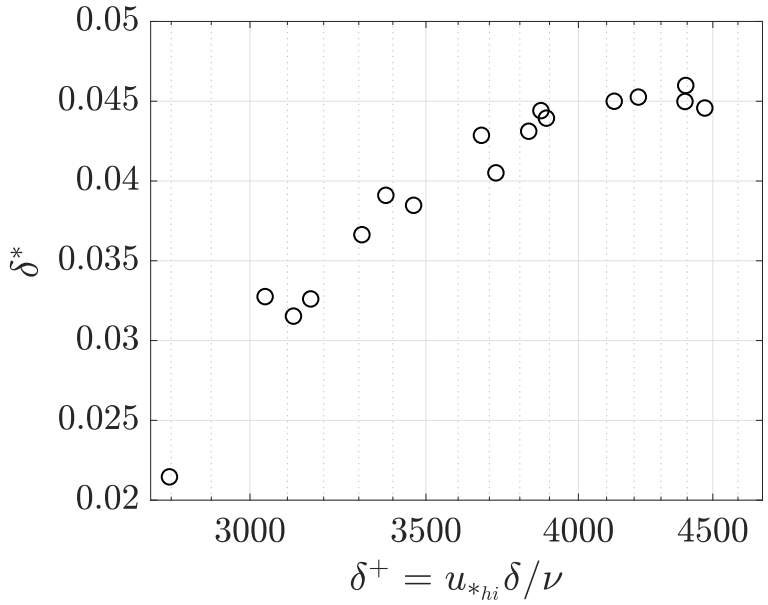

Figure 5.19: Displacement thickness contributions from the equilibrium region

5.5 Summary

A large experimental wind farm has been constructed and placed in a boundary layer wind tunnel. The model turbine spacing was 8 diameters in the streamwise direction, and the model array extended over 19 rows, or 36m, with the first turbine row placed 33m downstream of the wind tunnel inlet. Spires were used to thicken the inflow boundary layer and ensure a realistic ratio of boundary layer thickness vs wind turbine height. This study has provided useful knowledge on the complex developing flow of a WTABL, who's origin wall normal location remains fixed in space while the external ABL continues to develop. This was interpreted as a boundary layer flow with a *sparse displaced roughness* (SDR), in contrast to classical rough-wall boundary layers, where the roughness is attached to the wall Using boundary layer height as an outer normalization for the velocity deficit, the profiles collapse well after row 4. The experimental array is shown to become statistically stationary in the mean using a coefficient of determination criterion with specific attention given to the equilibrium region (just above turbine top tip height). Row 16 was used as a model for the coefficient of determination, the WTABL becomes fully developed in the mean flow

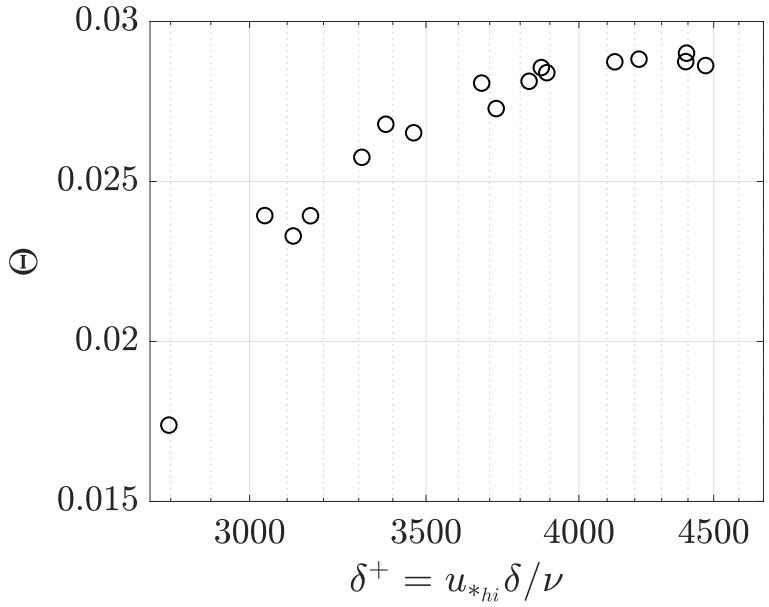

Figure 5.20: Momentum thickness contributions from the equilibrium region

from row 12 on. Integral terms also exhibit consistent behavior start at row 12. Knowing when an array reaches a fully developed state will enable enhanced predictions on generative capacity of the array. Knowledge of this fully developed state existing in a physical experiment of porous disks for a given configuration will help us better understand the balance of power extraction of the turbines with maintained atmospheric boundary layer growth above the canopy of the array. This benchmark data set will help the understanding of base condition asymptotic limits in a defined set of conditions. This work should be helpful for numericists to calibrate in situ wake boundary layer behavior, and thusly bulk power production in models. A data set for a case that has a realistic spacing of turbines in an offshore array was presented. Whether and how strongly the location that the flow reaches a fully developed boundary layer state depends on wind turbine spacing remains to be investigated.

CHAPTER 6

TURBINE WAKE MEANDERING

Large scale atmospheric eddies dominate the directional advection of the wake of single turbines. This atmosphere wake interaction, a dynamic shift in the wake over time in the rotor plane direction, is a phenomenon known as wake meandering [22, 38]. This motion of the wake causes the mean deficit in the flow to be instantaneously inconsistent from a time averaged sense, which will effect the incoming flow field for downstream turbines. The larger than rotor diameter eddies are primarily responsible for the non periodic forcing on the wake that cause meandering [44]. Unlike a bluff body shedding frequency, the meandering phenomenon for a turbine is not characterized by a well-pronounced peak in the frequency domain, but rather by a bumb spread over a larger low-frequencies range (1–10 Hz for this scale object). Here, a peak is detected in the frequency domain that contains a dominant amount of energy. For the purposes of this study, this peak is assumed to be the meandering of the wake, as no visual evidence in this exact set up can currently confirm this. See section 2.2.6 for more background on wake meandering.

This chapter is dedicated to the investigation of wake meandering behind single model turbines in a boundary layer flow and within an array of model turbines. Single turbines and a fully developed array of 19 rows and 5 columns of porous disk and bladed turbines were positioned within a the boundary layer in a large boundary layer wind tunnel. High temporal resolution velocity time series were obtained at high enough frequencies to resolve peak frequency trends, or Strouhal number, which scale geometrically with turbine diameter [65], downstream of individual and coalescing wakes of turbines. For bluff bodies the shedding has defined Strouhal numbers

$$St = \frac{f_s D}{U} \tag{6.1}$$

and the wake oscillation is sinusoidal [117]. In this case the vortex shedding characteristic length scale is $D = 0.25$ m, the diameter of the turbine. The shedding frequency is defined as f_s and the characteristic velocity is U. The characteristic velocity used here is the hub height velocity of approximately $U = 4$ m/s, so we expect Strouhal numbers of $St \approx 0.22$, following measurements made by Coudou [38]. With these base parameters identified, it is expected that the meandering of the wake be approximately $f_s = 3.5$ Hz.

The meandering of the wake of a single object decays with downstream distance. Wake meandering also presents itself in large experimental arrays and far downstream the peak meandering frequency is dominated by the turbine spacing. The relationship between large scale meandering and small scale turbulent motions in the wake is also investigated. Evidence is found of amplitude modulation on the energy of small scales by a decomposition of the velocity time series.

6.1 Model Turbine Wake

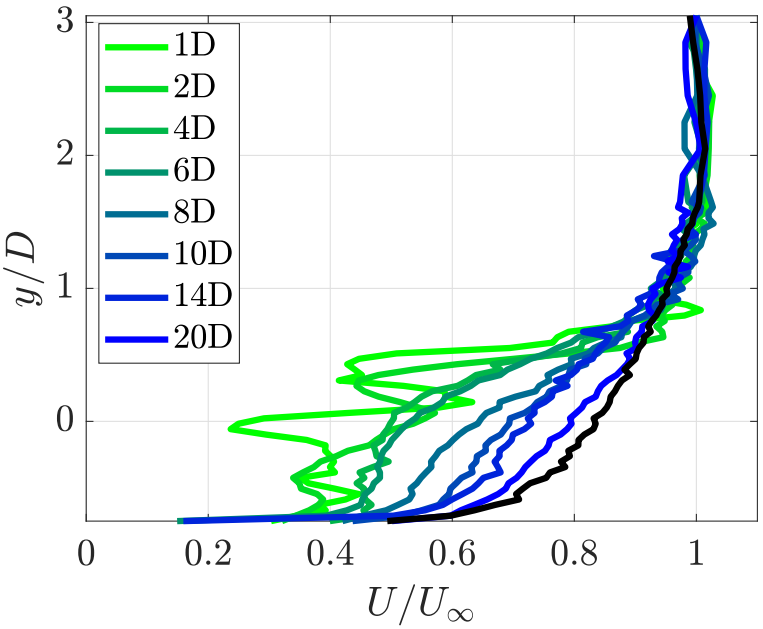

Figure 6.1: Normalized velocity wake measurements in the boundary layer downstream of the turbine. The solid black line represents the incoming boundary layer flow.

Figures 6.1 and 6.2 show the wake measurements in the boundary layer downstream of the turbine and the porous disk at various downstream positions normalized by free stream velocity.

The solid black line represents the inlet turbulent boundary layer profile, also shown in Figure 3.11. The initial velocity deficit in both objects is large, and decays back towards the velocity profile of the inlet with downstream evolution.

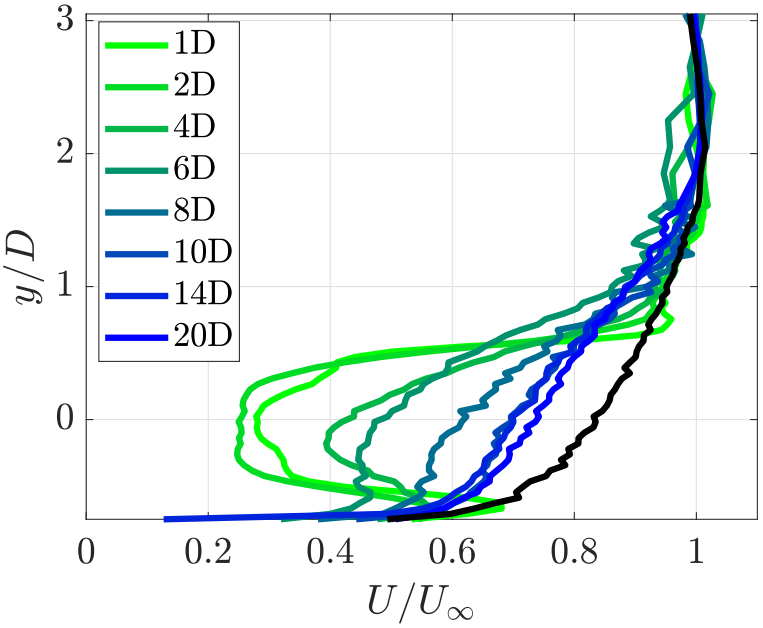

Figure 6.2: Normalized velocity wake measurements in the boundary layer downstream of the porous disk. The solid black line represents the incoming boundary layer flow.

In Figures 6.1 and 6.2 the wakes show a large velocity deficit in the near-wake at low x/D, and then recover towards the undisturbed, incoming boundary layer profile at higher x/D. At 20 diameters downstream, about a 10% difference to the incoming boundary profile can still be observed at hub height in both cases, but the momentum overall has recovered significantly. For the turbine (Figure 6.1) evidence of hub and tip vortices can be seen in the near-wake, whereas the porous disk near-wake (Figure 6.2) more closely resembles that of a bluff body. Progressing further downstream, say 10 to 14 diameters, the velocity deficit is seen to mostly recover and the velocity profiles in the wake become increasingly similar. Figure 6.3 shows comparisons of the vertical wake velocity profiles of the porous disk and turbine at various downstream distances. The turbine is indicated with symbol "×" and the disk is indicated with symbol "○". It was determined that the wakes of the porous disks and model turbines become sufficiently similar in this setup at a

downstream distance of 6 D to build up an array of both objects in these experiments. The array using a combination of porous disks and model turbines is space in the stream wise direction at 8 D.

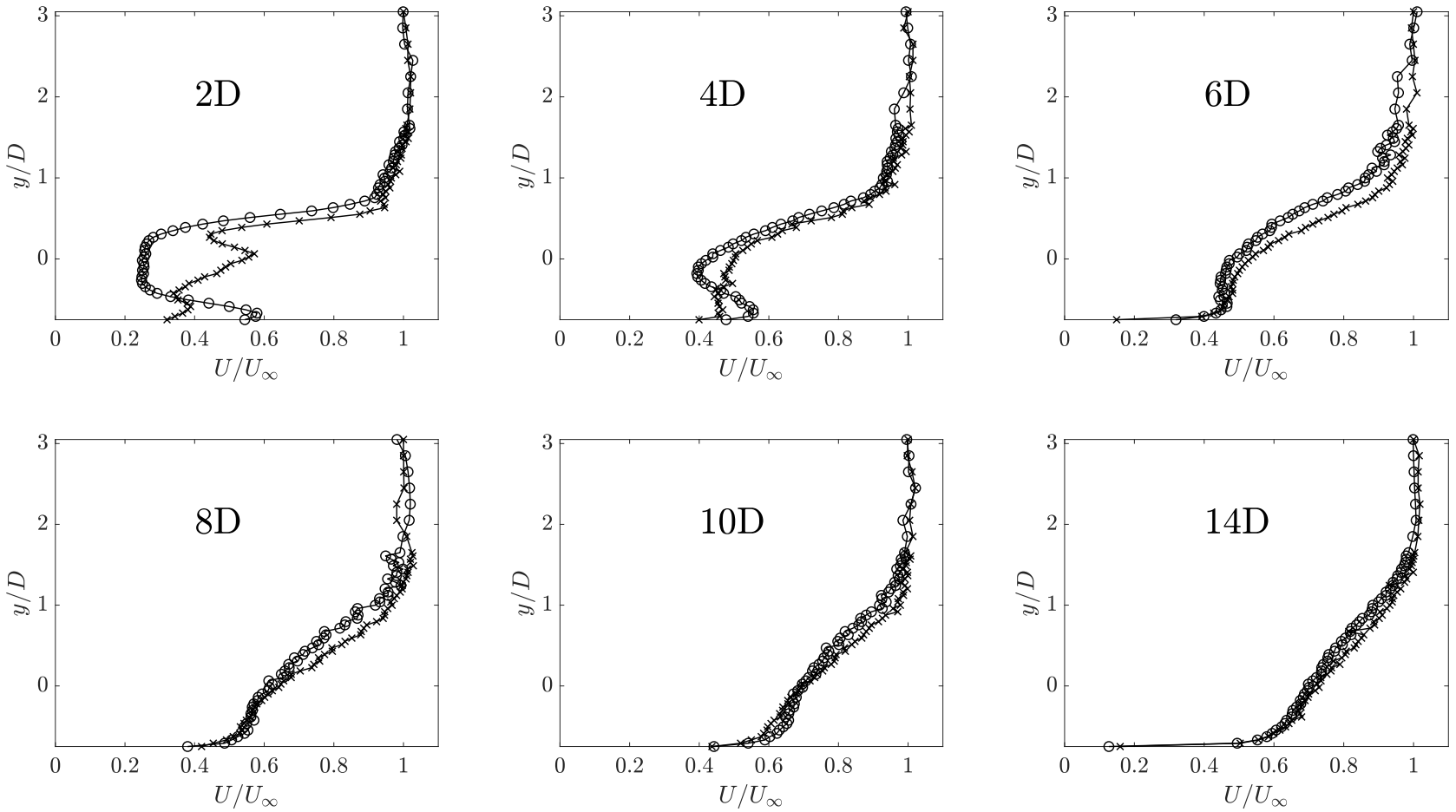

Figure 6.3: Wake comparison of the rotating model turbine and porous disk at various downstream positions. The turbine is indicated with symbol "×" and the disk is indicated with symbol "○"

.

6.2 Analysis Methods

The analysis of the time series' obtained in this measurement campaign is summarized here prior to going into a bit more detail. First, the spectrum of the velocity time series is calculated. Then, the spectrum is multiplied by frequency to produce the energy spectrum. A spectral energy peak is found using a regression algorithm and the corresponding frequency and energy content are obtained from the peak value of the regression. The premultiplied spectrum is useful for visualizing energetic peaks. It is assumed that the spectral energy peak is the meandering of the wake. These peak values are then plotted at different downstream locations from the object or within the array at different wall normal heights.

6.2.1 Fourier Analysis

To understand the power spectral density, first a discussion of Fourier Analysis is presented. The application of Fourier Analysis is derived from the study of Fourier Series and allows a user to represent analog functions by summations of trigonometric functions. The easiest way we conceptualize this process is when one listens to music. The first 5.5 seconds of Lynyrd Skynyrd's Sweet Home Alabama [105] is plotted in Figure 6.4. The time series of pressure waves known as sound

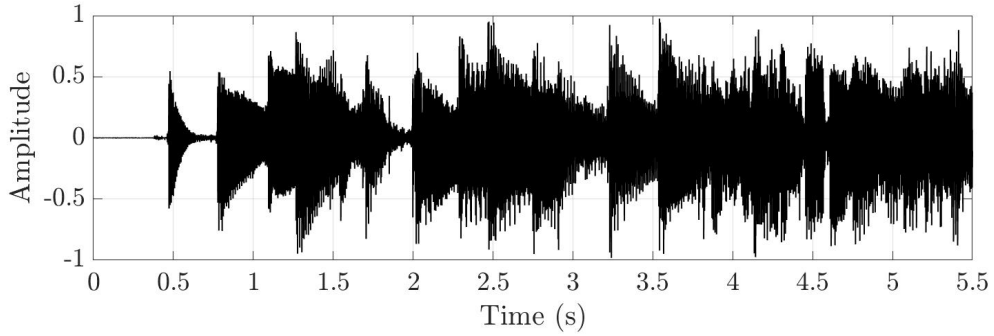

Figure 6.4: Amplitude plot of the first 5.5 seconds of Lynyrd Skynyrd's Sweet Home Alabama [105]

can be decomposed by Fourier Analysis. Fourier Transforms allow the user to go back and forth between the time and frequency domains. A typical Fourier Series would have the structure

$$y(t) = \sum (a_n cos(2\pi f_n t) + b_n sin(2\pi f_n t)) \tag{6.2}$$

which is a summation of sines and cosines [18]. For our purposes we will rewrite this summation in complex exponential form and define the Discreet Fourier Transform as

$$\hat{G}_j = \frac{1}{N} \sum^{N-1} g_n e^{-i2\pi jn/N} \tag{6.3}$$

where $\hat{G}_j$ is the Fourier Transform of the real time series g_n. This process is laborious for any large time series and so the Discreet Fourier Transform is typically computed using a fast Fourier Transform (FFT) algorithm. For more information on how and why the FFT is practically faster than the Discreet Fourier Transform, please see Bendat and Piersol [18].

The FFT is utilized to bring our real valued time series into the frequency domain and we calculate the power spectral density to assign energy values over a defined time interval as in equation 6.4.

$$\hat{S}_j = \hat{S}(\frac{j}{\Delta N}) = N\Delta \hat{G}_j \hat{G}_j^\star \tag{6.4}$$

$\hat{S}_j$, otherwise written as $S(f)$, is the power spectral density with $\hat{G}_j^\star$ being the complex conjugate of the FFT. If our time series g_n is real, which it is as we are dealing with flow velocity time series, the $S(f)$ returns a symmetric distribution of values in the frequency domain about $f = 0$. We will only concern ourselves with the positive frequencies, in this case indicating the amount of energy that the flow has at those frequencies.

Back to our music example, the FFT allows you to determine what frequencies are present in the song, and perhaps even how to recreate it (at least, you now know what 'notes' are being played). Figure 6.5 displays the power spectral density of the first 5.5 seconds of Lynyrd Skynyrd's Sweet Home Alabama [105] with specific peaks of frequency being labeled with notes. It can be seen that the tallest peak is labeled with the letter 'D' as Sweet Home Alabama starts on the note 'D' in the key of G major and is the most common note in the first few seconds, which is why this frequency (587.33 Hz) contains the most energy here.

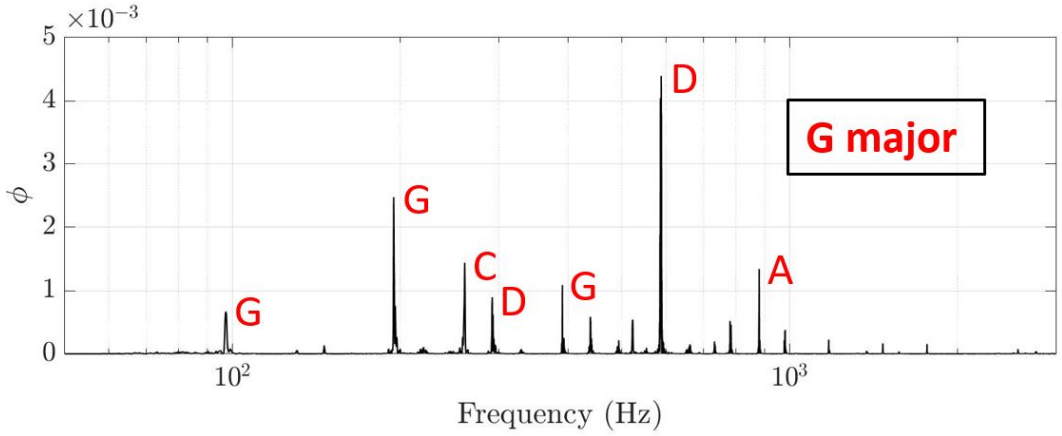

Figure 6.5: Power spectral density of the first 5.5 seconds of Lynyrd Skynyrd's Sweet Home Alabama [105] with specific frequencies indicated in notes.

6.2.2 Power Spectral Density

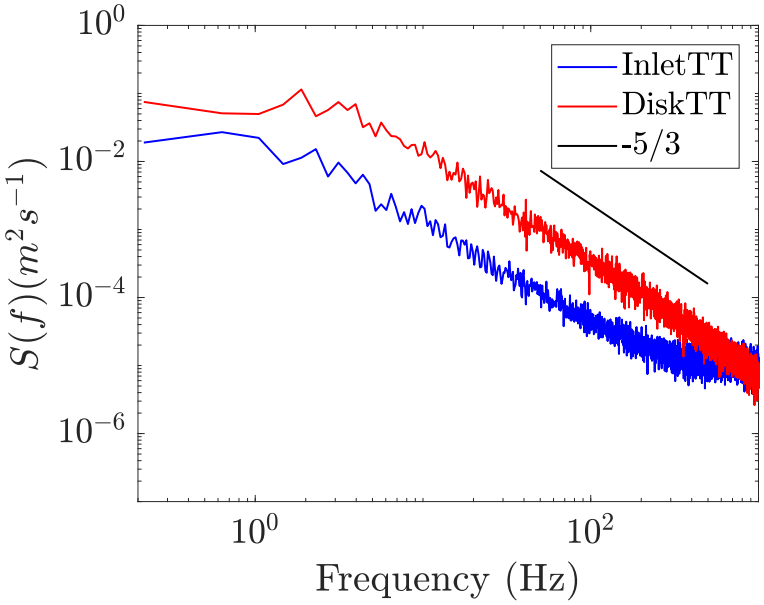

Figure 6.6: Inlet and Disk top tip spectral comparison with a $f^{-5/3}$ slope for reference

Figure 6.6 is a variance conserved one sided power spectral density $S(f)$ comparison of the inlet and 6 D downstream of a Disk at top tip height with a $f^{-5/3}$ slope for reference plotted with 50 degrees of freedom (DoF). The wake of the disk has increased energy in the spectrum at all

frequencies. The disk generates turbulence which increases variance in the frequency domain, while decreasing momentum in the wake.

It can be noticed in Figure 6.6 that the spectra do not drop off in the low frequencies. Generally, in most geophysical processes, energy starts at low frequencies (large scale motions) and cascades to the higher frequencies (small scale motions). However, there should be a drop off in the very low frequencies, indicating the scale of the process. It is expected that the lowest frequencies would have less energy than the dominant scale of the process. There is a potential that the resonance of the wind tunnel test section influences the energy input into the spectra. The tunnel resonance in this case would be the largest scale that would influence the energy of the process. This type of system influence has been briefly mentioned in [114]. The FPF is 72 meters long and in this study operates at a nominal 6.7 m/s. This means that a single turnover of a tunnel volume of air passes through the tunnel in about 10.5 seconds, or a frequency of 0.09 Hz. The time series examples discussed here are only one minute long and with 25 bands, figure 6.6 is only plotted to about 0.2 Hz so we are unable to see the influence of the tunnel resonance.

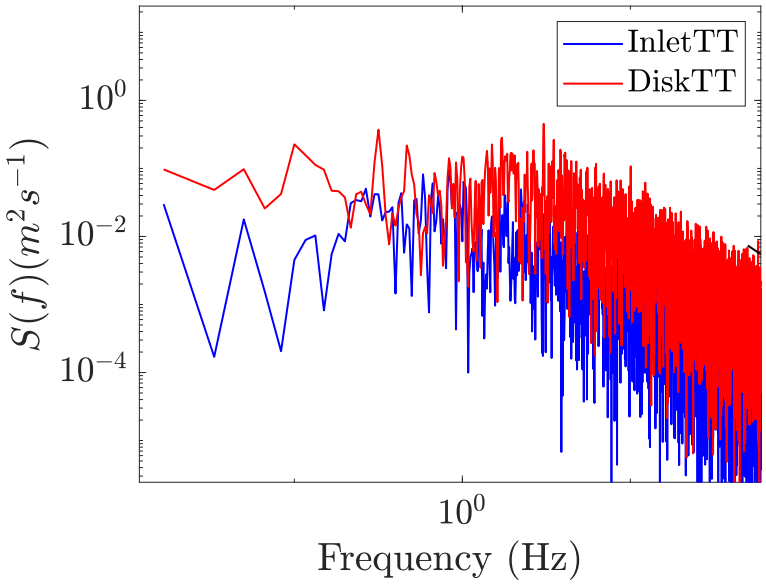

Figure 6.7: Inlet and Disk top tip spectral comparison with 2 DoF. Focus here is the on lower frequencies.

In Figure 6.7, the same data as Figure 6.6 is plotted with the minimum smoothing, one band and one ensemble, or 2 DoF, and zoomed up on the lower frequencies. With 2 DoF we are able to view all potential frequencies that the time series can resolve, or 1/60 seconds (for a one minute time series) which is $0.01\overline{6}$ Hz. It can be seen that when the non-smoothed spectra is presented, the energy at these lower frequencies is relatively flat. The energy at these low frequencies could be lower than presented, but with a relatively short time series, it is difficult to resolve. As per usual, the answer to higher resolution comes from obtaining a longer time series, but considerations of external weather influences and overall time constraints limit these efforts. Figure 6.7 is a good example of why spectra are smoothed in general. The smoothing cleans up the variation in energy and presents a less chaotic picture like in Figure 6.6. What can be said is that a peak from potential tunnel resonance is not seen, so the energy here may be coming from some external influence, like a long period temperature variation. Rather, the lowest frequencies relating to a geophysical timescale are not being resolved due to time series length. Lower frequencies aside, the focus will now be shifted to finding peaks of wake meandering in the 1-10 Hz range.

6.2.3 Peak Finding in the premultiplied spectra

To find the most energetic structures in the velocity time series, the spectrum is premultiplied by frequency to obtain the energy spectrum $f \cdot S(f)$. This method is also used in a wake meandering study of wind tunnel and field measurements by Heisel et. al. in 2018 [65]. The energy spectrum is applied for a defined length of time signal that contains finite energy. The peak energy content becomes more visible when multiplying by frequency and acts as a dynamical interpretation of the flow visualized by $S(f)$. The peak of this energy spectrum is located by means of polynomial regression for every time series. The spectra is averaged with 10 bands over 1 ensemble (20 DoF) and the hanning window is applied in an attempt to minimize the spectral leakage and help clarify the peak. The meandering phenomenon is not an exact periodic display of vortex shedding, but a dynamic shift in the wake over time; therefore we expect a small section of the spectrum to be raised in the 1 Hz – 10 Hz region instead of a defined single peak. It can be noted that turbulence

profiles of the wake of the model turbines are not included here. Electrical noise was present in some of the profiles in the high frequencies that affected the profiles. Because the noise was present in the high frequencies, the peak finding method presented here should not be effected due to the low frequency range examined.

To create a polynomial fit that is appropriate, the logarithmic spacing of binned frequencies in the spectrum is accounted for. The regression range is discretized and interpolated to normalize the weights of the log spaced binned frequencies. Figure 6.8 shows an example of a 5^{th} order

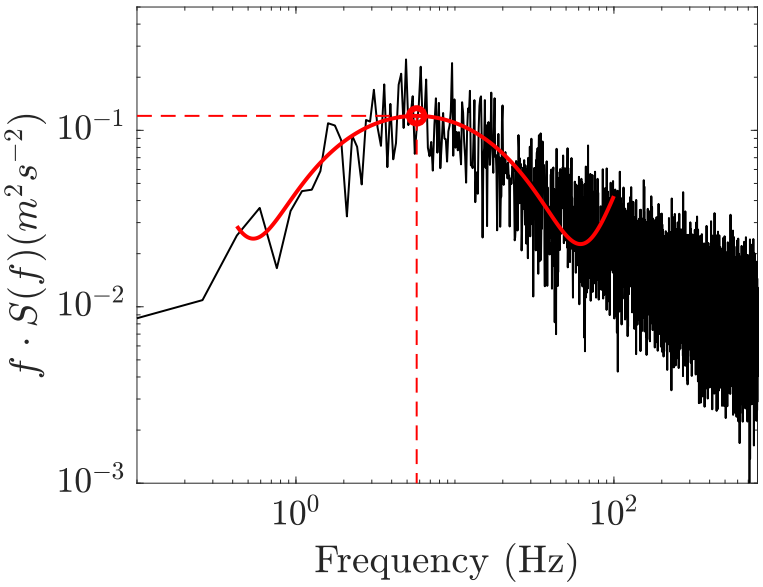

Figure 6.8: 5th Order polynomial regression on energy spectrum of the disk in the boundary layer measured vertically at top tip height at 6 diameters downstream

polynomial regression fit from 0.5 Hz – 100 Hz on the energy spectrum of a single porous disk in the boundary layer with time series measured at wall normal top tip height at 6 D downstream. The overlaid red line represents the regression. The peak of this regression is used as the corresponding maximum frequency which is used as that object's meandering frequency at a given wall normal location. This regression method was used to deduce the spectral peaks for all time series locations.

6.2.4 Comments on repeatability

A 5^{th} order polynomial is fit to the spectrum from a range from 0.5 Hz to 100 Hz. Simply taking the maximum value in the energy spectrum is unreliable owing the variance of the measurement. Hand picking the peak region by eye would bias the results and is also unreliable. Further smoothing with additional bands or ensembles and then averaging spectral peaks was considered, but this creates uncertainty of the raw peak frequency in the spectrum due to the record length and binning of the low frequencies creating a frequency locked result. With other methods considered, a regression is used.

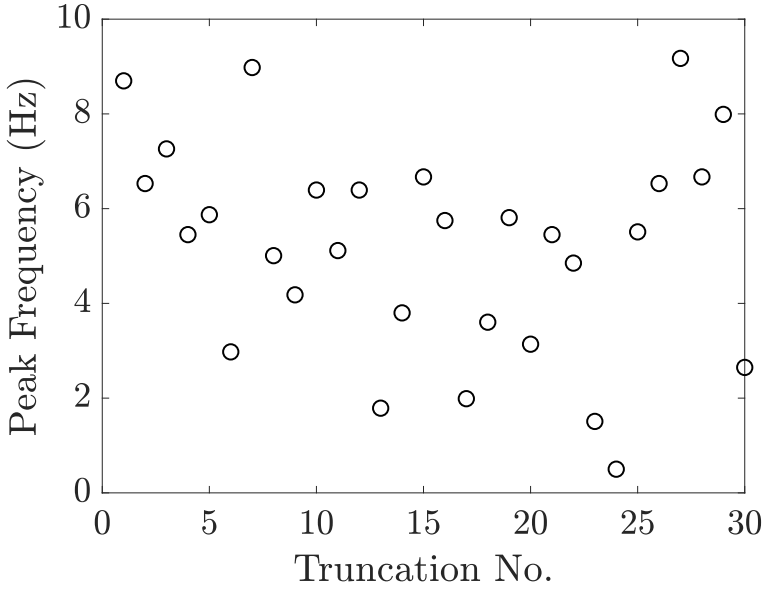

Figure 6.9: Peak frequencies found for each of 30 two-second time series

The ability of the regression to find the peak in a repeatable manner is examined here. The regression used to determine the peak frequencies has certain boundary conditions that can be changed. A study was performed modifying the parameters that effect the determination of the peak frequency. The parameters that were modified include

- The frequency bounds of the regression
- The order of the regression
- The number of DoF in the spectrum
- The length of the time series

Every parameter modifies the resultant peak frequency by a few percent, but it was quickly seen by modifying the parameters above that the length of the time series was the largest contributor by an order of magnitude.

The regression frequency bounds are maintained at 0.5 Hz to 100 Hz, which centers the regression around 10 Hz on a log scale. The length of the time series was modified by truncating finer sections (e.g. two 30 second time series, six 10 second time series, for a one minute data set) it was found that the longer the time series, the finer the resolution at the lower frequencies. Another negative to shortening the time series is that it generally increases the variance between truncated sections. A plot of different peak frequencies obtained by truncating a single one minute time series into 30 two-second time series is shown in Figure 6.9. The one minute time series used here is $x/D = 6$ downstream of the disk at a vertical location of top tip height. For each smaller two second time series the premultiplied spectra is calculated. There does not seem to be a distinguishable trend over the course of the time series. The peak frequency does have significant variance over the data set when truncated this way. The single one minute time series is truncated into smaller time intervals and the peak frequencies are calculated with the algorithm in Figure 6.10. A dashed red line indicates the peak frequency with the full one minute time series. It can be seen that the variation of peak frequencies decreases with increased time series length. Longer time series increase the resolution of the low frequencies in the premultiplied spectra and help calculate a more reliable estimate of the larger scales.

At a single location, if we consider Taylor's frozen flow hypothesis, we are able to see or measure the scale of passing eddies based on their measurement at a stationary location. For instance, if we are to view a passing eddy for 2 seconds and the flow speed is 4 m/s, we would be able to resolve an eddy of scale 8 meters, or a frequency down to 0.5 Hz. However, this would only be one single event, which would decrease the reliability of this event. If we increase the amount of time to view the flow to 10 seconds, we could view an event of 8 meter scale five times, increasing our reliability of seeing that type of event. In Figure 6.10, we are capturing the increased reliability of finding that peak frequency with increased length of time series.

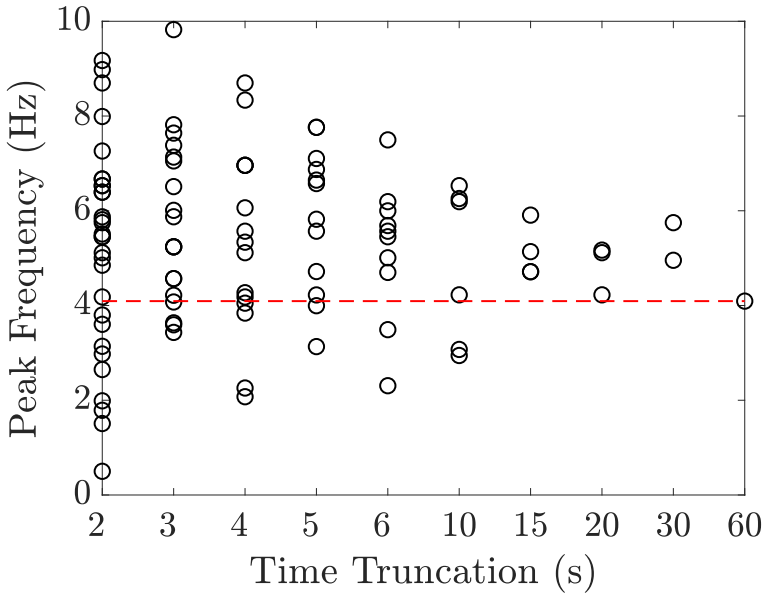

Figure 6.10: Peak frequencies found for varying time series lengths. The center red dashed line indicates the peak frequency found for the full one minute time series.

For each time truncation, a variance of peak frequencies is seen visually in Figure 6.10. This variance is calculated with respect to the different time truncations and displayed with other vertical locations at the same downstream distance ($x/D = 6$) from the porous disk in the boundary layer in Figure 6.11. The vertical positions are bottom tip height H_{BT}, hub height H_{Hub}, top tip height H_{TT}, one diameter above hub height H_{Hub+1D}, and one diameter above top tip height H_{TT+1D}. The variance of the peak frequency is obviously significant with small time series and decreases with increased time series length. Although these few data sets are only one minute in length, but this trend is expected to continue with increased length of time series. The plots presented here are representative of the entire measurement campaign. A longer discussion about the balance of length of time series and data acquisition accuracy is found in Chapter 4.

It is possible for the peak frequency plots in Section 6.3 to appear slightly different if the time series obtained per point location were a different length. Therefore it cannot be said for certain that the peak frequencies obtained for the meandering of the wake are absolute. That said, the following plots will give good estimates of the trends of wake meandering downstream of single objects and within an array with the current measurement campaign.

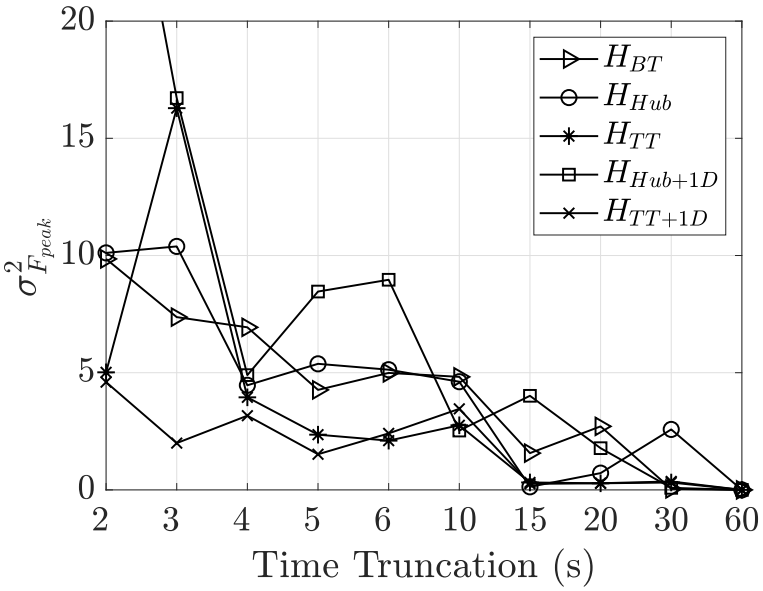

Figure 6.11: Variance of the peak frequency per time truncation at different vertical positions

6.2.5 Boundary Layer Structure Size

It was mentioned that larger than rotor atmospheric scales are responsible for the production of wake meandering. Figure 6.12 shows the structure size of the incoming boundary layer impinging the model turbine using data from this study at 62 m downstream of the turbulence management section using the local velocity and peak frequency to calculate an eddy size. Figure 6.12 is truncated at $y/D = 1.5$ in the wall normal direction to focus on the structures in the region of the model turbine rotor. The basic equation used to calculate a local structure size is

$$\delta_{structure} = U_{local}/F_{peak} \tag{6.5}$$

where $\delta_{structure}$ is the local structure size, U_{local} is the local velocity and F_{peak} is the peak frequency in the premultiplied spectra. Most of the incoming structures are larger than the rotor diameter and would therefore nominally have the ability to influence downstream wake dynamics. The red dashed line is the average of the incoming structure sizes and is equal to 2.3 meters. This large structure size indicates that there exist a dominant energy contribution to the flow at scales about 8 times larger than the rotor diameter. Currently, a data set comparing the in situ flow with the

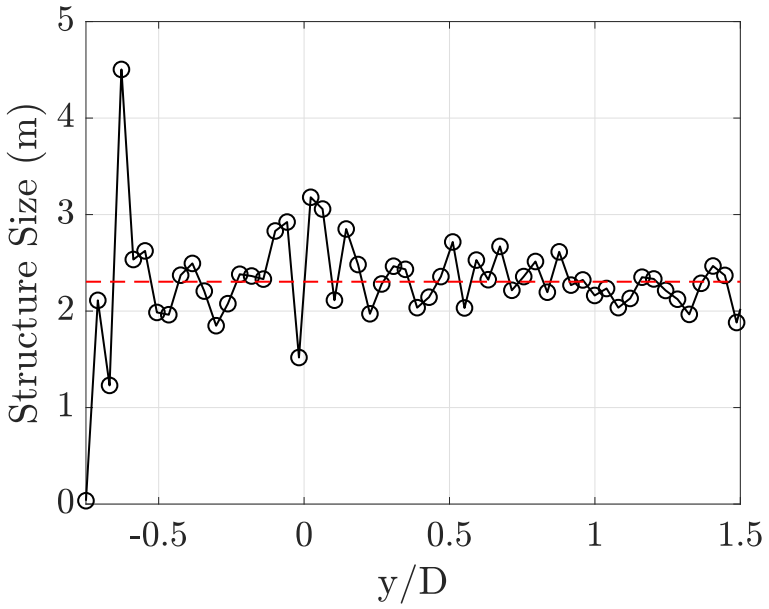

Figure 6.12: Structure size of the incoming boundary layer from the lowest measurement location 1 D above hub height obtained at 62 m downstream of the inlet. The region of interest is in roughly y/D =-0.5 to 0.5, the rotor location.

mean deficit excursion concurrently to calculate coherency in this setup does not exist, and so the incoming size can only be examined with single point statistics.

Figure 6.13 shows the calculated boundary layer structure size at various heights within the boundary layer, where $y/D = 0$ is turbine hub height, at five different downstream locations. Figure 6.14 show the peak frequency in the boundary layer at the same locations. These figures show the development of the boundary layer structure size with downstream distance. The data set used in Figures 6.13 and 6.14 is used in Vincenti et. al. 2013 [114]. These measurements are logarithmically spaced boundary layer profiles for the purpose of focusing on the physics near wall region as briefly discussed in Chapter 5. The Vincenti time series are obtained with a single wire hot wire at 10 kHz for 5 minutes per location for downstream distances of 4 m, 8 m, and 16 m, and 4 minutes per location for downstream distances 32 m, and 66 m. As mentioned, the Vincenti time series are focused on near wall boundary layer physics, and are obtained up to a wall normal position to the approximate boundary layer height height at that downstream location, so are a bit sparse for the region of interest for these studies. Figure 6.13 shows that structure size in the region

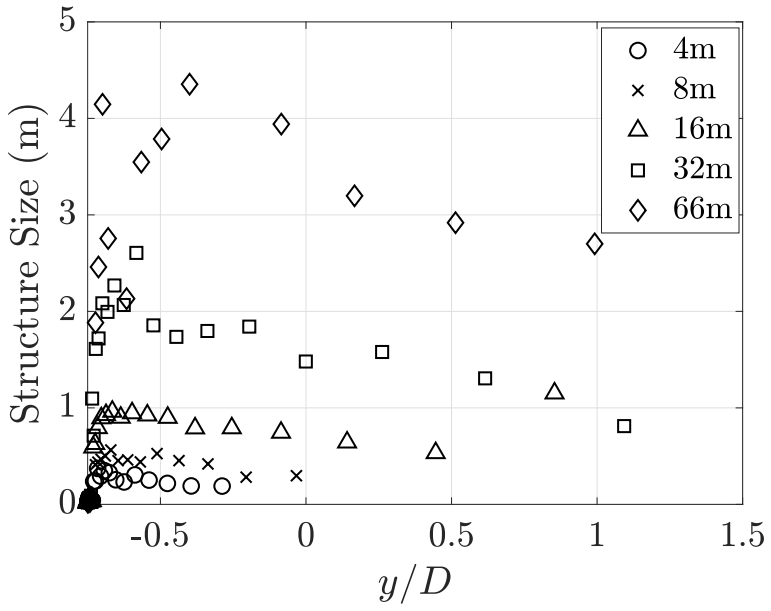

Figure 6.13: Structure size of the developing boundary layer at different downstream locations using data from Vincenti et. al. [114]. The region of interest is in roughly y/D =-0.5 to 0.5, the rotor location.

of interest increases with downstream distance. It can be noted that at 62 m downstream, the data from this thesis suggests a 2.4 m structure at top tip height as seen in Figure 6.12 while the Vincenti data at 66 m suggests a slightly smaller structure (2.9 m at top tip height), which is within reason. The data from Vincenti is sparse in the region of interest here.

The structure size is a function of both the peak frequency and the mean local velocity. At a fixed wall normal position, the local velocity decreases with increased distance downstream, which is understood when considering boundary layer similarity solutions prevalent in that field. Staying at a fixed wall normal position and advancing through the growing boundary layer can be seen as progressing slightly further into the boundary layer, closer to the near wall based on boundary layer height. Near wall structures tend to be larger than outer structures and so we see a decrease of peak frequencies with increasing downstream distance. It is apparent in Figure 6.13 that the peak frequency decreases at a faster rate than the velocity which produce larger structures with downstream development. There are clear frequency and structure size differences between 32 m and 66 m, which is basically the extent of the length of the array. Recall, the array extent spans 17

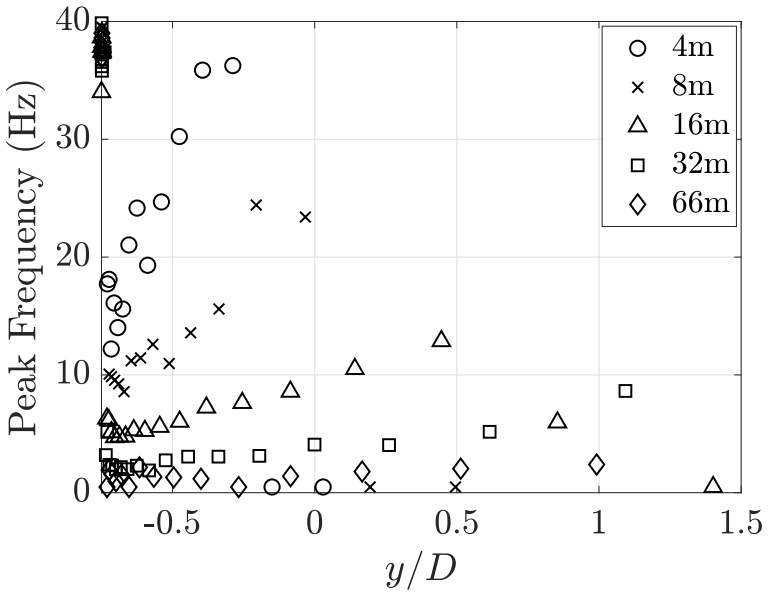

Figure 6.14: Peak frequencies of the developing boundary layer at different downstream locations using data from Vincenti et. al. [114]

rows of 2 m spaced turbines, or 34 m in development. However, the array measurements are for this set of experiments are located at the same location for each vertical profile and turbines are placed upstream of the measurement location to simulate traversing through the array. Figure 6.14 shows that the peak frequency in the region of interest (over the swept area of the turbine) does decrease slightly over that development fetch. The hub peak frequency decreases by ≈ 2.5 Hz, with the top tip location being about the same decrease. The bottom tip decrease in peak frequency is ≈ 1.5 Hz. The influence of the downstream evolution of peak frequency is discussed in Section 6.4.1.

6.3 Single turbine peak frequencies

The regression method discussed above is now applied to the data sets obtained downstream of the model turbines in the boundary layer. Both peak frequency and energy are extracted from the regression on the energy spectra. The evolution of peak frequencies are investigated here. The peak frequency regression is applied to for the energy spectra for all measured downstream locations for a porous disk (left) and a turbine (right) in the boundary layer at all vertical locations plotted as

a colormap in Figure 6.15. Vertical locations are represented in Figure 6.15 as a percentage of diameter of the object, where $y/D = 0$ is hub height. The color bar is cutoff at a frequency

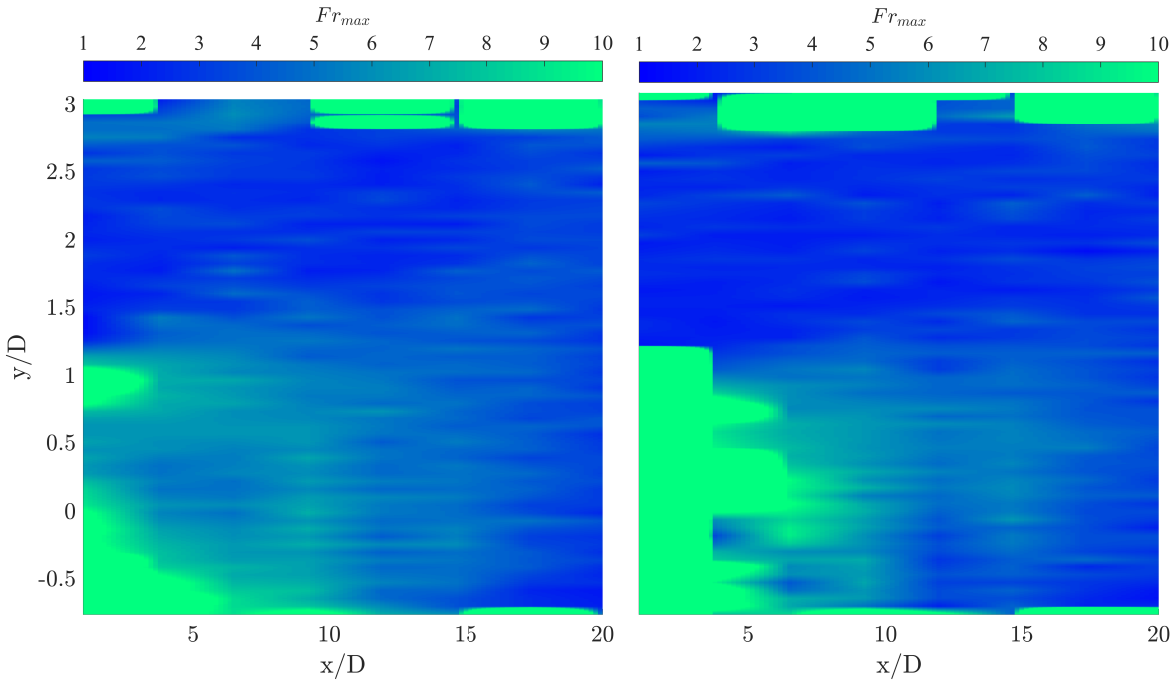

Figure 6.15: Maximum frequency surface plot in the wake of a porous disk (left) and a spinning turbine (right) in boundary layer flow

of 10 Hz to more easily detect variances in the peak frequencies in the region of interest. Near wake structures in the direct vicinity of the objects have higher peak frequencies, and these peaks decay with downstream position. Higher peak frequencies in the near wake are observed for the turbine which is influenced by the rotation of the blades. This type of investigation into the energy containing structures in the wake provides another view of the similarities of a drag matched porous disk and a rotating turbine in boundary layer flow at as close as 6 diameters downstream in the current configuration. Additional spurious high frequency peaks are seen at some of the highest vertical measurement positions indicative of the peak finding regression when encountering an overly flat spectra. The FPF has a free stream turbulence of $\approx 0.5\%$. The low free stream turbulence is synonymous with a low variance in the spectrum and therefore a flatter energy spectral density. There is no discernible peak in the energy spectrum at these free stream locations. In this region,

premultiplying the spectrum is just an amplification of noise. The spectra far away from any object have particularly low energy in the lower frequencies. This type of lower energy at larger length scales is indicative of small scale turbulence with no large structures, as expected in the free stream.

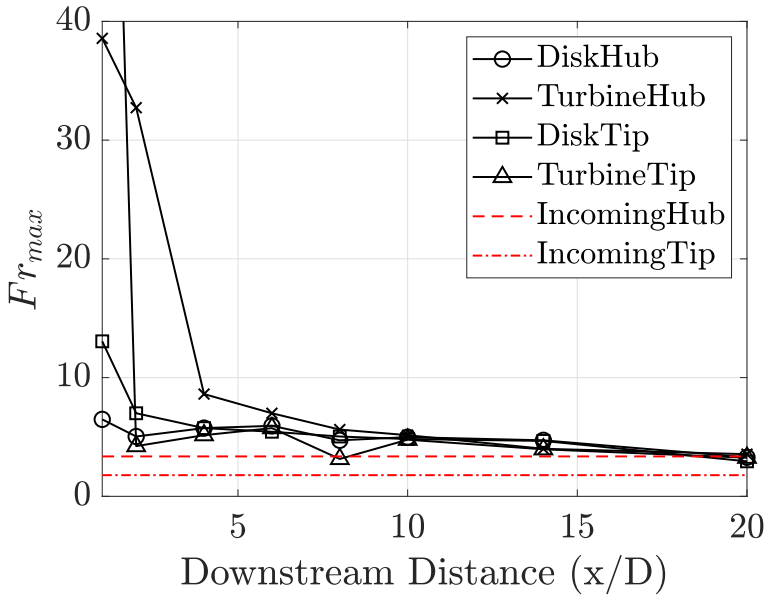

Figure 6.16: Maximum frequency per downstream position for Hub and Tip height for single object in boundary layer pulled from energy spectra

In Figure 6.16 the hub and tip height measurements from the disk and the rotating turbine wake are extracted and plotted with respect to downstream distance. The hub height and top tip height locations are thought to be the most influenced by the non periodic movement of the velocity deficit downstream of the object. Also included are the maximum energy frequencies obtained from the inlet at hub height and top tip height for reference. Initially the turbine peak frequency from the energy spectrum is very high at both hub height and top tip height due to the blade passage frequency which affects the near wake. Just past near wake in the $x/D = 6$ downstream regime the Strouhal number is calculated to be ≈ 0.25, similar to measurements made by Coudou [38]. Further downstream, the peaks trend towards lower frequencies and eventually return to that of incoming peak frequencies at hub and tip locations very far downstream. It is noted that the near wake of the disk has significantly lower peak frequencies in the near wake at both vertical locations.

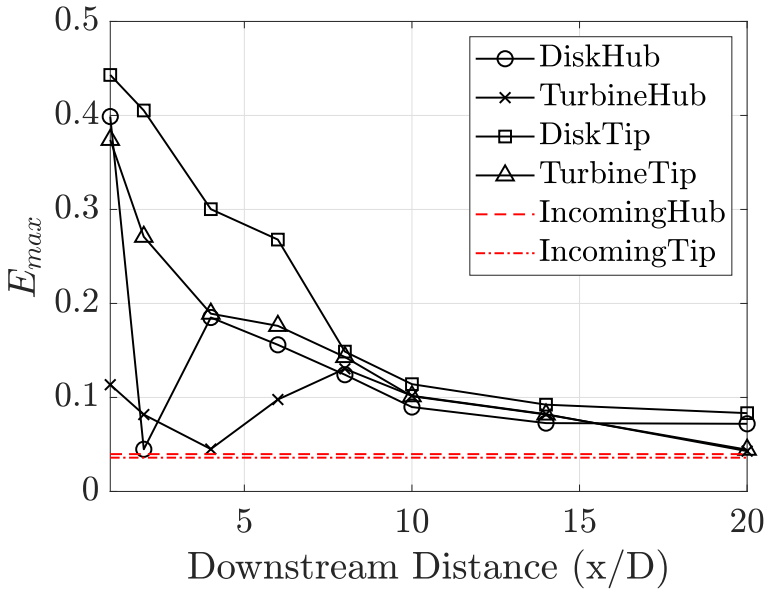

Figure 6.17: Maximum energy in premultiplied spectra per downstream position for Hub and Tip height for single objects in boundary layer

The peak energy content obtained from the premultiplied spectra of the objects at hub height and top tip height is obtained and shown in Figure 6.17. The peak energy for both objects starts high in the near wake and with progression downstream decays towards the incoming energy levels. The wake of a porous disk vs. a rotating turbine in a mean shear has been validated as similar in the literature, including these objects [34]. It is seen here that the objects also become very similar in peak frequency and energy in spectra with increased downstream distance. With this knowledge, the methods presented here could be used as another confirmation of the wake similarities of porous disks and rotating model turbines in shear flows at a certain downstream distance.

6.4 Turbine Array

An array comprised mainly of porous disks is built up and the tip vortices and wake swirl is reintroduced into the flow by placement of a 3×3 array of miniature 0.25 m diameter rotating model turbines. Vertical single hot wire profiles are taken at centerline of the 5 column × 19 row array behind the 3rd row of rotating turbines. Measurements taken at a downstream locations of $x/D = 2$ and $x/D = 4$. Two stream wise spacings are used, 8 diameter and 10 diameter. Two

dummy rows are put in place behind the measurement location as to not affect the pressure gradient due to a sudden decrease in blockage.

6.4.1 Array wake meandering

A plot of maximum frequency per downstream position in an array of porous disks and turbines with profiles taken every 5 rows at two downstream locations and two array spacings is shown in Figure 6.18. The abscissa is labeled 'R3,x/D =2' which contains two parts. The first, 'R3' is

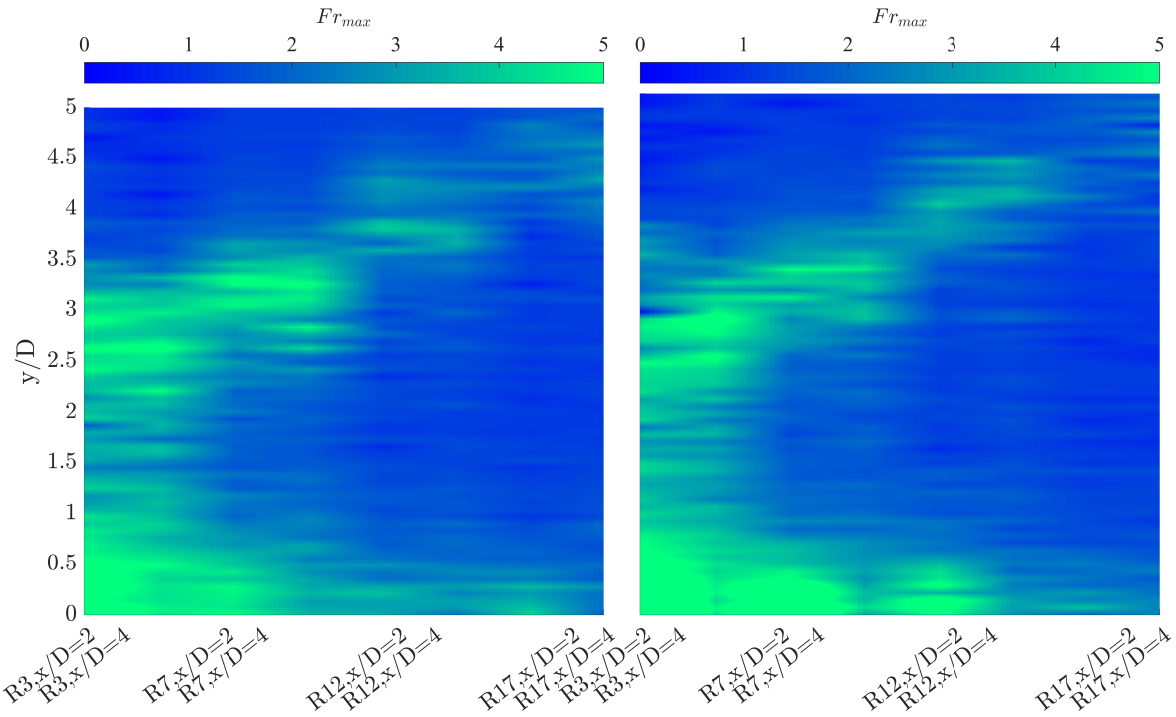

Figure 6.18: Maximum frequency per downstream position for an array of turbines in a boundary layer at two spacings. 8D (left) and 10D (right)

the number of turbine rows the measurement takes place downstream of and the 'x/D =2' is the measurement location directly downstream of the turbine, either 2 or 4 diameters (0.5 m or 1 m respectively). The measurements are taken with two array spacings, 8 diameters and 10 diameters. The ordinate is labeled as 'y/D' indicating a percentage of object diameter where 0 indicated the hub height. Through the extent of the array, higher frequencies are observed in a streak moving up and right which follow the internal array boundary layer growth.

Extracted from the surface plot is the top tip height and hub height maximum frequencies and energies for the $8D$ and $10D$ spacing for a single downstream measurement, either '$x/D = 2$' or '$x/D = 4$' and shown in Figures 6.19 and 6.20. The red dashed lines indicate the maximum energy in the spectra of the inlet at hub and tip locations.

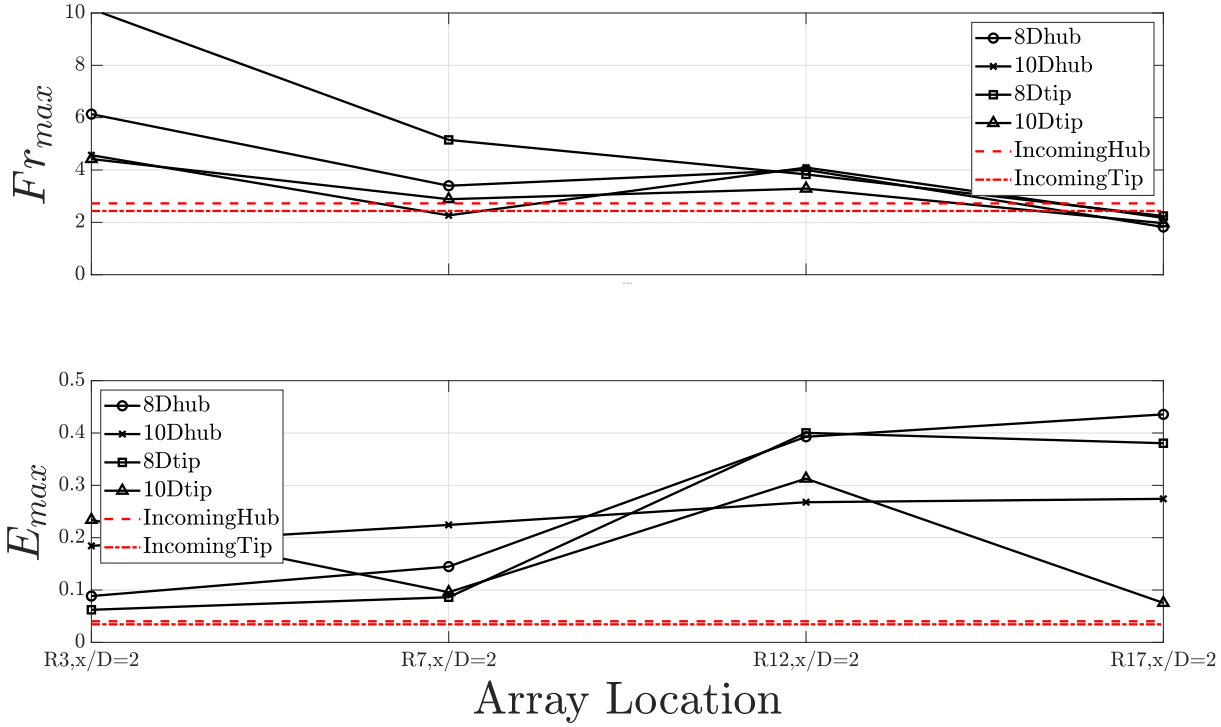

Figure 6.19: Maximum frequency per downstream position for Hub and Tip height for an array of turbines in a boundary layer measured at a downstream distance behind the indicated turbine row of $x/D = 2$

The maximum frequency occurs at a downstream location of $x/D = 2$ for the 8 D spacing at top tip height. It's common for higher energy to exist in the tip region due to the tip vortex shedding phenomenon. This does not explain the lower maximum frequency value for the 10 D spacing arrangement. Moving downstream and increasing the number of turbines in the array, a downward trend in maximum frequencies is seen. Also plotted on Figure 6.19 is the incoming hub and tip locations within the boundary layer. It is shown that with an increased number of turbines, the most energetic structures in the flow are no longer the maximum frequency peaks in the incoming boundary layer. Moving far downstream in an array destroys the incoming large

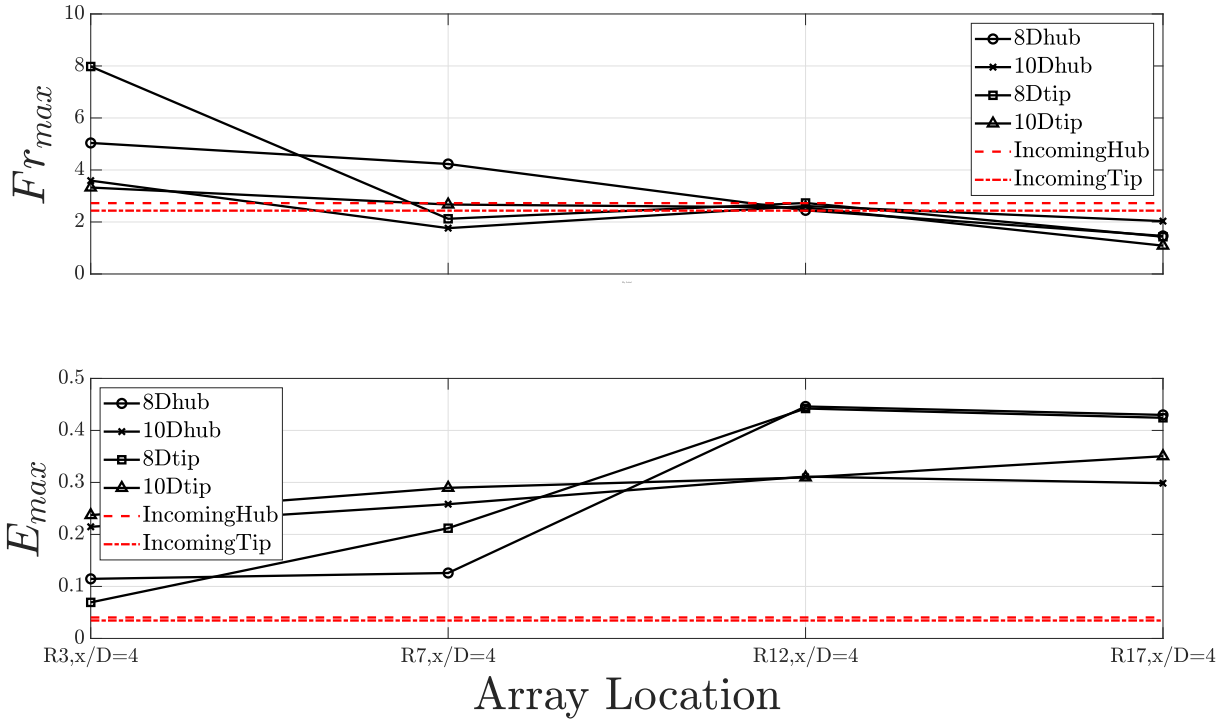

Figure 6.20: Maximum frequency per downstream position for Hub and Tip height for an array of turbines in a boundary layer measured at a downstream distance behind the indicated turbine row of $x/D = 4$

scale eddies and slower, larger structures dominate the flow. These longer structures could be the natural resonance of the array spacing itself.

To see if the array could have a coalescing meander, a few different characteristic velocities can be applied.

- The tunnel set freestream speed of 6.7 m/s.
- The incoming hub velocity which is about 5.7 m/s.
- The hub height speed 2 diameters upstream of each turbine which is 3.8 m/s on average.

The array has a set configuration and is spaced at either 8 D or 10 D, which is 2 m and 2.5 m respectively. This would mean that the dominant array configuration based frequency would range from 3.35 Hz to 1.52 Hz. Referencing Figure 6.19 and 6.20 again, far downstream the maximum frequency is about 1 - 2 Hz meaning the internal array hub speed is most appropriate to calculate array resonance. By 17 rows downstream, the meandering has arranged itself in a very large

scale motion with a dominant frequency lower than the large scale atmospheric turbulence in the approaching flow. The fully developed flow has a peak frequency dominated by array spacing.

Unlike the single objects in Figure 6.17, the maximum energy in the array is shown to increase with downstream distance. This shows that not only does the array contain large scale structures with frequencies slower than the incoming profile, but there are energy increases associated with the structures formed by turbine spacing.

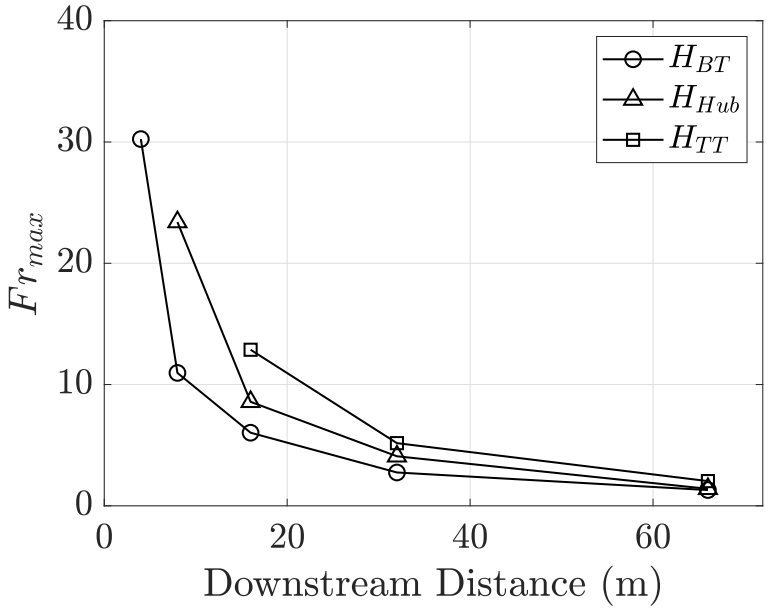

Figure 6.21: Maximum frequency per downstream location for approximate Bottom Tip, Hub and Top Tip height (within $y/D = \pm 0.1$) from Vincenti et. al. [114]

It should be noted that due to the large extent of the array, the peak frequency of the incoming boundary layer flow would also change as discussed in Section 6.2.5. Figure 6.21 shows the change in peak frequency with downstream position obtained from the data of Vincenti et. al. [114]. Due to the logarithmic spacing of the data from Vincenti, the wall normal locations used here are within $y/D = \pm 0.1$ of bottom tip, hub height and top tip. Additionally, the data was obtained up to the boundary layer height, so some information may not exist at the locations of interest here. It can be seen that the peak frequencies decrease as a function of downstream distance for the wall normal locations chosen. Peak frequency also decreases with decreased distance to the wall as discussed in 6.2.5. So, it is possible that the flow within the array also decreases in peak frequency and the

spacing of the turbines and flow velocity exact combination just happens to match by coincidence. Measuring the peak frequencies at the first location, behind only three rows of turbines in Figures 6.19 and 6.20, it is found that the maximum frequencies are much unlike the incoming flow, as the array creates a large disturbance. Although a coincidence is possible, it seems unlikely, as the array acts as a very large disturbance in the flow. It is argued here that the array creates a large enough disturbance in the flow that any modification in frequency over the extent of the array (see Section 6.2.5) should be attributed to the influence of the structures modifying the flow and not the natural development of the boundary layer. Self organization of flow structures is the only way for this decrease in peak frequency to be observed. As the measurement location isn't changing, the new influence of the upstream placed turbines must be the cause of the change in peak frequency.

The understanding how deep array meandering behaves will allow the optimization of the balance between turbine loading and maintenance costs on one side, and overall energy yield on the other.

6.5 Scale Decomposition

In the wake of an object, defined as the momentum deficit, there are increased turbulence levels compared to the incoming boundary layer flow. We can look at the velocity time series as a superpositioning of large fluctuations and small fluctuations and separate them accordingly. We find that the slower turnover, larger scale structures modulate the small structures. This section applies some of the methodologies of the work of Mathis, Hutchins and Marusic (2009) [68]. The motion of the wake is correlated with excursions from the mean that amplify the smaller turnovers. If the wake meanders into and out of the sensor location, it is expected to also see some small scale modulation correlated with the passage of the larger meandering structures. Knowing where increased turbulence is projected to be in the incoming flow for downstream turbines will help understanding of how to tune and operate arrays.

6.5.1 Filtering large and small structures

A butterworth filter with 0.1 dB passband ripple and a stop band attenuation of 50 dB was designed to separate the large motions and the small motions at an appropriate location, a stop band frequency of 20 Hz. This stop band frequency is higher than would be expected for the meandering motion (recall maximum frequencies in the peak of the spectrum of roughly 1-10 Hz), but certainly much slower than the turn over time for small eddies in the turbulence regime. Figure 6.22 shows the effectiveness of the filter on the spectra. The raw timeseries spectrum is shown in

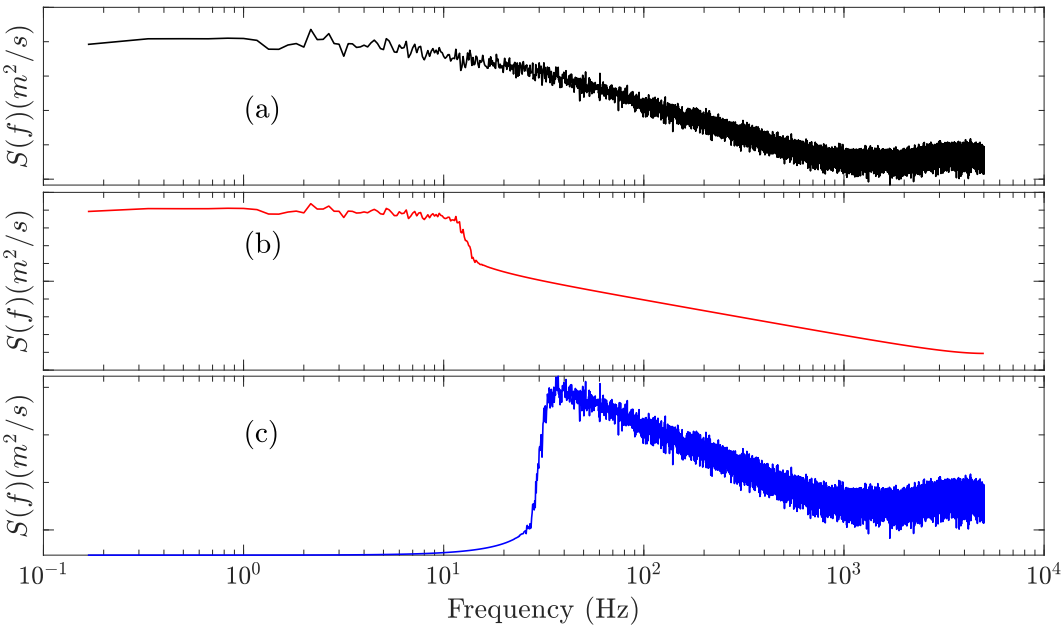

Figure 6.22: Spectra showing the high pass and low pass filters used to define the scale separation in the wake. a)time series, b)low pass filter, c)high pass filter

(a) of Figure 6.22. The low pass filter in (b) only keeps the large fluctuations in the flow and the high pass filter with the same filter criteria in (c) only keeps the turbulence.

The mean removed raw section of time series velocity at top tip height at 1 D behind the disk in the boundary layer has been separated into two parts at this cutoff and shown in Figure 6.23. As in Figure 6.22, (a) is the raw time series, (b) is the low pass filtered larger structures in the flow and (c) is the small scale structures in Figure 6.23. This truncated section of the flow is broken up by vertical dashed lines to indicate sections that are prolonged regions of positive and

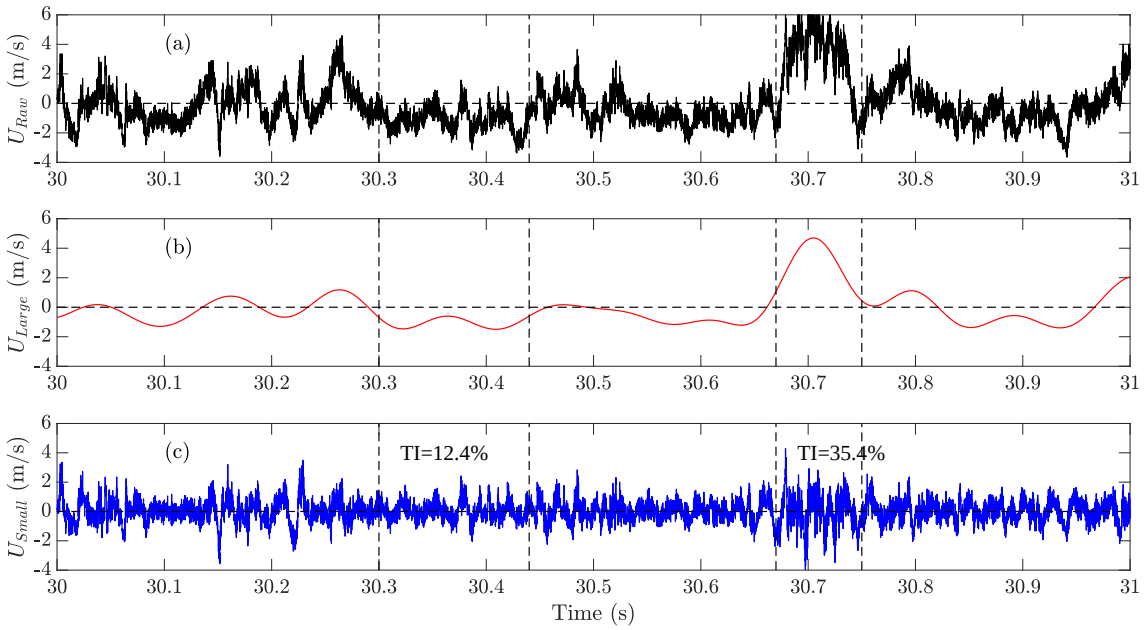

Figure 6.23: Scale separation between large and small structures of 1 diameter downstream of a disk in the boundary layer at top tip height. a)time series, b)low pass filter, c)high pass filter

negative fluctuation from the mean. A positive excursion would represent a higher velocity motion containing a packet of information and a negative excursion would represent a slower motion. The positive excursion from the mean amplitude modulates the small scales as seen in (c) of Figure 6.23. This same trend occurs for multiple time series truncations not shown here. When the large scale fluctuations are positive (U_{Large}), the turbulence intensity, ie. the amplitude of the small scale fluctuations (U_{Small}) is also larger. The opposite is true for negative large scale fluctuations, also shown by turbulence intensity quantity on Figure 6.23. With this visual observation in mind, we move on to a more formal way of conducting this large scale modulation analysis of small scale amplitudes.

6.5.2 The Hilbert Transform

The Hilbert transform is a phase shifted convolution integral and can be defined as

$$H(t) = \frac{1}{\pi} P \int_{-\infty}^{+\infty} \frac{x(\tau)}{t-\tau} d\tau \tag{6.6}$$

See [93] for a more complete definition. The modulus, or envelope, of the analytic signal can be written

$$A(t) = \sqrt{x^2(t) + H^2(t)} \tag{6.7}$$

In Figure 6.24 an example usage of the Hilbert transform is shown. Plot (a) shows the carrier

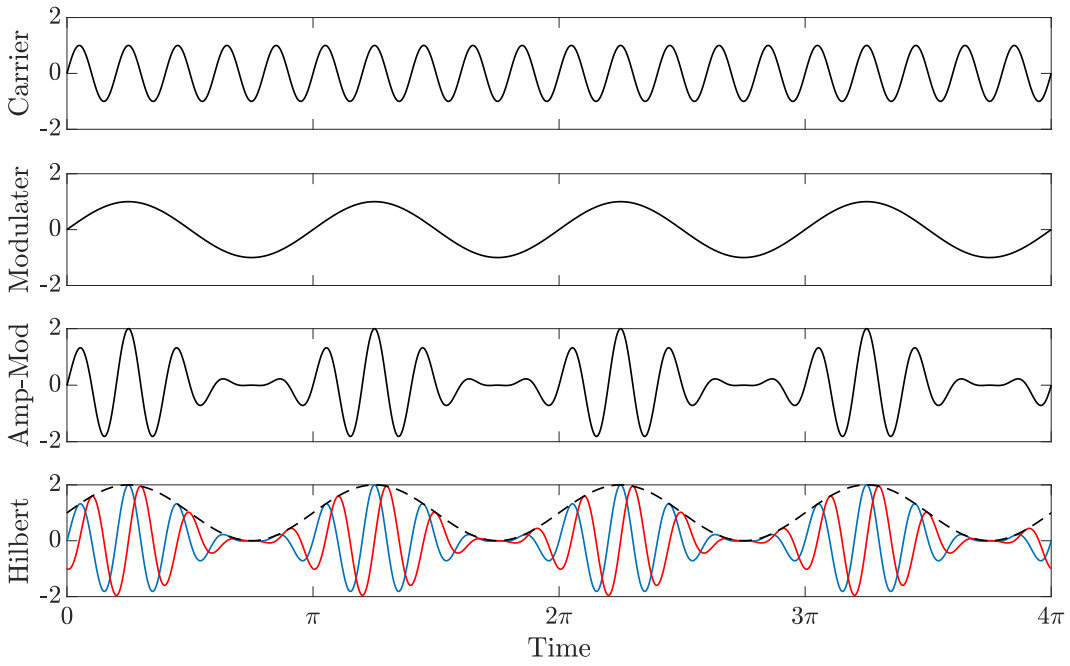

Figure 6.24: Example usage of the Hilbert Transform

wave, a simple sinusoid, $c(t) = sin(10t)$. Plot (b) is the modulating wave, $m(t) = sin(2t)$. Plot (c) shows the amplitude modulated wave shifted by an offset $B = 1$. Finally, the real part of the Hilbert transform is plotted in (d) which returns the amplitude modified signal $u(t)$ in solid blue, and the imaginary part of the Hilbert transform returns the $u(t)$ phase shifted by $\pi/2$ shown in solid red.

$$u(t) = (B + m) \cdot c(t) \tag{6.8}$$

The envelope, calculated by Equation 6.7, is shown by the dotted black line. In this case, because the modulating signal is a pure sinusoid, the envelope returns all positive valued modulating wave time series.

The Hilbert transform may be useful when using an analog signal obtained from a real data set as seen in Figure 6.25. Plot (a) of Figure 6.25 shows the raw timeseries of velocity at 1 diameter

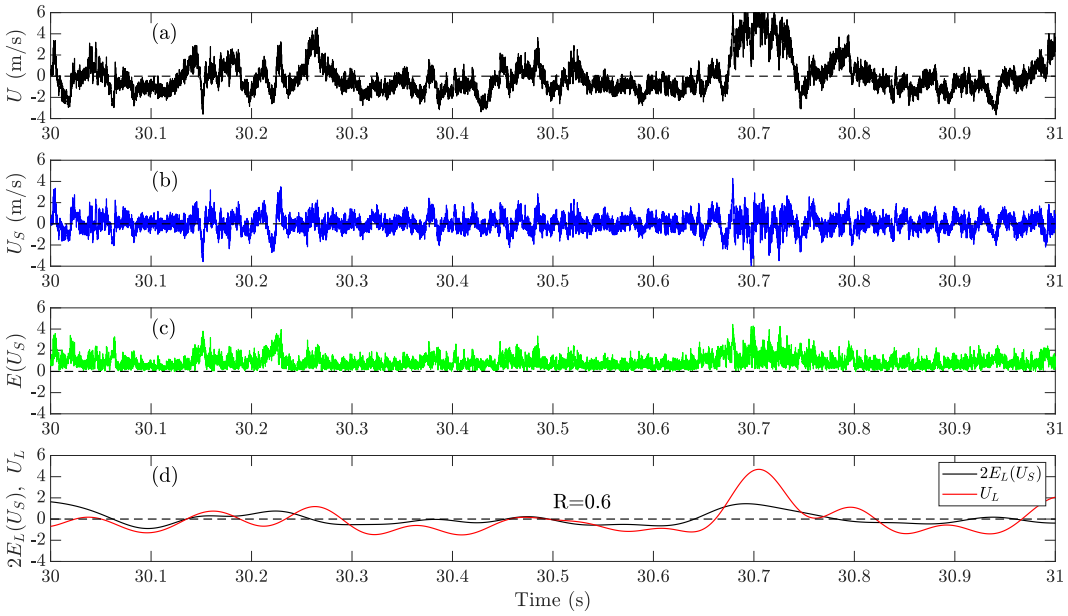

Figure 6.25: Usage of the Hilbert Transform at 1 diameter downstream of a disk in the boundary layer at top tip height for an arbitrary time range

downstream of a disk in the boundary layer at top tip height for an arbitrary time range. Using the filters discussed in Section 6.5.1 the small scale structures (U_S) are separated from the larger wake meandering and plotted in (b). Plot (c) shows the Envelope of the small scale structures ($E(U_S)$) calculated by taking the Hilbert transform of U_S. In order to confirm a relationship between wake meandering and small scale structure amplification, the high pass filtered data was analyzed using the Hilbert transform. The envelope created by use of the Hilbert transform now represents any modulating affect on the signal. As in the example in Figure 6.24, it would be nice if the envelope only contained the modulating signal. However, since the wake is comprised of multiple scale oscillations as with any turbulent signal, the Hilbert transform will capture this broad range of amplitudes and wavelengths in the carrier signal. The effect of the small scale variances is removed by filtering the envelope with the same cutoff as applied to the raw time series to obtain the large scale structures which is now denoted as $E_L(U_S)$. The final plot (d) in Figure 6.25 shows the low pass filtered time series U_L and the low pass filtered envelope of the small structures, $E_L(U_S)$.

The low pass filtered envelope of the small structures is multiplied by 2 for convenience to show a similar amplitude to the low pass filtered time series.

To calculate a quantitative correlation between U_L and $E_L(U_S)$, we define a correlation coefficient listed as R in Figure 6.25 for that arbitrary truncated time range. The correlation coefficient is defined as the covariance divided by the product of the standard deviations

$$R = \frac{\overline{U_L E_L(U_S)}}{\sqrt{\overline{U_L^2}}\sqrt{\overline{E_L(U_S)^2}}} \tag{6.9}$$

For a comparison, Hutchins and Marusic 2009 show a representative plot with a correlation coefficient of $R = 0.33$ for the low pass filtered Hilbert transform in comparison with the large scale structures in boundary layer flow [68]. This correlation coefficient gives a quantitative value of the similarity between the large scale structures and the amplitude modulation of the small scale structures by the meandering, as calculated by the Hilbert transform envelope.

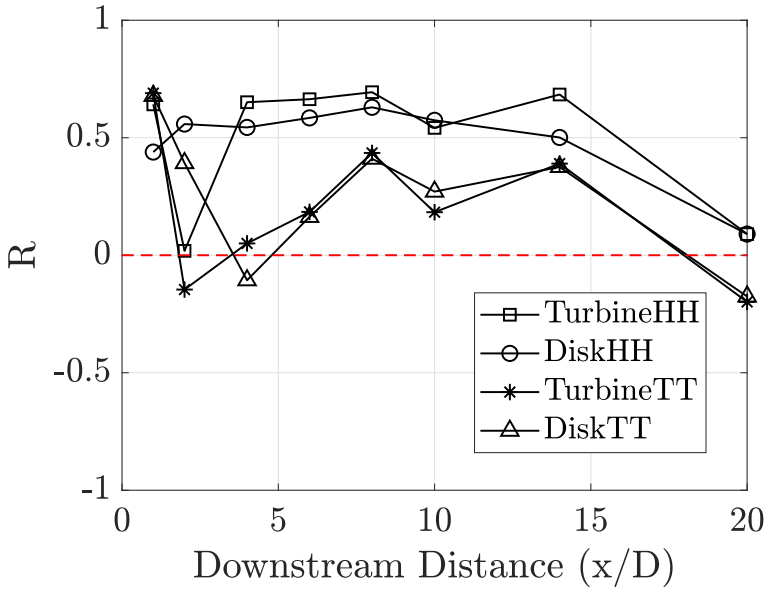

Figure 6.26: Correlation coefficient for top tip and hub height of the single disk and single turbine at downstream locations.

Figure 6.26 shows the correlation coefficient for the turbine and the disk at top tip and hub height for the whole time series measured in the boundary layer at the 8 downstream locations.

Calculating R values for near and far downstream distances for the whole time series it seems that the near wake has generally greater correlation than the far wake for hub height values. Far downstream, the wake mixing increases with downstream distance and decreases correlation. As shown in Figure 6.16, the meandering signature also decays. The correlation is larger within the center of the wake due to the large scale motions and within the wake the turbulence is higher. At top tip of the wake of the model turbines, much less time is spent within the wake at the stationary measurement location as the wake meanders in three dimensional space. When the location is not within the wake, the correlation drops as less turbulence is present. This could be thought of as the same reasoning why further downstream R decreases for all location as the wake recovery decreases turbulence and larger scale motions.

6.5.3 Synthetic Time Series

This section discusses the verification of the correlation between small scale amplification and large scale motions by usage of a synthetic data set. A synthetic signal can be constructed from the an original time series' power spectral density. The power spectral density is converted to amplitudes, then scrambled by applying a random phase between 0 and 2π for each frequency bin. The inverse Fourier transform is applied to produce a new time series and only the real component is plotted. As an example, a time series is used from hub height at 6 diameters downstream of the turbine in boundary layer flow and the two time series, original (left) and synthetic (right) are plotted in Figure 6.27. The power spectral density is also calculated for comparison in Figure 6.27 plotted with 100 DoF. Note that the power spectral density of the synthetic signal should be identical to the power spectral density of the original signal. The synthetic time series has has been created from the frequency information of a real time series, neglecting realistic phase information.

The two time series, original and synthetic, undergo the low pass and high pass filter operations. Large scale (top) and small scale (bottom) filtering is shown in Figure 6.28 of the original time series (left) and the synthetic time series (right). We can see some evidence in this one second section examined here of the small scale amplitude modulation of the small scales for the original

time series. The positive excursions from the mean have a visual impact on the small scales increase in variance. From cursory inspection, the synthetic time series does not appear to have the same amplitude modulation. The randomization of the phases in the power spectral density that produced the time series destroyed the correlations of the memory of the flow removing the effect that large scales have on small scales in the in situ data.

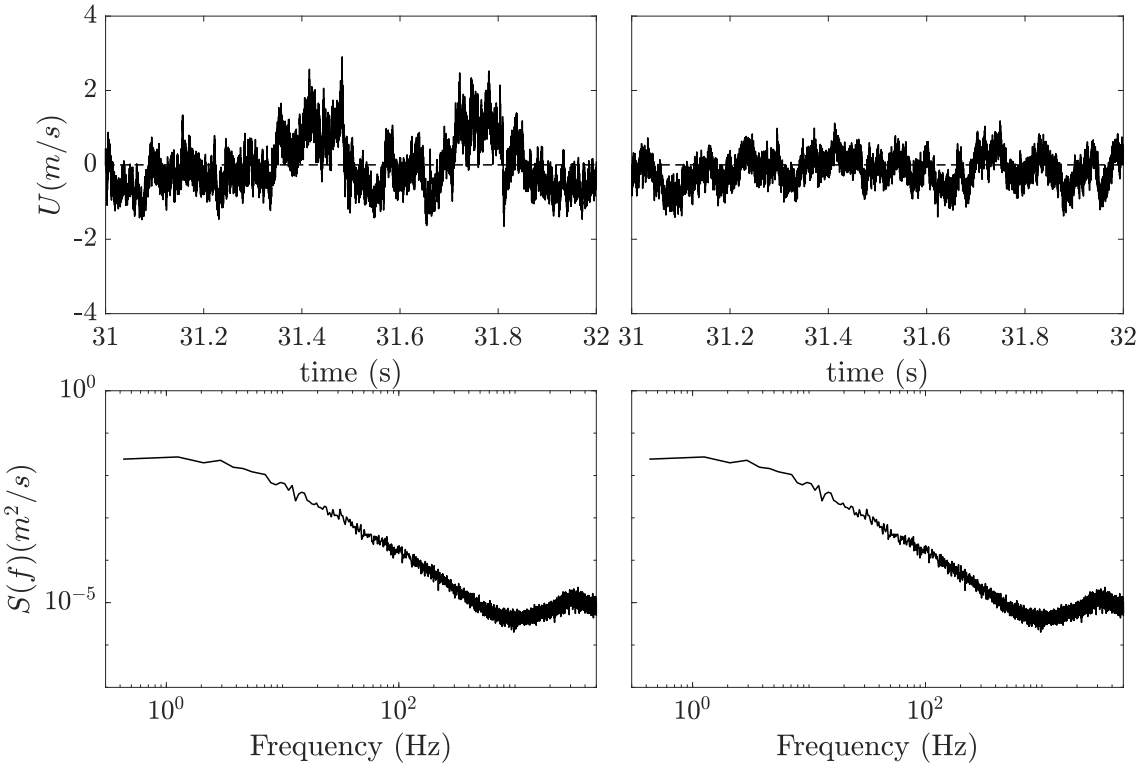

Figure 6.27: Time series and power spectral density from real data (left) and synthetic time series and power spectral density (right)

To confirm this visual inspection, the analysis is extended to full signals across all wall normal heights and the correlation coefficient is plotted in Figure 6.29 and 6.30. Real data is on the left and synthetic data is on the right. Figure 6.29 is data downstream of the turbine and Figure 6.30 is data downstream of the disk. Synthetic time series were reproduced based on the phase scrambled power spectral density of each measurement location. Immediately obvious is the lack of correlation between large and small scales at any position with the synthetic data. The original signals show comparatively high correlation with some degree of wall normal dependency. Similar

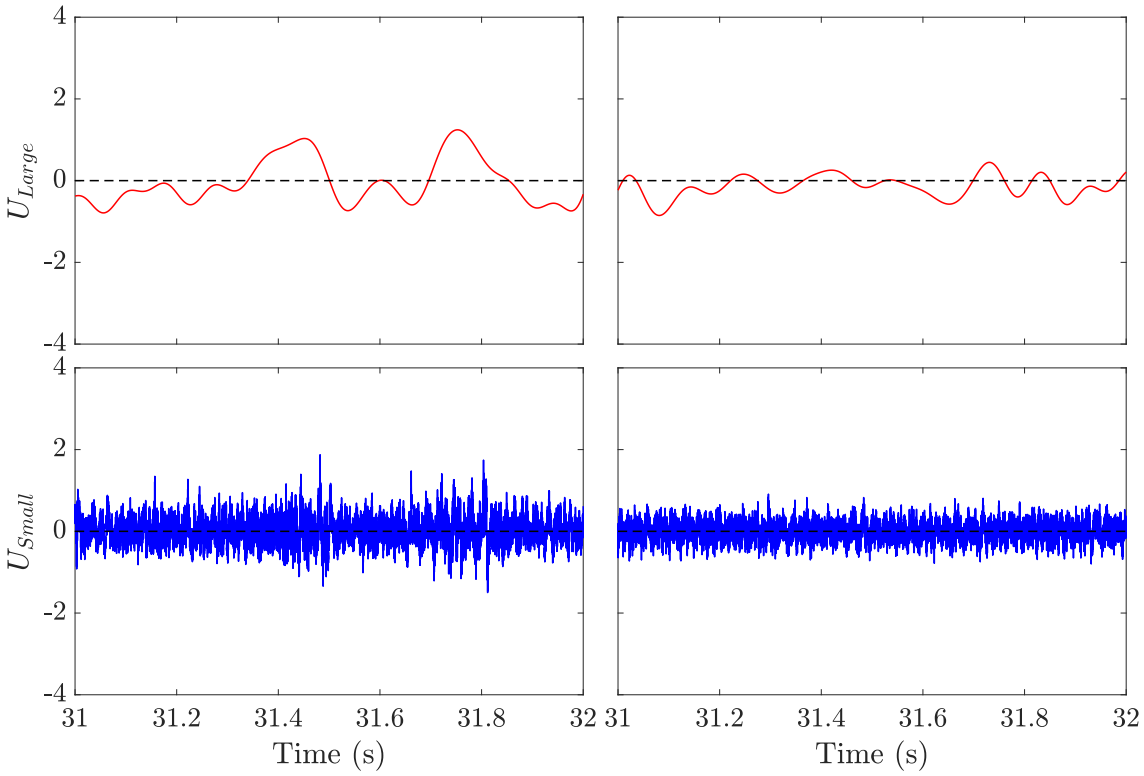

Figure 6.28: Large scale (top) and small scale (bottom) filtered time series from real data (left) and synthetic time series (right)

trends are noted between the two sets of correlation coefficients for the real data. In the near wake, the correlation seems to vary a high degree. With increased downstream distance, the wall normal correlation exhibits a relatively similar trend, with higher correlation close to the wall and directly behind the turbine. With increased height, the correlation descends steeply, and this steep descent can be seen to shift to higher locations above the turbine with increased downstream distance. This shift in the first steep descent most likely indicates the growth of the wake with downstream distance and that within the wake the amplitude modulation of small scales is influenced by larger scales. Outside of the wake growth above the turbine and at the end of the sharp descent in correlation value, R is nearly zero, even experiencing a large peak correlation reversal for both turbine models at the maximum downstream distance measured of 20 diameters. This reversal is in fact also seen in pure boundary layer data by Hutchins and Marusic [68].

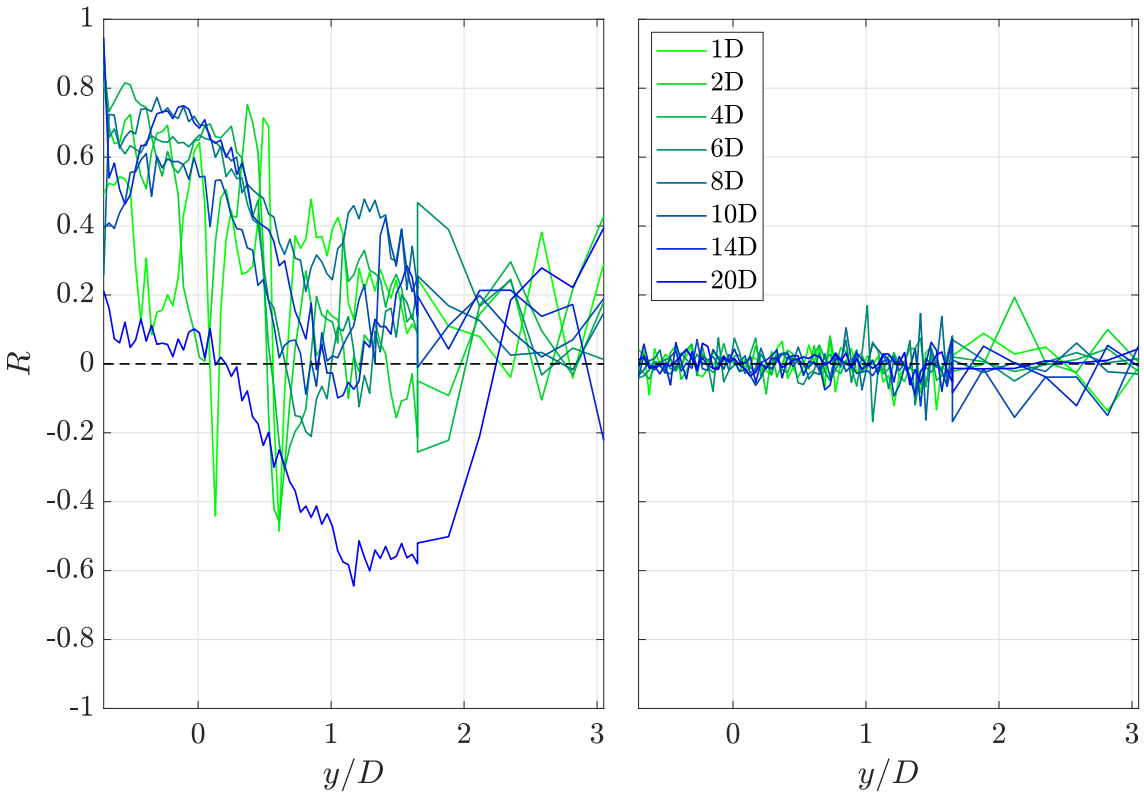

Figure 6.29: Correlation Coefficient R calculated at all available wall normal positions and downstream locations for real data downstream of the turbine (left) and synthetic time series (right)

It is shown here that the large scale energy is superimposed as amplitude modulations to the small scale fluctuations. In areas with large scale motions, like within a meandering wake, the small scale fluctuating component is more energetic. In non-wake regions, the lack of large motions, as indicative of a relatively flat spectra, a reversal of the trend is found. In the freestream region, the small scale fluctuations become independent of large scale motions and the correlation coefficient is decreased. The inclusion of a synthetic time series for comparison, with randomized phase, indicates the truth of the correlations from the real data sets.

6.6 Summary

A model turbine and a drag matched porous disk were placed in a boundary layer flow to investigate the meandering behavior of the wake with single point statistics. Using a regression on the premultiplied spectra, we find that the maximum frequency in the wake of the single objects

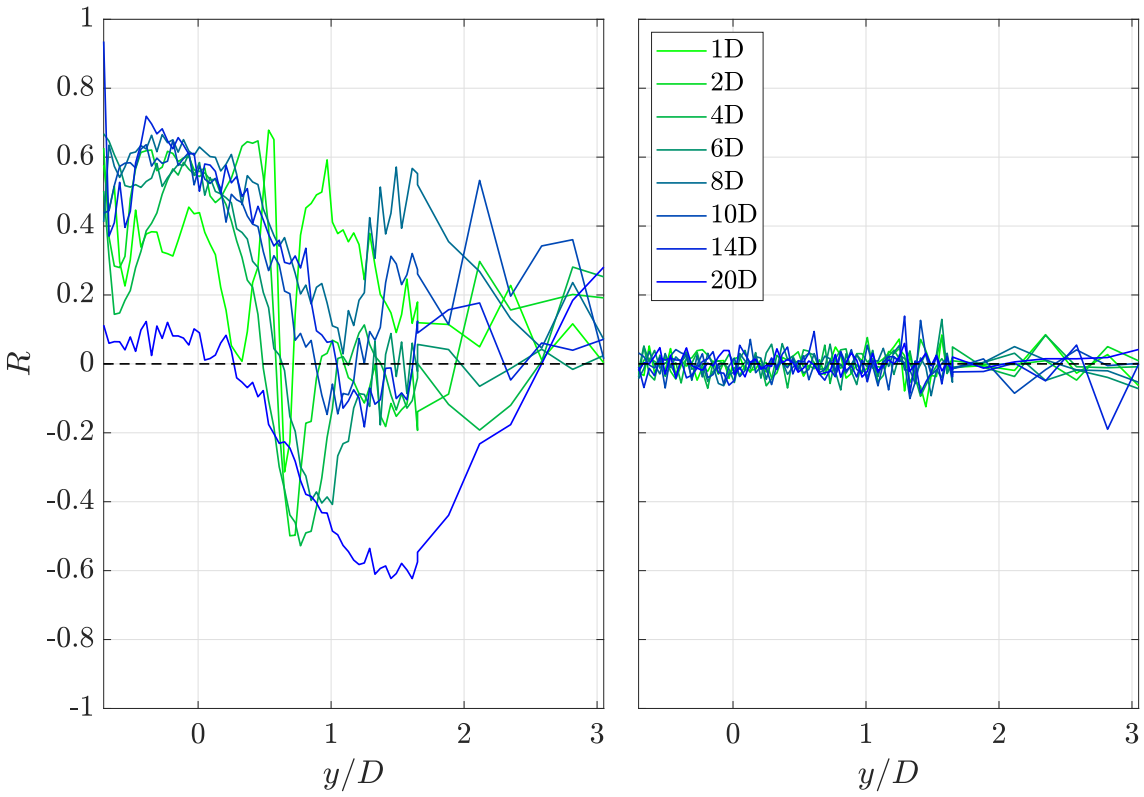

Figure 6.30: Correlation Coefficient R calculated at all available wall normal positions and downstream locations for real data downstream of the disk (left) and synthetic time series (right)

decays back to inlet conditions with measurements 20 diameters downstream. The energy of the premultiplied spectra also decays with increased downstream distance. This type of analysis could be another methodology used to compare porous disks and rotating model turbines in shear flows. Positioning the turbines and disks together in an array, it is shown that far downstream in the fully developed region of flow, the wakes organize into larger structures that depend on the spacing of the array and internal farm velocity.

A scale decomposition of the velocity signal was performed in conjunction with the Hilbert transform to separate large and small scale motions. It is shown that large scale oscillations amplitude modulate the small scale energy in the wake. The small scale motions were then low pass filtered to uncover modulation from low frequency large scale structures in the flow. A correlation coefficient was applied to the relation between large and small scales. It was found that within

the wake of the model turbines the correlation was high, while outside the wake the coefficient decreases.

Large scale meandering motions play an important role in the wake of turbines and turbine arrays in boundary layer flows. The dominant scales of the flow are shown to depend on turbine spacing, and this knowledge can be used when siting an array to take advantage of these flow dynamics. Similarly, if meandering scales are known, turbines can be passively tuned to take advantage of the motion of the wake, or avoid blade scales that interact negatively with the meandering fluctuations to avoid increased rotor fatigue.

CHAPTER 7

SUMMARY AND CONCLUSIONS

Two experimental scale wind turbine models were utilized to conduct studies of boundary layer–wake interactions of single models and the fluid dynamics within a large wind farm. Data for the turbine array has been presented for a case that has a realistic spacing of turbines when compared to an offshore array.

Mean velocity data was obtained in a 19-row, 5-column wind turbine array in a boundary layer wind tunnel and confirms the existence of the fully developed wind turbine array boundary layer. The array was built up with 0.25 m diameter porous disks with a hub height placed at $0.75D$ from the floor. The disks were drag matched with rotating model turbines which are 1:500 scale models of NREL's offshore reference turbine. Porous disks are the physical representation of the CFD modeler actuator disk concept. The array was positioned in a model atmospheric boundary layer type flow and compared with ASCE standards. The flow was thickened with spires at the entrance of the test section. Velocity data was obtained in vertical profiles of 24 wall-normal locations each at center line of the tunnel and array at downstream locations of $x/D = 6$ from the first 17 rows of model turbines. Velocity profiles normalized by free stream velocity show that momentum is lost into the array with progression downstream. When using a boundary layer height outer normalization the flow exhibits self similar behavior as near as four rows downstream and the profiles collapse well. From the outer normalization, it could be incorrectly assumed that the flow reaches a statistically stationary state with respect to downstream evolution as quickly as 4 rows downstream. Using a coefficient of determination method with the velocity profile of row 16 being the model, three normalizations are considered to quantitatively asses the determination of the fully developed condition. Within a narrow band of the flow, the equilibrium region, after 12 rows it is found that the coefficient of determination peaks and levels off. This statistical stationarity can

also be called the infinite wind farm condition. The confirmation of the fully developed condition has not previously been observed in physical studies. The experimental array is shown to become fully developed in the mean at row 12.

This study has provided knowledge on the complex developing flow of a wind turbine array boundary layer, who's origin wall normal location remains fixed in space while the external atmospheric boundary layer continues to develop. Knowledge of this fully developed state existing in a physical experiment of porous disks for a given configuration will help us better understand the balance of power extraction of the turbines with maintained atmospheric boundary layer growth above the canopy of the array. This benchmark data set will help the fundamental understanding of wind turbine array limits in a defined set of conditions. This work used porous disks, which are the physical approximation of the computational actuator disk models, which should be helpful for numericists to calibrate in situ wake boundary layer behavior, and thusly bulk power production in models. The data set is publicly available as discussed in Appendix A.

An expanded uncertainty analysis via Taylor Series Method was conducted to draw attention to the challenges and cautions that should be taken when using an open to atmosphere type facility. The typical standard uncertainty analysis for the first order moment of a turbulent flow, velocity, only considers the local turbulence and number of independent samples. The uncertainty analysis accounts for the bias of each instrument in the measurement suite to calculate mean velocity. In this case, the velocity was calculated using Bernoulli's equation considering the flow of air to be an ideal gas. The Taylor Series Method of calculating an expanded uncertainty analysis takes the first term in a Taylor Series expansion with respect to each measured quantity. Measured in this study are the differential pressure, temperature, atmospheric pressure. Included in the random uncertainties are systematic error correlation effects, like the digitization of the data.

Efforts were focused on the balance of data accuracy with reasonable total measurement time, considering the open to atmosphere nature of the facility. Point wise data collection time had to be balanced with the unpredictability of inlet weather conditions to determine an appropriate overall profile time length. Uncertainty of the specific measurement device being used must be considered

when trying to gain information from a turbulent flow of interest. Instruments with additional complexities sometimes preclude obtaining the most relevant trends about specific experimental flow setups. The final expanded uncertainty for the mean velocity was calculated using representative values as a nominal 2.5% uncertainty at 95% confidence. The result of the Taylor Series Method expanded uncertainty analysis was confirmed by a Monte Carlo simulation.

Large atmospheric eddies are responsible for downstream non-periodic shifts of the wake in the rotor plane known as wake meandering. Wake meandering is investigated in this dissertation downstream of two 0.25 m diameter model turbines, a rotating bladed scale model and a drag matched porous disk. The two models were placed individually in boundary layer flow and vertical profiles at 67 wall normal locations were measured of stream wise velocity in the wake of these models. The vertical profile spans from 0.01 m to a wall normal 0.95 m, encompassing the height of the boundary layer. These time series were acquired with high temporal resolution hot wire anemometry at 8 downstream locations ranging from 1 to 20 diameters downstream of the models. The spectra was calculated from the time series at every measurement location and a 5^{th} order regression was used on the premultiplied spectra to identify the maximum frequency and spectral energy content. It is assumed that the peak energy from the regression and associated frequency located in the premultiplied spectra of the wake is the wake meandering. The near wake peak frequency of the rotating turbine is heavily effected by the blade passage frequency, but the two models become similar in both peak frequency and energy content at around $6D$ downstream in this setup. It is found that the peak meandering frequency in the wake of the single models decays with downstream distance and returns to the peak frequency of the inlet flow conditions at hub and top tip locations at 20 diameters downstream.

An array was then constructed with a combination of rotating model turbines and porous disks. The array was spaced at 8 and 10 diameters in the stream wise direction and 4 diameters in the span wise direction, the same array dimensions as the study determining the fully developed nature of the flow. 86 porous disks were used to build up the array and a 3×3 array of rotating turbines was placed just upstream of the measurement location to reintroduce the swirling flow components

and tip vortices into the near wake. Stream wise velocity measurements were acquired in vertical profiles of 74 wall normal locations at center-line. The profiles were located at a stream wise distance of x/D =2 and 4 downstream of four different model turbine rows. From these time series, the evolution of peak frequency internal to the array is obtained from the method outlined above. It is found that the internal array peak frequencies decrease with downstream distance in the array implying an increase in structure size. Additionally, when more than one turbine is aligned in the stream wise direction, the wakes become amplified as seen by the increase of spectral energy with downstream evolution. Far downstream in the fully developed region of flow, the wakes organize into structures that depend on the spacing of the turbines in the array and internal farm velocity. The array produces it's own resonance that is independent from the inlet boundary layer structures. A scale decomposition of the velocity signal was performed using the Hilbert transform that separated large and small scale excursions from the mean. It was shown that the large scale motions amplitude modulate the small scale motions in the boundary layer and wake. In the wake, the correlation between large and small scales amplitudes was higher than outside of the wake indicating the affect of the model turbine's wake on the turbulence in the flow.

The knowledge gain here regarding wake meandering should help inform the passive optimization of wind farm layouts and future tuning of turbines for active optimization such as active load reduction by pitch or yaw actuation. Knowledge of the meandering frequency evolution could also be used to space turbines appropriately for improved monitoring and performance for higher energy extraction.

7.0.1 Future Work

Comparing the current data set to similar conditions from modelers would be a good starting point. Distributing the publicly available data set to modelers (Appendix A) to calibrate wind turbine farm LES codes using actuator disk models should be of high importance. Looking at the difference between the physical data set and simulations with periodic boundary conditions could also be interesting to see if the boundary conditions impart un-physical conditions onto the flow.

This data set can also be used for atmospheric modelers who currently apply a surface roughness where a large wind farm exists. Understanding the flow patters within a large array can aid with fine tuning the momentum extraction of the array and the surface roughness term in atmospheric models. This will help with the understanding of the farm's influence on weather patterns, far downstream of the array itself.

Whether the flow reaches a fully developed boundary layer state depends on wind turbine spacing remains to be investigated. More turbine spacings are needed to confirm the fully developed condition in a variety of stream wise and span wise configurations. The direction of the wind will of course have impact on the velocity profiles far downstream. This case is specifically set up in the worst case scenario where all the turbine rows and columns are aligned with the prevailing direction. Future studies could include wake steering caused by turbine yaw direction and veer created by the Coriolis forces caused by earth's rotation.

It would be useful to develop a paramaterization or algorithm that could be use to increase predictability of the fluid dynamic similarity from one row to the next far downstream. Obtaining more components of velocity with higher temporal resolution would allow for the investigation of statistical convergence of the turbulence terms. A high resolution full field data, such as PIV, set would be ideal to understand the vertical kinetic energy transport needed for sustained power production far downstream. Furthermore, a full field data set would allow for the calculation of energy containing modes in the flow by usage of proper orthogonal decomposition.

A confirmation of the wake meandering proposed in this study with multi point statistics or a field view would be useful to compare with current measurements. A multi-instrument study would be useful to calculate coherency cross correlations from the inlet of the array to multi-rows downstream of the inlet. Additionally, this would allow for the investigation of yawing torque on downstream rotors with position of upstream wakes. How the wakes within the array meander and coalesce is dependent on the size of incoming structures from the boundary layer, but this was only viewed in this thesis with single point statistics. A more in depth study should be undertaken to

reveal in situ influence of structure size and evolution of scale with increasing number of turbine rows.

BIBLIOGRAPHY

[1] R. J. Adrian. Hairpin vortex organization in wall turbulence. *Physics of Fluids*, 2007.

[2] AIAA. Standard s-071a: Assessment of experimental uncertainty with application to wind tunnel testing. *American Institute of Aeronautics and Astronautics*, 1999.

[3] J. Ainslie. Calculating the flow field in the wake of wind turbines. *Journal of Wind Engineering and Industrial Aerodynamics*, 27:213–224, 1988.

[4] W. Al-Nassar, S. Alhajraf, M. Al-Sudirawi, and G. Joseph. Kisr long atmospheric boundary layer wind tunnel. In *Proceedings of ICAR5/GCTE-SEN Joint Conference, International Center for Arid and Semiarid Lands Studies, Texas Tech Unicersity, Lubbock, Texas, USA Publication 02-2*, 2002.

[5] S. J. Andersen, J. N. Sorensen, and R. Mikkelsen. Simulation of the inherent turbulence and wake interaction inside an infinitely long row of wind turbines. *Journal of Turbulence*, 2013.

[6] S. J. Andersen, J. N. Sorensen, and R. F. Mikkelsen. Turbulence and entrainment length scales in large wind farms. *Philosophical Transactions A*, 2017.

[7] S. J. Andersen, B. Witha, S.-P. Breton, J. N. Sorensen, R. F. Mikkelsen, and S. Ivanell. Quantifying variability of large eddy simulations of very large wind farms. *Journal of Physics: Conference Series 625. Wake Conference*, 2015.

[8] C. L. Archer, A. Vasel-Be-Hagh, C. Yan, S. Wu, Y. Pan, J. F. Brodie, and A. E. Maguire. Review and evaluation of wake loss models for wind energy applications. *Applied Energy*, 226:1187–1207, sep 2018.

[9] ASCE/SEI. Wind tunnel testing for buildings and other structures. *American Society of Civil Engineers*, (ASCE/SEI 49-12), 2012.

[10] ASCE/SEI. Minimum design loads and associated criteria for buildings and other structures. *American Society of Civil Engineers*, (ASCE/SEI 7-12), 2016.

[11] S. Aubrun, S. Loyer, P. E. Hancock, and P. Hayden. Wind turbine wake properties: Comparison between a non-rotating simplified wind turbine model and a rotating model. *Wind Engineering and Industrial Aerodynamics*, 2012.

[12] E. Barlas, S. Buckingham, and J. van Beeck. Roughness effects on wind-turbine wake dynamics in a boundary-layer wind tunnel. *Boundary-Layer Meteorology*, 2016.

[13] R. Barlow. Systematic errors: Facts and fictions. *Advanced Statistical Techniques in HEP*, 2002.

[14] D. B. Barrie and D. B. Kirk-Davidoff. Weather response to a large wind turbine array. *Atmospheric Chemistry and Physics*, 10(2):769–775, jan 2010.

[15] R. Barthelmie, S. Pryor, S. Frandsen, K. Hansen, J. Schepers, K. Rados, W. Schlez, A. Neubert, L. Jensen, and S. Neckelmann. Quantifying the impact of wind turbine wakes on power output at offshore wind farms. *Atmospheric and Oceanic Technology*, 27:1302–1317, 2010.

[16] R. J. Barthelmie, K. Hansen, S. T. Frandsen, O. Rathmann, J. G. Schepers, W. Schlez, J. Phillips, K. Rados, A. Zervos, E. S. Politis, and P. K. Chaviaropoulos. Modelling and measuring flow and wind turbine wakes in large wind farms offshore. *Wind Energy*, 12(5):431–444, 2009.

[17] K. Beland, J. Bibeau, C. Gagnon, and J. Landry. Offshore wind turbine arrays. *TECH 797 Ocean Project final report. Sea Grant. University of New Hamsphire*, 2013.

[18] J. S. Bendat. *RANDOM DATA Analysis and Measurement Procedures*. Wiley-Interscience, 1971.

[19] F. Bingol, G. C. Larsen, and J. Mann. Wake meandering - an analysis of instantaneous 2d laser measurements. *Journal of Physics: Conference Series. The science of making torque from wind*, 2007.

[20] F. Bingol, J. Mann, and G. C. Larsen. Light detection and ranging measurements of wake dynamics part i: One-dimensional scanning. *Wind Energy*, 2010.

[21] K. Bithas and P. Kalimeris. A brief history of energy use in human societies. In *Revisiting the Energy-Development Link*, pages 5–10. Springer International Publishing, dec 2015.

[22] J. Bossuyt, M. F. Howland, C. Meneveau, and J. Meyers. Measurement of unsteady loading and power output variability in a micro wind farm model in a wind tunnel. *Experimental Fluids*, 2016.

[23] A. L. Buck. New equations for computing vapor pressure and enhancement factor. *National Center for Atmospheric Research*, 1981.

[24] W. V. Burton. Wind tunnel simulation of an atmospheric boundary layer. Master's thesis, Texas Tech University, 2001.

[25] R. Cal, J. Lebron, L. Castillo, H. Kang, and C. Meneveau. Experimental study of the horizontally averaged flow structure in a model wind-turbine array boundary layer. *J. Renewable and Sustainable Energy*, 2(013106), 2010.

[26] M. Calaf, C. Meneveau, and J. Meyers. Large eddy simulation study of fully developed wind-turbine array boundary layers. *Physics of Fluids*, 22(015110), 2010.

[27] M. Calaf, M. B. Parlange, and C. Meneveau. Large eddy simulation study of scalar transport in fully developed wind-turbine array boundary layers. *Physics of Fluids*, 23(126603), 2011.

[28] E. H. Camp and R. B. Cal. Mean kinetic energy transport and event classification in a model wind turbine array versus an array of porous disks: Energy budget and octant analysis. *Physical Review Fluids*, 1(4), aug 2016.

[29] L. Castillo and W. George. Similarity analysis for turbulent boundary layer with pressure gradient: Outer flow. *AIAA Journal*, 2001.

[30] I. P. Castro, H. Cheng, and R. Reynolds. Turbulence over urban-type roughness: Deductions from wind-tunnel measurements. *Boundary-Layer Meterology*, 118:109–131, 2006.

[31] L. Chamorro, R. Arndt, and F. Sotiropoulos. Turbulence properties within a staggered wind farm. an experimental study. *Boundary-Layer Meteorology*, 141:349–367, 2011.

[32] L. P. Chamorro, R. Arndt, and F. Sotiropoulos. Turbulent flow properties around a staggered wind farm. *Kluwer Academic Publishers*, 2011.

[33] K. Charmanski. Experimental investigation of large model wind turbine arrays. Master's thesis, University of New Hampshire, 2013.

[34] K. Charmanski, J. Turner, and M. Wosnik. Physical model study of the wind turbine array boundary layer. In *ASME 2014 4th Joint US-European Fluids Eng. Division Summer Meeting*, Chicago, 2014.

[35] M. Churchfield, S. Lee, P. Moriarty, L. Martinez, S. Leonardi, G. Vijayakumar, and J. Brasseur. A large-eddy simulations of wind-plant aerodynamics. *50th AIAA Aerospace Sciences Meeting including the New Horizons Forum and Aerospace Exposition*, jan 2012.

[36] H. Coleman and W. Steele. *Experimentation, Validation, and Uncertainty Analysis for Engineers, 3rd*. John Wiley & Sons, Inc., 2009.

[37] G. P. Corten, P. Schaak, and T. Hegberg. Velocity profiles measured above a scale wind farm. *Energy Research centre of the Netherlands, ECN Wind Energy*, 2002.

[38] N. Coudou, S. Buckingham, and J. van Beeck. Experimental study on the wind-turbine wake meandering inside a scale model wind farm placed in an atmospheric-boundary layer wind tunnel. *IOP Conf. Series: Journal of Physics: Conf. Series 854. Wake Conference*, 2017.

[39] A. Creech, W.-G. Früh, and A. E. Maguire. Simulations of an offshore wind farm using large-eddy simulation and a torque-controlled actuator disc model. *Surveys in Geophysics*, 36(3):427–481, feb 2015.

[40] DOE. Wind technologies market report. *United States Department of Energy: Office of Energy Efficiency and Renewable Energy*, 2017.

[41] N. P. Dufresne. Experimental investigation of the turbulent axisymmetric wake with rotation generated by a windturbine. Master's thesis, University of New Hampshire, 2013.

[42] R. Ebner. *Influences of roughness on the inertial mechanism of turbulent boundary-layer scale separation*. PhD thesis, University of New Hampshire, 2014.

[43] ELD. http://www.eldinc.com/. 2019.

[44] G. Espana, S. Aubrun, S. Loyer, and P. Devinant. Spatial study of the wake meandering using modelled wind turbines in a wind tunnel. *Wind Energy*, 2011.

[45] G. Espana, S. Aubrun, S. Loyer, and P. Devinant. Wind tunnel study of the wake meandering downstream of a moddelled wind turbine as an effect of large scale turbulent eddies. *Journal of Wind Engineering and Industrial Aerodynamics*, 2012.

[46] C. Farell and A. K. Iyengar. Experiments on the wind tunnel simulation of atmospheric boundary layers. *Journal of Wind Engineering and Industrial Aerodynamics*, 1999.

[47] I. Farrance and R. Frenkel. Uncertainty in measurement: A review of monte carlo simulation using microsoft excel for the calculation of uncertainties through functional relationships, including uncertainties in empirically derived constants. *Clinical Biochemical Review*, 35(1):37–61, 2014.

[48] A. J. Favre, J. J. Gaviglio, and R. Dumas. Space-time double correlatons and spectra in a turbulent boundary layer. *Journal of Fluid Mechanics*, 1957.

[49] A. M. Ferrar. Averaging and representation of asynchronous spatial measurements. *Journal of Verification, Validation and Uncertainty Quantification*, 1, September 2016.

[50] S. Frandsen. On the wind speed reduction in the center of large clusters of wind turbines. *Wind Engineering and Industrial Aerodynamics*, 39:251–265, 1992.

[51] D. Frum. *How We Got Here: The 70's: The Decade that Brought You Modern Life (For Better or Worse)*. Basic Books, 2008.

[52] A. T. G Buresti. On the error sensitivity of calibration procedures for normal hot-wire probes. *Measurement Science Technology*, 2991.

[53] W. K. George. *Lectures in Turbulence for the 21st Century*. http://www.turbulence-online.com/publication.html, 2013.

[54] W. K. George and L. Castillo. Zero-pressure-gradient turbulent boundary layer. *Applied Mechanics Reviews*, 50(12):689, 1997.

[55] P. Gipe. The wind industrys experience with aesthetic criticism. *Leonardo 26, 243-248*, 1993.

[56] J. P. Goit and J. Meyers. Optimal control of energy extraction in wind-farm boundary layers. *J. Fluid Mechanics*, 768:5–50, 2015.

[57] J. P. Goit, W. Munters, and J. Meyers. Optimal coordinated control of power extraction in les of a wind farm with entrance effects. *Energies*, 9(29), 2016.

[58] GWEC.net. Global wind energy council. 2018.

[59] M. Hahn and P. Gilman. Offshore wind markey and economic analysis. *2014 Annual Market Assessment*, DE-EE0005360, 2014.

[60] N. Hamilton, H. S. Kang, C. Meneveau, and R. B. Cal. Statistical analysis of kinetic energy entrainment in a model wind turbine array boundary layer. *Journal of renewable and sustainable energy*, 4(063105), 2012.

[61] P. E. Hancock and T. D. Farr. wind-tunnel simulations of wind-turbine arrays in neutral and non-neutral winds. *Journal of Physics: Conference Series. The science of making torque from wind*, 2014.

[62] Z. Harun. *The structure of adverse and favourable pressure gradient turbuelnt boundary layers*. PhD thesis, University of Melbourne, 2012.

[63] C. Hasager, N. Nygaard, P. Volker, I. Karagali, S. Andersen, and J. Badger. Wind farm wake: The 2016 horns rev photo case. *Energies 10:317, 03*, 2017.

[64] C. B. Hasager, L. Rasmussen, A. Pena, L. E. Jensen, and P.-E. Rethore. Wind farm wake: The horns rev photo case. *Energies*, 2013.

[65] M. Heisel, J. Hong, and M. Guala. The spectral signature of wind turbine wake meandering: A wind tunnel and field-scale study. *Wind Energy*, 21(9):715–731, apr 2018.

[66] X. Z. HongYou Liu, GuoHua Wang. Spatial length scales of large-scale structures in atmospheric surface layers. *Physical Review Fluids*, 2017.

[67] K. B. Howard, A. Singh, F. Sotiropoulos, and M. Guala. On the statistics of wind turbine wake meandering: An experimental investigation. *Physics of Fluids*, 2015.

[68] N. Hutchins and I. Marusic. Evidence of very long meandering features in the logarithmic region of turbulent boundary layers. *Journal of Fluid Mechanics*, 2006.

[69] J. G. Ikenberry. *The Irony of State Strength: Comparative Responses to the Oil Shocks in the 1970's*, volume 40 (1) 105-137. International Organization, 1986.

[70] H. Irwin. the design of spires for wind simulation. *Journal of Wind Engineering and Industrial Aerodynamics*, 7:361–366, 1980.

[71] ISO. Guide to the expression of uncertainty in measurement. *International Organization for Standardization (ISO)*, Geneva, 1993.

[72] G. V. Iungo, F. Viola, S. Camarri, F. Porte-Agel, and F. Gallaire. Linear stability analysis of wind turbine wakes performed on wind tunnel measurements. *Journal of Fluid Mechanics*, 2013.

[73] N. Jensen. A note on wind generator interaction. *Riso National Laboratory*, 1983.

[74] N. Jensen, I. Katic, and J. Hojstrup. A simple model for cluster efficiency. *W. Palz & E. Sesto (Eds.), EWEC'86 Proceedings. Vol. 1 (pp. 407-410)*, 1987.

[75] P. B. Johansson. *The Axisymmetric Turbulent Wake*. PhD thesis, Chalmers University of Technology, 2002.

[76] J. Jonkman, S. Butterfield, W. Musial, and G. Scott. Definition of a 5 mw reference wind turbine for offshore system developement. *Technical Report NREL/ TP - 500 - 38060*, 2009.

[77] D. W. Keith, J. F. DeCarolis, D. C. Denkenberger, D. H. Lenschow, S. L. Malyshev, S. Pacala, and P. J. Rasch. The influence of large-scale wind power on global climate. *Proceedings of the National Academy of Sciences*, 101(46):16115–16120, nov 2004.

[78] J. Klewicki, P. Fife, T. Wei, and P. McMurtry. A physical model of the turbulent boundary layer consonant with mean momentum balance structure. *Philosophical Transactions of the Royal Society A: Mathematical, Physical and Engineering Sciences*, 365(1852):823–840, mar 2007.

[79] J. C. Klewicki. Reynolds number dependence, scaling, and dynamics of turbulent boundary layers. *Journal of Fluids Engineering*, 132(9):094001, 2010.

[80] J. C. Klewicki and R. E. Falco. On accurately measuring statistics associated with small-scale structure in turbulent boundary layers using hot-wire probes. *Journal of Fluid Mechanics*, 219(-1):119, oct 1990.

[81] L. S. G. Kovasznay, V. Kibens, and R. F. Blackwelder. Large-scale motion in the intermittent region of a turbulent boundary layer. *Journal of Fluid Mechanics*, 1970.

[82] H. Kozmar. Natural wind simulation in the tum boundary layer wind tunnel. In *European and African Conference on Wind Engineering, EACWE 5*, 2009.

[83] B. W. Lance and B. L. Smith. Experimental validation benchmark data for computational fluid dynamics of transient convection from forced to natural with flow reversal on a vertical flat plate. *Journal of Verification, Validation and Uncertainty Quantification*, 2016.

[84] G. Larsen, J. Mann, J. Sorensen, M. Nielsen, and R. Mikkelsen. Dynamic wake meandering modeling. *Riso National Laboratory*, 2007.

[85] L. Lignarolo, D. Ragni, C. S. Ferreiera, and G. van Bussel. Kinetic energy entrainment in wind turbine and actuator disk wakes: an experimental analysis. *Journal of Physics*, Conference Series 524: The science of making torque from wind(012163), 2014.

[86] L. A. Limited. Londonarray.com. *22 Mount Ephraim, Tunbridge Wells, Kent TN4 8AS*, 2019.

[87] K. Maalawi and M. Badr. A practical approach for selecting optimum wind rotors. *Renewable Energy*, 2003.

[88] J. Manwell, J. McGowan, and A. Rogers. Wind energy explained: Theory design and application. *Wiley. United States.*, 2002.

[89] D. Medici and P. H. Alfredsson. Measurements behind model wind turbines: Further evidence of wake meandering. *Wind Energy*, 2008.

[90] C. Meneveau. The top-down model of wind farm boundary layers and its applications. *Journal of Turbulence*, 2012.

[91] Y.-A. Muller, S. Aubrun, and C. Masson. Determination of real-time predictors of the wind turbine wake meandering. *Experimental Fluids*, 2015.

[92] J. Naughton. Validation hierarchy. *Oldenburg ForWind Wind Energy Science and Wind Tunnel Experiments Conference*, 2018.

[93] M. M. Navarro. Ocean wave data analysis using hilbert transform techniques. Master's thesis, Naval Postgraduate School, 1996.

[94] J. Newman, D. A. Drew, and L. Castillo. Psuedo spectral analysis of the energy entrainment in a scaled down wind farm. *Renewable Energy*, 2013.

[95] NGI. Middelgrunden offshore wind farm. *https://www.ngi.no/eng/*, 2018.

[96] NREL. 2017 offshore wind technologies market update. *U.S. Department of Energy Office of Energy Efficiency and Renewable Energy*, 2018.

[97] W. L. Oberkampf and T. G. Trucano. Verification and validation in computational fluid dynamics. *Progress in Aerospace Sciences*, 2002.

[98] R. L. Panton. *Incompressible Flow*. Wiley, 2005.

[99] P. D. Pictures. https://www.publicdomainpictures.net/en/view-image.php?image=9818&picture=zaanse-schans-windmills three windmills in zaanse schans in holland. *Electronic*.

[100] A. K. Prasad. Analytical solution for the optimal spacing of wind turbines. *Journal of Fluids Engineering*, 136(011107), 2014.

[101] S. B. Roy. Can large wind farms affect local meteorology? *Journal of Geophysical Research*, 109(D19), 2004.

[102] M. D. C. Saavedra. *Don Quixote*. PENGUIN GROUP, 2003.

[103] P. J. Schubel and R. J. Crossley. Wind turbine blade design. *Energies*, 5(9):3425–3449, sep 2012.

[104] A. Sescu and C. Meneveau. Large-eddy simulations and single-column modeling of thermally stratified wind turbine arrays for fully developed, stationary atmospheric conditions. *Atmospheric and Oceanic Technology*, 32:1144–1162, 2015.

[105] L. Skynyrd. Sweet home alambama. *Second Helping*, 1974.

[106] B. L. Smith and W. L. Oberkampf. Limitations of and alternatives to traditional uncertainty quantification for measurements. In *ASME 4th Join US-European Fluids Engineering Division Summer Meeting*, 2014.

[107] S. Steiros and M. Hultmark. Drag on flat plates of arbitrary porosity. *Journal of Fluid Mechanics*, 2018.

[108] R. Stevens, D. Gayme, and C. Meneveau. Coupled wake boundary layer model of windfarms. *Journal of Renewable and Sustainable Energy*, 2014.

[109] G. Taylor-Power. Experimental investigation of turbulent wakes generated by wind turbine models in a large boundary layer wind tunnel. Master's thesis, University of New Hampshire, 2018.

[110] R. Theunissen, P. Housley, C. B. Allen, and C. Carey. Experimental verification of computational predictions in power generation variation with layout of offshore wind farms. *Wind Energy*, 2014.

[111] J. Turner and M. Wosnik. (submitted) velocity data in a fully developed experimental wind turbine array boundary layer. *Wind Energy*, 2019.

[112] M. Tutkun, W. George, J. Delville, M. Stanislas, P. Johansson, J.-M. Foucaut, and S. Coudert. Two-point correlations in high reynolds number flat plate turbulent boundary layers. *Journal of Turbulence*, 2008.

[113] G. A. M. van Kuik, J. Peinke, R. Nijssen, D. Lekou, J. Mann, J. N. Sørensen, C. Ferreira, J. W. van Wingerden, D. Schlipf, P. Gebraad, H. Polinder, A. Abrahamsen, G. J. W. van Bussel, J. D. Sørensen, P. Tavner, C. L. Bottasso, M. Muskulus, D. Matha, H. J. Lindeboom, S. Degraer, O. Kramer, S. Lehnhoff, M. Sonnenschein, P. E. Sørensen, R. W. Künneke, P. E. Morthorst, and K. Skytte. Long-term research challenges in wind energy – a research agenda by the european academy of wind energy. *Wind Energy Science*, 1(1):1–39, feb 2016.

[114] P. Vincenti, J. Klewicki, C. Morrill-Winter, C. White, and M. Wosnik. treamwise velocity statistics in turbulent boundary layers that spatially develop to high reynolds number. *Experimental Fluids*, 54(1629), 2013.

[115] T. von Kármán. Progress in the statistical theory of turbulence. *Proceedings of the National Academy of Sciences of the United States of America*, 1948.

[116] B. M. Wilson and B. L. Smith. Taylor-series and monte-carlo-method uncertainty estimation of the width of a probability distribution based on varying bias and random error. *Measurement Science and Technology*, 24(3):035301, jan 2013.

[117] J. G. Wissink and W. Rodi. Numerical study of the near wake of a circular cylinder. *International Journal of Heat and Fluid Flow*, 2008.

[118] E. A. Wrigley and R. S. Schofield. *The Population History of England 1541-1871. A Reconstruction*. Cambridge University Press, 1989.

[119] Z. Yang, Y. Li, and J. E. Seem. Multi-model predictive control for wind turbine operation under meandering wake of upstream turbines. *Control Engineering Practice*, 2015.

[120] W. Zhang, C. D. Markfort, and F. Porte-Agel. Near-wake flow structure downwind of a wind turbine in a turbulent boundary layer. *Experimental Fluids*, 2012.

APPENDIX A

DATA SET AVAILABILITY

The mean velocity data set presented in Chapter 5 has been made publicly available. Post processed 6 minute time averages of velocity per point are archived via Figshare.com, a data hosting website that can supply permanent digital object identifiers (DOIs). Access is available through the MIT license and can be accessed via

DOI: `http://dx.doi.org/10.6084/m9.figshare.5197204`

Or on the figshare website with the article name:

`Processed_Data_FullyDevelopedWindTurbineArrayBoundaryLayer_r0`

The files are broken up into each profile and mean values are provided for each time series point within the profile file. A separate file for quantities that are considered stationary over the course of a profile is provided.

APPENDIX B

GOVERNING EQUATIONS

B.1 What is a fluid?

A fluid is a substance that deforms under infinitesimal shear. In other words, fluids are wimpy. We experience fluids non-stop in everyday life from our cardiovascular systems to the atmosphere to transportation and the only way to escape all influences of the physics of fluid dynamics is certainly death. A fluid can be a gas or a liquid and they generally fill the container they reside in. When applying a differential pressure to a fluid in the continuum mechanics regime, a flow is created towards the lower pressure, away from the higher pressure. The equations that govern the physics of the flow of fluids are the Navier-Stokes Equations as seen in Section B.3.

B.2 Reynolds Numbers

Parameters in the field of fluid dynamics are frequently non-dimensional. It is convenient to express how different systems behave in terms of these non-dimensional parameters due to the scalability of the physics. One such highly important parameter is the Reynolds Number shown with respect to development fetch x in Equation B.1.

$$Re_x = \frac{Ux}{\nu} \tag{B.1}$$

The Reynolds number is a ratio between inertial forces and viscous forces and can lead one to an understanding of the relative level of dominant forces in the flow. If the Reynolds number is low

(less than 1), viscous forces are dominant, turbulence is unlikely, and the flow moves with a slow, sticky, layered behavior called laminar flow. If the Reynolds number is high ($>>1$), certainly in the case of wind energy applications, inertial forces are dominant and turbulence is increasingly likely, if not absolute.

Turbulence itself has a mutli-faceted definition. However, for our purposes, turbulence is comprised of chaotic motions of fluid where the flow's intricacies become unpredictable. Turbulence occurs when the Reynolds number has reached the point where laminar (structured in layers) flow is no longer possible. Consider the case of a flow bounded by a lower boundary, the boundary layer. In boundary layer flow, the fluid closest to the ground dumps momentum into the wall and is slowed to a stop at the lower engineering surface. The fluid higher up in the boundary layer, the freestream, is able to move much quicker, increasingly unaffected by the momentum loss to the wall. This creates a parabolic-like velocity profile where the velocity at the wall starts at zero and increases rapidly to it's freestream state away from the wall. As this flow develops, say, as we follow a single chunk of fluid downstream with velocity U, the Reynolds number is increasing with development in our variable x. At a certain point, the laminar layers of flow start to become disorderly and the flow transitions to turbulence.

The last concern of the variables that make up the Reynolds number is ν, the kinematic viscosity. The viscosity of a fluid is dependent on the properties of the substance itself, as well as the temperature which affects density. Viscosity can be colloquially defined as the stickyness of a fluid, the friction factor for substances that flow. Air has a relatively weak viscosity, as opposed to honey, which would have a high viscosity.

The a simple thought experiment elucidating the Reynolds number is as follows using honey and water as our high viscosity and low viscosity fluid respectively. Consider that one knocks

over a glass of honey and another separate glass of water. The high viscosity fluid, honey, would maintain a laminar flow state for much longer than the lower viscosity fluid, water, if put under the same conditions. The honey would take much longer to spill out of the glass and be much more orderly in it's flow structure. (That is not to say anything about the mess of cleaning up this experiment).

Let's briefly reconsider these concepts combined into the following: A turbulent boundary layer flow is the type of flow physics that we experience everyday in our atmosphere, where the substance is air. When you are at the beach, it would behoove you to fly your kite high up in the atmosphere, rather than at the ground. This concept is that of the atmospheric boundary layer. The incoming wind at the beach has had a long time to develop flowing over the large flat ocean surface caused by the differential heating of the earth due to the sun. Upon arrival to your beach, the sturcutre of the wind is certainly a large turbulent boundary layer on order 1 km in height. For this reason of increased wind at the beach, the idea of capturing this energy out in the ocean is born. Wind turbines placed on a relatively flat surface (ocean) are installed with tall heights to capture the fastest wind in the atmospheric boundary layer.

B.3 Navier-Stokes Equations

For the purpose of this work, we will consider only incompressible Newtonian flows, where density changes in the fluid are not an important part of the physics [98]. We also make the assumption that we will operate in the world of continuum mechanics. The continuum asumption simply means that physical properties are distributed through space. In incompressible flow with density, viscosity and thermal conductivity constant, we have Newton's second law for fluids, $F = ma$ for a finite volumetric element, the Navier-Stokes Equations and continuity.

$$\frac{D\tilde{u_i}}{Dt} = -\frac{1}{\rho}\frac{\partial \tilde{P}}{\partial x_i} + \nu\nabla^2\tilde{u} + f_j, \qquad \frac{d\tilde{u_i}}{dx_i} = 0 \tag{B.2}$$

where $\frac{D\tilde{u_i}}{Dt} \equiv \frac{\partial \tilde{u_i}}{\partial t} + \nabla \cdot \tilde{u_i}$

Expanding, we have

$$\frac{\partial \tilde{u_i}}{\partial t} + \tilde{u_j}\frac{\partial \tilde{u_i}}{\partial x_j} = -\frac{1}{\rho}\frac{\partial \tilde{P}}{\partial x_i} + \frac{1}{\rho}\frac{\partial \tilde{\tau_{ij}}}{\partial x_j} + f_j \tag{B.3}$$

where $\tilde{\tau}_{ij} = \mu(\frac{\partial \tilde{u_i}}{\partial x_j} + \frac{\partial \tilde{u_j}}{\partial x_i})$

B.4 Transport equation for turbulence kinetic energy

Brought forth by the consideration of vertical kinetic energy transport into a wind farm array from the prevailing boundary layer above, the turbulent kinetic energy is derived here.

Here the transport equation for turbulence kinetic energy, $\frac{1}{2}\overline{u_i'u_i'}$, is derived by subtracting the mean kinetic energy equation from the instantaneous energy equation, neglecting body forces f_j. Starting with the momentum equation (equation B.2 and multiplying by the mean velocity, U_i, we have the Mean Kinetic Energy equation

$$\underbrace{U_j\frac{\partial}{\partial x_j}(\frac{1}{2}U_iU_i)}_{A} = \underbrace{\frac{\partial}{\partial x_j}\left[-\frac{P}{\rho}U_j + 2\nu U_iE_{ij} - U_i\overline{u_i'u_j'}\right]}_{B\quad C\quad D} - \underbrace{2\nu E_{ij}E_{ij}}_{E} + \underbrace{\overline{u_i'u_j'}E_{ij}}_{F} \tag{B.4}$$

Where

1. Mean convection
2. Pressure transport
3. Mean energy

4. Turbulence

5. Viscous dissipation

6. Turbulence production

Now, taking the instantaneous momentum equation and multiplying through by $\tilde{u_i}$

$$\left[\tilde{u_j}\frac{\partial \tilde{u_i}}{\partial x_j} = \frac{-1}{\rho}\frac{d\tilde{P}}{dx_i} + \frac{\partial}{\partial x_j}(2\nu\tilde{e_{ij}})\right] \cdot \tilde{u_i} \tag{B.5}$$

with

$$\tilde{e}_{ij} = \frac{1}{2}\left(\frac{\partial \tilde{u_i}}{\partial x_j} + \frac{\partial \tilde{u_j}}{\partial x_i}\right) = \underbrace{\frac{1}{2}\left(\frac{\partial U_i}{\partial x_j} + \frac{\partial U_j}{\partial x_i}\right)}_{E_{ij}} + \underbrace{\frac{1}{2}\left(\frac{\partial u_i'}{\partial x_j} + \frac{\partial u_j'}{\partial x_i}\right)}_{e'ij} \tag{B.6}$$

and recalling the chain rule

$$\frac{\partial \tilde{u_i}\tilde{u_i}}{\partial x_j} = \tilde{u_i}\frac{\partial \tilde{u_i}}{\partial x_j} + \tilde{u_i}\frac{\partial \tilde{u_i}}{\partial x_j} = 2\tilde{u_i}\frac{\partial \tilde{u_i}}{\partial x_j} \tag{B.7}$$

We obtain the instantaneous kinetic energy equation

$$\underbrace{\tilde{u_j}\frac{\partial}{\partial x_j}(\frac{1}{2}\tilde{u_i}\tilde{u_i})}_{I} = -\underbrace{\tilde{u_i}\frac{1}{\rho}\frac{d\tilde{P}}{dx_i}}_{II} + \underbrace{\tilde{u_i}\frac{\partial}{\partial x_j}(2\nu\tilde{e}_{ij})}_{III} \tag{B.8}$$

We now expand and average the instantaneous kinetic energy equation, canceling terms that equate to zero via continuity or averaging of a fluctuating quantity, and apply chain rule to rearrange

B.4.1 Term I

$$\tilde{u_j}\frac{\partial}{\partial x_j}(\frac{1}{2}\tilde{u_i}\tilde{u_i}) = U_j\frac{\partial}{\partial x_j}(\frac{1}{2}U_iU_i) + U_j\frac{\partial}{\partial x_j}(\frac{1}{2}\overline{u_i'u_i'}) + \frac{\partial}{\partial x_j}(U_i\overline{u_i'u_j'}) + \overline{u_j'\frac{\partial}{\partial x_j}(\frac{1}{2}u_i'u_i')} \tag{B.9}$$

where

$$\overline{u_j' \frac{\partial}{\partial x_j}(\frac{1}{2}u_i'u_i')} = \frac{\partial}{\partial x_j}(\frac{1}{2}\overline{u_i'u_i'u_j'}) - \frac{1}{2}u_i'u_i' \cancelto{0,\, continuity}{\frac{\partial u_j'}{\partial x_j}} \tag{B.10}$$

$$\tilde{u_j}\frac{\partial}{\partial x_j}(\frac{1}{2}\tilde{u_i}\tilde{u_i}) = U_j\frac{\partial}{\partial x_j}(\frac{1}{2}U_iU_i) + U_j\frac{\partial}{\partial x_j}(\frac{1}{2}\overline{u_i'u_i'}) + \frac{\partial}{\partial x_j}(U_i\overline{u_i'u_j'}) + \frac{\partial}{\partial x_j}(\frac{1}{2}\overline{u_i'u_i'u_j'}) \tag{B.11}$$

B.4.2 Term II

$$\tilde{u_i}\frac{1}{\rho}\frac{d\tilde{P}}{dx_i} = -\frac{U_i}{\rho}\frac{\partial P}{\partial x_i} - \overline{\frac{u_i'}{\rho}\frac{\partial p'}{\partial x_i}} \tag{B.12}$$

$$\tilde{u_i}\frac{1}{\rho}\frac{d\tilde{P}}{dx_i} = -\frac{1}{\rho}\frac{\partial}{\partial x_i}(PU_i) - \frac{1}{\rho}\frac{\partial}{\partial x_i}(\overline{p'u_i'}) \tag{B.13}$$

Recall $\frac{\partial U_i}{\partial x_i} = \frac{\partial U_j}{\partial x_i} = 0$

$$\tilde{u_i}\frac{1}{\rho}\frac{d\tilde{P}}{dx_i} = -\frac{1}{\rho}\frac{\partial}{\partial x_j}(PU_j) - \frac{1}{\rho}\frac{\partial}{\partial x_j}(\overline{p'u_j'}) \tag{B.14}$$

B.4.3 Term III

$$\tilde{u_i}\frac{\partial}{\partial x_j}(2\nu\tilde{e_{ij}}) = 2\nu\frac{\partial U_iE_{ij}}{\partial x_j} + 2\nu\frac{\partial\overline{u_i'e_{ij}'}}{\partial x_j} - 2\nu E_{ij}\underbrace{\frac{\partial U_i}{\partial x_j}}_{E_{ij}} - 2\nu e_{ij}'\underbrace{\frac{\partial u_i'}{\partial x_j}}_{e_{ij}'} \tag{B.15}$$

Where $-2\nu E_{ij}\frac{\partial U_i}{\partial x_j}$ can be expanded to $-2\nu E_{ij}\frac{1}{2}(\frac{\partial U_i}{\partial x_j} + \frac{\partial U_i}{\partial x_j})$ swapping indices $-2\nu E_{ij}\frac{1}{2}(\frac{\partial U_i}{\partial x_j} + \frac{\partial U_j}{\partial x_i})$ and recombining with the stress tensor the term becomes $-2\nu E_{ij}E_{ij}$ The same process can be done for the $-2\nu e_{ij}'\frac{\partial u_i'}{\partial x_j}$ term.

Combining terms to one equation and subtracting the mean kinetic energy equation. The terms cancel from the above equation B.4.

$$\cancel{U_j \frac{\partial}{\partial x_j}(\frac{1}{2}U_i U_i)}^{A} + \underbrace{U_j \frac{\partial}{\partial x_j}(\frac{1}{2}\overline{u_i' u_i'})}_{1} + \cancel{\frac{\partial}{\partial x_j}(U_i \overline{u_i' u_j'})}^{D} + \underbrace{\frac{\partial}{\partial x_j}(\frac{1}{2}\overline{u_i' u_i' u_j'})}_{4} =$$

$$\cancel{-\frac{1}{\rho}\frac{\partial}{\partial x_j}(P U_j)}^{B} \underbrace{-\frac{1}{\rho}\frac{\partial}{\partial x_j}(\overline{p' u_j'})}_{2} \cancel{+2\nu \frac{\partial U_i E_{ij}}{\partial x_j}}^{C} \underbrace{+2\nu \frac{\partial \overline{u_i' e_{ij}'}}{\partial x_j}}_{3} \cancel{-2\nu E_{ij} E_{ij}}^{E} \underbrace{-2\nu \overline{e_{ij}' e_{ij}'}}_{5} \quad \text{(B.16)}$$

Finally, the turbulence kinetic energy transport equation

$$\underbrace{U_j \frac{\partial}{\partial x_j}(\frac{1}{2}\overline{u_i' u_i'})}_{1} = \underbrace{\frac{\partial}{\partial x_j}\left[\frac{-1}{\rho}\overline{u_j' p'} + 2\nu \overline{u_i' e_{ij}'} - \frac{1}{2}\overline{u_i' u_i' u_j'}\right]}_{2 \quad 3 \quad 4} \underbrace{-2\nu \overline{e_{ij}' e_{ij}'}}_{5} \underbrace{-\overline{u_i' u_j'} E_{ij}}_{6=F} \quad \text{(B.17)}$$

We label the terms in the following way:

1. Rate of change of Turbulent kinetic energy following the mean. Convective change.

2. Pressure gradient work transport

3. Turbulence kinetic energy viscous stress transport

4. Turbulent motion transport

5. Viscous dissipation of turbulence kinetic energy

6. Turbulent production (communication term with the mean kinetic energy equation)

The turbulence kinetic energy equation is associated with the turbulent fluctuations of the flow. It becomes important in knowing where the energy is in the flow.

B.4.4 Transport for the Reynolds stress tensor

Here we derive the transport for the Reynolds stress tensor, $\overline{u_i' u_j'}$ by multiplying the fluctuating momentum equation by u_k', then writing the same equation with free indeces reversed, adding the two equations together and averaging. We start with the fluctuating momentum equation, ie. the instantaneous momentum equation minus the mean momentum equation and multiply by a fluctuating velocity with independent index k

$$\left[U_j \frac{\partial u_i'}{\partial x_j} = -\frac{1}{\rho}\frac{\partial P'}{\partial x_i} + \frac{\partial}{\partial x_j}(2\nu e_{ij}') - (u_j' \frac{\partial u_i'}{\partial x_j} - \overline{u_j' \frac{\partial u_i}{\partial x_j}}) - u_j' \frac{\partial U_i}{\partial x_j} \right] \cdot u_k' \tag{B.18}$$

$$U_j \frac{\partial u_i'}{\partial x_j} u_k' = -\frac{1}{\rho}\frac{\partial P'}{\partial x_i} u_k' + \frac{\partial}{\partial x_j}(2\nu e_{ij}') u_k' - (u_j' \frac{\partial u_i'}{\partial x_j} u_k' - \overline{u_j' \frac{\partial u_i}{\partial x_j}} u_k') - u_j' \frac{\partial U_i}{\partial x_j} u_k' \tag{B.19}$$

Flipping free indeces i and k

$$U_j \frac{\partial u_k'}{\partial x_j} u_i' = -\frac{1}{\rho}\frac{\partial P'}{\partial x_k} u_i' + \frac{\partial}{\partial x_j}(2\nu e_{kj}') u_i' - (u_j' \frac{\partial u_k'}{\partial x_j} u_i' - \overline{u_j' \frac{\partial u_k}{\partial x_j}} u_i') - u_j' \frac{\partial U_k}{\partial x_j} u_i' \tag{B.20}$$

Adding these two equations together with some chain rule and continuity applied and time averaging

$$\begin{aligned} U_j \overline{\frac{\partial u_k' u_i'}{\partial x_j}} = &-\frac{1}{\rho}(\overline{\frac{\partial P'}{\partial x_k} u_i'} + \overline{\frac{\partial P'}{\partial x_i} u_k'}) + 2\nu \frac{\partial}{\partial x_j}(\overline{e_{kj}' u_i'} + \overline{e_{ij}' u_k'}) - 2\nu \overline{e_{ij}' \frac{\partial u_k'}{x_j}} - 2\nu \overline{e_{kj}' \frac{\partial u_i'}{x_j}} \\ &- \frac{\partial}{\partial x_j}(\overline{u_j' u_k' u_i'}) + \overline{u_j' \frac{\partial u_k}{\partial x_j} \cancelto{0}{u_i'}} + \overline{u_j' \frac{\partial u_i}{\partial x_j} \cancelto{0}{u_k'}} - \overline{u_j' \frac{\partial U_k}{\partial x_j} u_i'} - \overline{u_j' \frac{\partial U_i}{\partial x_j} u_k'} \end{aligned} \tag{B.21}$$

Expanding the pressure term and recombining we have the Reynolds' stress equation

$$\begin{aligned} U_j \frac{\partial}{\partial x_j}(\overline{u_k' u_i'}) = &\frac{\partial}{\partial x_j}\left[\frac{1}{\rho}(\overline{u_i' p'} \delta_{kj} + \overline{u_k' p'} \delta_{ij}) - \overline{u_i' u_j' u_k'} + 2\nu(\overline{u_k' e_{ij}} + \overline{u_i' e_{kj}}) \right] \\ &+ \overline{\frac{p'}{\rho}(\frac{\partial u_i'}{\partial x_k} + \frac{\partial u_k'}{\partial x_i})} - (\overline{u_i' u_j'} \frac{\partial U_k}{\partial x_j} + \overline{u_k' u_j'} \frac{\partial U_i}{\partial x_j}) - 4\nu \overline{e_{ij}' e_{kj}'} \end{aligned} \tag{B.22}$$

The transport equation for the Reynolds stress tensor contains (from left to right) terms that physically represent the advection of the Reynolds' stress, the transport of pressure, transport of turbu-

lent advection, and transport of viscous stress. The next term is the pressure strain rate, the mean transport of Reynolds' stress and the viscous diffusion term.

APPENDIX C

REPEATABILITY

Studies not presented in the main body of the thesis are discussed here. Data was obtained previous to the full consideration of the uncertainty analysis performed in Chapter 4. Increased complexity of instrumentation also increases measurement uncertainty, which is the focus of this appendix. The repeatability of the velocity came into question and specific locations were repeated numerous times.

C.1 Repeated Profiles

Numerous profiles were taken at $x/D = 6$ downstream of row 11 within the array of porous disks with three instruments. (1) An x-wire hot wire anemometer, (2) a single wire hot wire anemometer, (3) a pitot tube and (3) a laser doppler velocimeter (LDV). Six time series were obtained from top tip height to 1D above hub height at 10%D spacing for 10 minutes per location. These profiles, taken in an identical location and setup have different values when compared to each other, and even when obtained with the same instrument. Initially it seemed as though there were two different flow states where one set of data is consistently higher in velocity than the next. This can be seen in Figure C.1 where four profiles taken with different instruments at the same location do not match up. Two of the profiles are taken with pitot tubes attached to a differential pressure transducer and two of the profiles are taken with a laser doppler velocimeter (LDV). The seed for the LVD was provided by a streamlined airfoil with holes drilled into the trailing edge connected

to a laskin nozzle submerged in Dioctyl sebacate, an oil, that was positioned 8 m upstream of the measurement location.

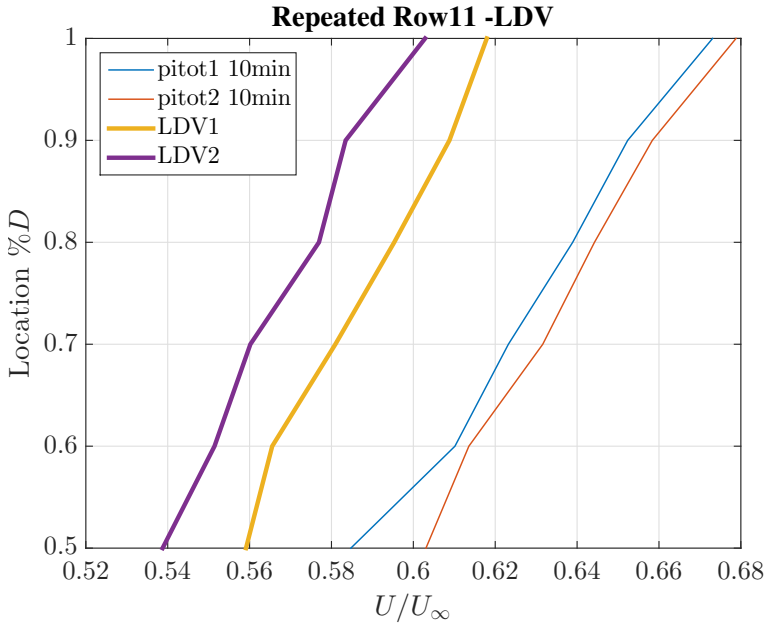

Figure C.1: Repeatability with different instruments. Measurements obtained at $x/D = 6$ downstream of row 11 in the array setup with porous disks.

It is reasonable to think that the velocity cannot be identical for each data set and an extensive consideration of uncertainty is presented in Chapter 4. Temperature differences affect density which will change flow velocity as fans are run at constant RPM. Data taken in the FPF are usually plotted in inner normalized variables and a log scale to allow focus to be placed on boundary layer measurements. This method has the advantage that any small differences are first normalized with kinematic viscosity, then collapsed together using a logarithm. The profiles we've examined that seem dissimilar are normalized by freestream velocity as per usual in the field of wind energy. It is difficult, if not impossible to extract a logarithmic region with use of a clauser chart to estimate friction velocity with this scale of roughness. When looking at boundary layer profiles, the outer

region (when scaled in inner units) doesn't always match up. In fact, the similarity only presents itself in the log region and the outer region does not show similarity even with the same freestream velocity. The region that is being examined is directly above the turbine top tip height and perhaps could use some intermediate scaling. However, the rest of the wind turbine community uses free stream velocity to normalize their profiles and it was shown in Chapter 5 that an outer normalization with boundary layer height does indeed collapse the profiles of mean velocity obtained with a pitot tube.

C.2 Hotwire Calibration

Following the work by Hultmark 2010, we look at a hotwire as a heat transfer problem and then derive a function of $U/\nu = f(E^2/k\Delta T)$ as seen in figure C.2. Where U is the velocity the wire is seeing, ν is the kinematic viscosity, recalculated at each temperature T_{amb} where $\Delta T = T_{wire} - T_{amb}$ and k is the thermal conductivity of air. The temperature of the wire is determined by the overheat ratio applied at a certain calibration temperature. This should alleviate temperature dependence on temperature for the hotwire. Hultmark applied this technique with success for temperature changes of up to 15°C.

Figure C.3 shows three separate data sets at different times lasting 3 hours each. The data set are binned and averaged to reduced the scatter of the time series on the plot. The freestream was obtained with a pitot tube positioned at 1.2 m and the hotwire was located at top tip height, although no turbines are present in these data sets. The original hotwire calibration and the Hultmark temperature varying calibration are both plotted in Figure C.3. The freestream stays relatively flat around a constant 7 m/s. With increase in temperature the original howtiwre calibration has an average decrease in velocity but stays constant in that decrease for each time series respectively.

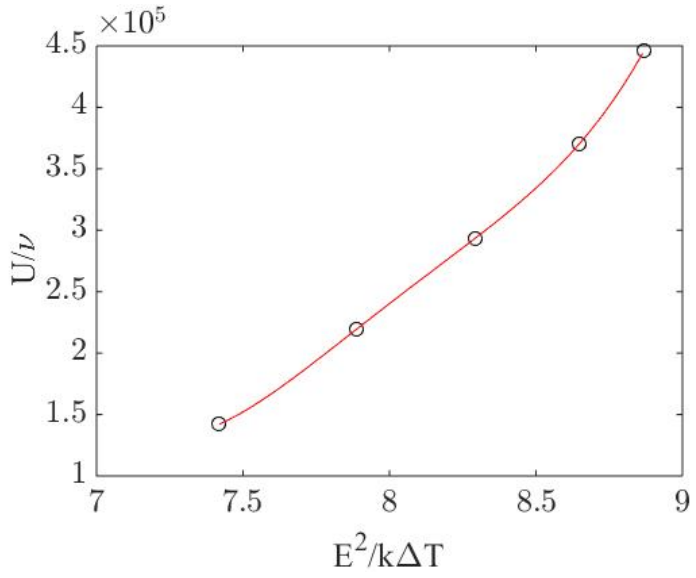

Figure C.2: Temperature corrected HW calibration method

With an increase in temperature, the temperature calibrated hotwire stays around the same average value of velocity, but a trend is noticed of a slight increase in velocity in the individual time series. Because there seems to be a warm up transient in the velocity of the hotwire with the temperature correction calibration it was not used to calibrate the hot wires in the thesis. The profiles in this body of work were calibrated using an interpolated average temperature between two calibration data sets taken before and after each profile. The linear calibrations were always applied to data sets that did not last longer than about an hour and half real time. This short time reduced the amount of temperature drift over the course of the profile.

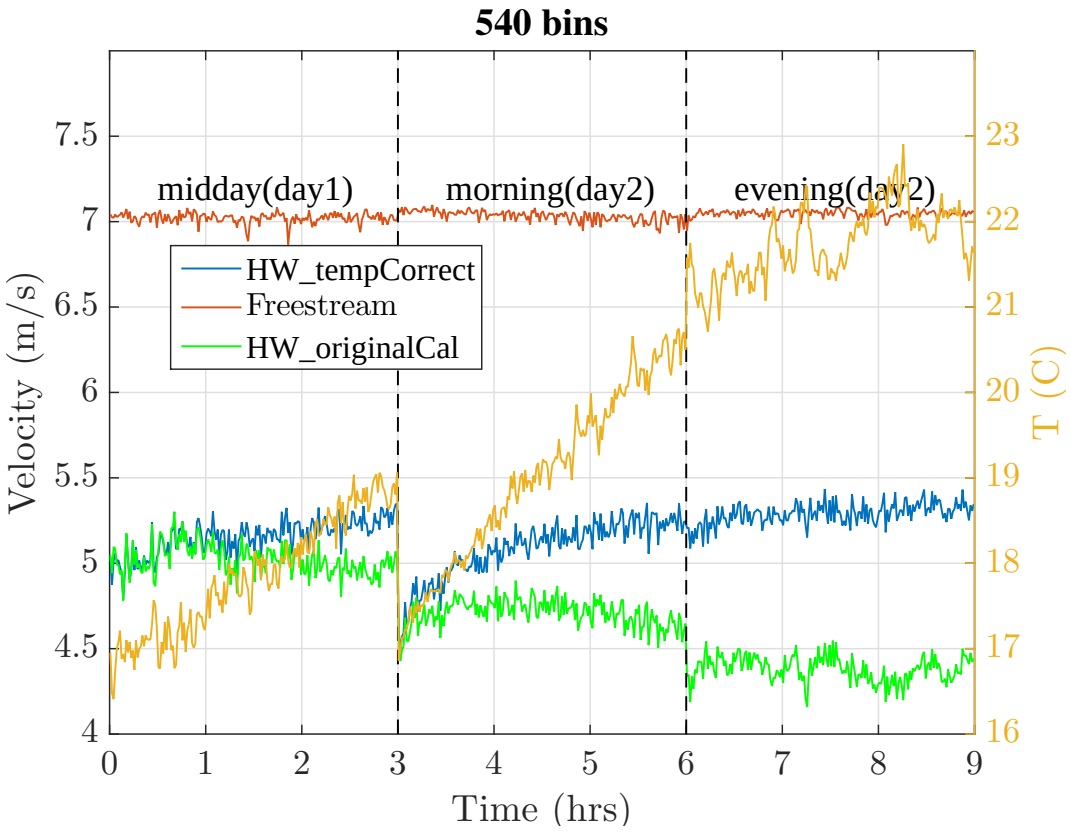

Figure C.3: Temperature corrected Hotwire with binned values for 3 different 3 hour data sets - binned every minute

The figures C.6, C.5, and C.4, are histograms of the 3 different 3hr data sets obtained on 14June16 and 15June16. Refer back to figure C.3 for the temperatures that these histograms correspond to. Note that the histrograms are very similar in peaks and distribution shape. It is gained from these histograms that there is no bimodal distribution of flow as initially conjectured.

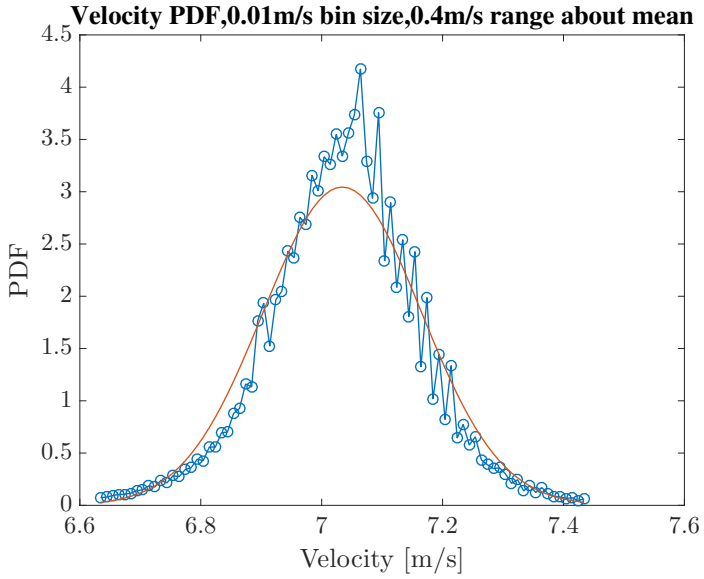

Figure C.4: Histogram of freestream velocities with combined 14June16,15June16 morning, 15June evening data sets

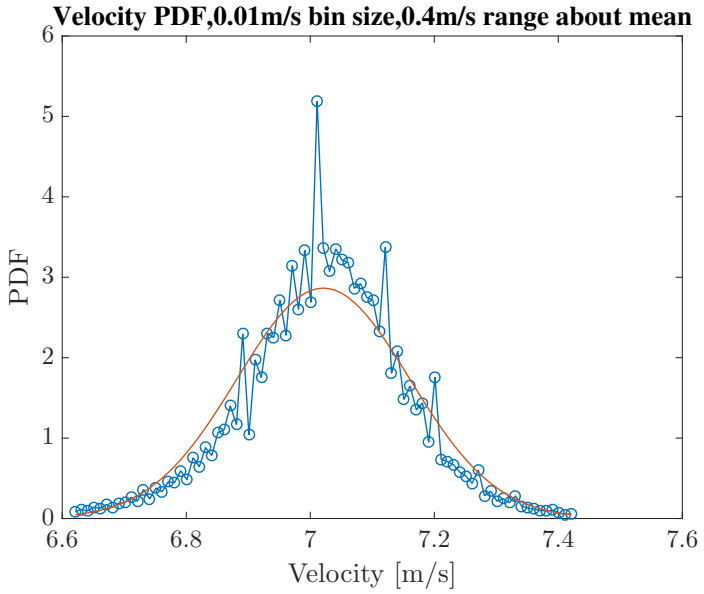

Figure C.5: Histogram of freestream velocities with only 14June16 data set

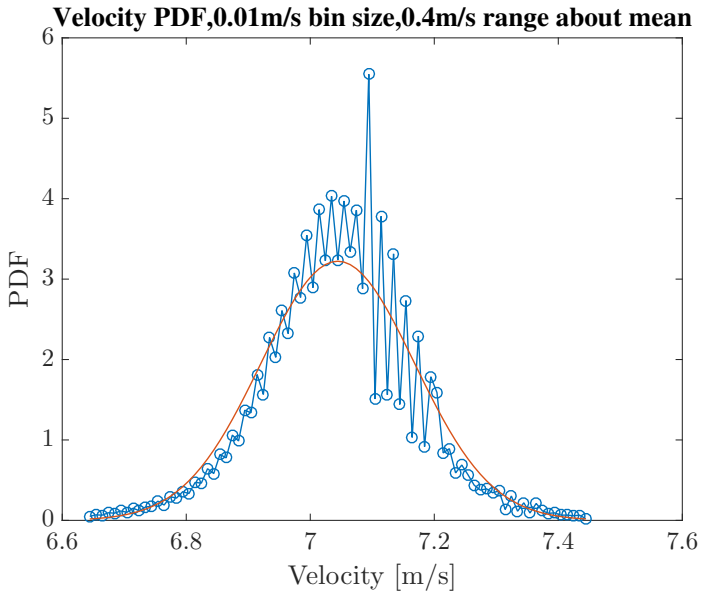

Figure C.6: Histogram of freestream velocities with only 15June16 evening data set for the first hour

C.3 Tall Profile

This section will investigate where the Freestream data should be obtained in the FPF. It is known that the inlet and turbulence management section are formed with screens sown together at certain locations. Additionally, there exists a honeycomb section, the flow straightener, which has a seam. The seam in the flow straightener opens at high speeds and presses up against one of the screens. These locations could cause a disturbance in the flow and should be avoided. Tunnel height is 2.7 m tall. It is known that it is a boundary layer wind tunnel and therefore has momentum losses on the floor and two side walls. These data sets should provide information on where the best wall normal location is, with the least disturbances from the walls, to obtain free stream velocity.

The following profiles were taken with a single wire hotwire from 800 mm off the ground to 2200 mm off the ground and calibrated at 1.4 m cross referencing a pitot tube. Each time series

was 5 minutes at a sample rate of 1 kHz. Profiles were taken with the array of porous disks (and spires) set up and measurements were obtained at a downstream location of $x/D = 6$ downstream of Row 11 and the data set was obtained again once the array was removed for an empty tunnel. Reference Figures C.7 and C.8 for velocity and turbulence profile respectively. It can be seen that the Hultmark temperature calibration functions relatively well when there is a temperature variation during the data set. There was a 3°C difference between start and end of the profile with the array set up which effects the regular calibration of the hotwire strongly. In typical operation conditions, these data sets would have been thrown out as they exceeded the 2°C limit. It seems that from figure C.7, having a pitot tube to measure freestream at 1.4 m is out of the momentum boundary layer. This 1.4 m height is just out of the turbulence boundary layer as well, or very close to it, referencing figure C.8.

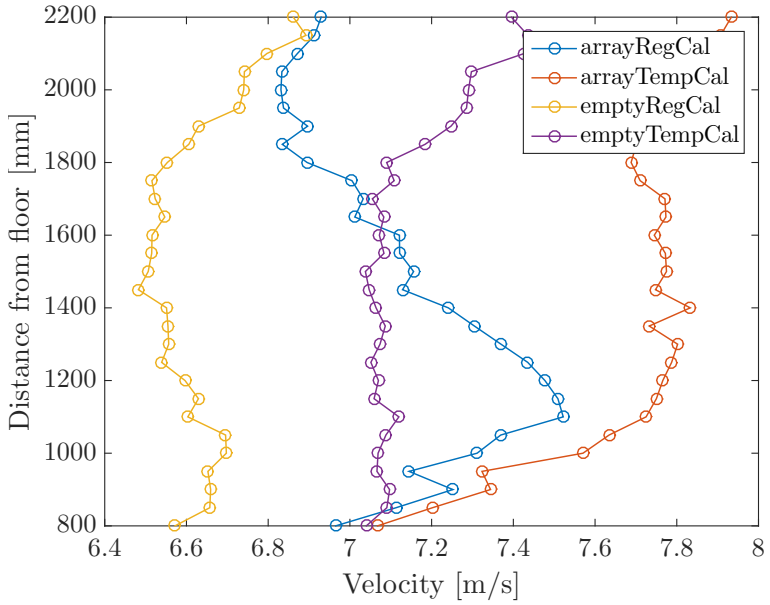

Figure C.7: Tall profile velocity

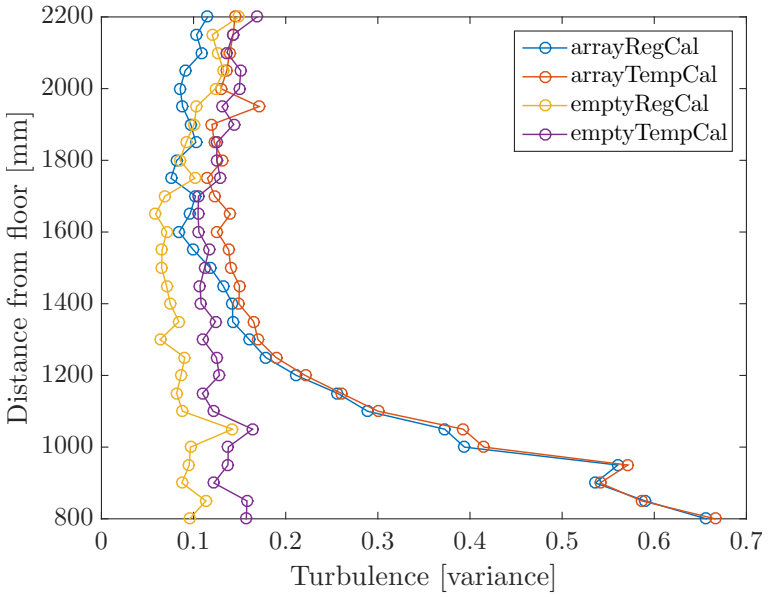

Figure C.8: Tall profile turbulence measurement

APPENDIX D

EXPERIMENT LIST

Figure D.1 shows a table of a list of data sets obtained in the FPF with scale model turbines. Not all of these data sets were utilized in this thesis. Particularly the cross wire data sets were an ambitious campaign that did not pan out with low enough uncertainty to be useful for their intended purpose. Unless otherwise noted, all of the measurements were performed at the centerline of the tunnel, which is also the cenerline of the array or object being measured.

The data sets are numbered and the names try to represent the reasoning for obtaining them. The instruments used are either pitot tubes, single wire hot wires or two component hot wires oriented to obtained the streamwise and wall normal velocities. The frequency listed is the data acquisition rate in Hertz. The time per point category is in minutes. The row location is listed because many of the studies are performed in the wind turbine array with 8 diameter streamwise spacing and 4 diameter spanwise spacing with a first row placed at 33 m downstream of the turbulence management section of the FPF. For the measurements downstream of single objects, the row location is downstream distance in diameter measured at the centerline of the object. Streamwise location indicates at what downstream location the measurement was taken behind an object in the array. For the single objects, the streamwise location remained constant at 62 m downstream while the object was moved to simulation moving downstream within the wake.

The number of points per profile is stated and vertical location is listed with a name. These names reference the set of vertical measurement locations in reference to the floor. These measurements are listed below for completeness.

Spacing indicates the array stream wise spacing. Free stream indicates the vertical location at which a pitot tube is placed to measure the free stream velocity. The spires are either not used or placed at 5 m downstream of the inlet. The temperature was either measured from the national instruments PXI computer or with an externally amplified thermocouple at the measurement location or placed in the tunnel with the data acquisition computer on a cart. The cart was placed as far away as possible from the measurement location, but had to be located in the test section due to limitations of cable lengths. For instance, the length of the BNC cable that attaches to the hot wire anemometer channels was specified to be no greater than 5 m as listed by the AA-1003 specification sheet and manual. The pitot tube also had to be connected via tygon tubing to a differential pressure meter, and care was taken to minimize the length of this Tygon tubing, while moving the pressure meter as far away from the measurement location as possible.

No.	DataSet Name	Instrument	Frequency	Time/pt	Row Location	Streamwise Locations	No. points/profile
1	FullyDevelopedPitot	Pitot tube	100 Hz	6min	R0-17 (R1@33m)	x/D = 6	24
1a	Inlet hotwire profile	single HW	1kHz	6min	31m downstream	x/D = -2	24
2	XarrayR17 Tight	xwire	5kHz	3min	R17 (R1@33m)	x/D = 1-7	28
3	Equil Region	xwire	5kHz	10min	R11-17(R1@33m)	x/D = 6	6
4	Realistic turbines 3x3	single HW	10kHz	1min	5x5,9x5,14x5,19x5	x/D = 2,4	74
4a	nothing in tunnel 62m	single HW	10kHz	1min	62m downstream	62m downstream	74
5	Single turbine BL	single HW	10kHz	1min	1,2,4,6,8,10,14,20D	62m downstream	67
5a	Single disk BL	single HW	10kHz	1min	1,2,4,6,8,10,14,20D	62m downstream	67

No.	Vertical Locations	Spacing	Freestream	Spires	Temperature	Notes
1	Locations_fromBottom	8D	1.7m	5m	TC at measurement location	Full array set up, traverse moved through tunnel
1a	Locations_fromBottom	8D	1.7m	5m	TC at measurement location	No turbines set up for this measurement
2	XarrayR17Steps	8D	1.7m	5m	TC in tunnel on cart	
3	EquilSteps	8D	1.7m	5m	TC on cart	
4	RealTurbines	8D &10D	1.2m	no	TC in tunnel on PXI	3x3 array setup, turbines added to the front
4a	RealTurbines		1.2m	no	TC in tunnel on PXI	
5	SingleObject		1.2m	no	TC in tunnel on PXI	turbine was moved
5a	SingleObject		1.2m	no	TC in tunnel on PXI	turbine was moved

Figure D.1: List of data sets obtained with scale model turbines in the FPF

LocationsfromBottom

125.0, 187.5, 250.0, 312.5, 337.5, 362.5, 387.5, 412.5, 437.5, 500.0, 562.5, 625.0, 687.5, 750.0, 812.5, 875.0, 937.5, 1000.0, 1062.5, 1187.5, 1312.5, 1437.5, 1562.5, 1687.5

XarrayR17Steps

87.5, 112.5, 137.5, 162.5, 187.5, 200.0, 212.5, 225.0, 237.5, 250.0, 262.5, 275.0, 287.5, 300.0, 312.5, 325.0, 337.5, 350.0, 362.5, 375.0, 387.5, 400.0, 412.5, 425.0, 450.0, 475.0, 500.0, 525.0

EquilSteps

312.5, 337.5, 362.5, 387.5, 412.5, 437.5

RealTurbines

0.1875, 0.1975, 0.2075, 0.2175, 0.2275, 0.2375, 0.2475, 0.2575, 0.2675, 0.2775, 0.2875, 0.2975, 0.3075, 0.3175, 0.3275, 0.3375, 0.3475, 0.3575, 0.3675, 0.3775, 0.3875, 0.4075, 0.4275, 0.4475, 0.4675, 0.4875, 0.5075, 0.5275, 0.5475, 0.5675, 0.5875, 0.6075, 0.6275, 0.6475, 0.6675, 0.6875, 0.7075, 0.7275, 0.7475, 0.7675, 0.7875, 0.8075, 0.8275, 0.8475, 0.8675, 0.8875, 0.9075, 0.9275, 0.9475, 0.9675, 0.9875, 1.0075, 1.0275, 1.0475, 1.0675, 1.0875, 1.1075, 1.1275, 1.1475, 1.1675, 1.1875, 1.2075, 1.2275, 1.2475, 1.2675, 1.2875, 1.3075, 1.3275, 1.3475, 1.3675, 1.3875, 1.4075, 1.4275, 1.4475

SingleObject

0, 0.0102, 0.0203, 0.0305, 0.0407, 0.0508, 0.0610, 0.0712, 0.0814, 0.0915, 0.1017, 0.1119, 0.1220, 0.1322, 0.1424, 0.1525, 0.1627, 0.1729, 0.1831, 0.1932, 0.2034, 0.2136, 0.2237, 0.2339, 0.2441,

0.2542, 0.2644, 0.2746, 0.2847, 0.2949, 0.3051, 0.3153, 0.3254, 0.3356, 0.3458, 0.3559, 0.3661, 0.3763, 0.3864, 0.3966, 0.4068, 0.4169, 0.4271, 0.4373, 0.4475, 0.4576, 0.4678, 0.4780, 0.4881, 0.4983, 0.5085, 0.5186, 0.5288, 0.5390, 0.5492, 0.5593, 0.5695, 0.5797, 0.5898, 0.6000, 0.6500, 0.7000, 0.7500, 0.8000, 0.8500, 0.9000, 0.9500